Proses Simülasyonu ile Lazerle Metal Toz Ergitme Proses Parametrelerinin Etkisi Üzerine Bir Çalışma

Peter Rugu Maina

YÜKSEK LİSANS TEZİ

Havacılık Bilimi ve Teknolojileri Anabilim Dalı

Ekim 2020

A Study on the Effect of Varying Selective Laser Melting Process Parameters by Build Process Simulation

Peter Rugu Maina

MASTER OF SCIENCE THESIS

Department of Aviation Science and Technology

October 2020

A Study on the Effect of Varying Selective Laser Melting Process Parameters by Build Process Simulation

A thesis submitted to Eskisehir Osmangazi University
Graduate School of Natural and Applied Sciences
in partial fulfilment of the requirements for the degree of
Master of Science in the Department of Aviation Science and Technology
by

Peter Rugu Maina

Supervisor: Prof. Dr. Melih Cemal KUŞHAN
Co-supervisor: Assist. Prof. Dr. Evren YASA

October 2020

ETHICAL STATEMENT

I hereby declare that this thesis titled “A Study on the Effect of Varying Selective Laser Melting Process Parameters by Build Process Simulation” has been prepared in accordance with the thesis writing rules of Eskişehir Osmangazi University Graduate School of Natural and Applied Sciences under the academic consultancy of my supervisor Prof. Dr. Melih Cemal Kuşhan and Co-Supervisor: Assist. Prof. Dr. Evren Yasa. I hereby declare that the work presented in this thesis is original. I also declare that, I have respected scientific ethical principles and rules in all stages of my thesis study, all information and data presented in this thesis have been obtained within the scope of scientific and academic ethical principles and rules, all materials used in this thesis which are not original to this work have fully cited and referenced, and all knowledge, documents and results have been presented in accordance with scientific ethical principles and rules. 01/10/2020

Peter Rugu Maina

Signature

ÖZET

Yenilikçi bir endüstriyel üretim teknolojisi olarak, katmanlı imalat veya diğer bir deyişle eklemeli imalat, şekillendirme, kesme ve döküm gibi geleneksel metal üretim süreçlerine kıyasla yüksek derecede özelleştirmeye olanak tanıyan katman katman üretim konseptini kullanarak karmaşık geometrilere sahip üç boyutlu parçaların oluşturulmasına izin verir. Bununla birlikte, eklemeli üretim ile ilişkili sayısız avantaja rağmen, farklı proses parametreleri kombinasyonlarının kullanılması, çok sayıda proses parametresinin varlığı ve ürün performansına olan karmaşık etkileri, prosesin daha çok uygulama için kullanımının önünde önemli bir engeldir. Özellikle optimize edilmemiş proses parametrelerinin kullanılması nedeniyle, parça karmaşıklığına bağlı olarak 3 boyutlu metal parçaların ilk kez üretimi sırasında hata ve kayıp oranları oldukça yüksek olabilmektedir. Bu nedenle, metal parçaların başarılı bir şekilde mümkün olduğunca ilk seferde üretilmesi için metal katmanlı imalat süreçlerinin öngörülebilir ve güvenilir kılınarak, yüksek maliyetli ve zaman alıcı deneme yanılma girişimlerinin ortadan kaldırılması gerekmektedir. Malzeme israfını ve gereksiz makine zamanını engellemek için, üretimi başlatmadan önce, parçada toleransları aşan atmaların veya çatlakların hangi kritik yerlerde hangi proses parametreleri ile simülasyonu o nedenle kritik hale gelmektedir.

Bu amaca yönelik olarak, Autodesk Netfabb Simulation Utility yazılımı kullanılarak, Lazerle Metal Toz Ergitme proses parametrelerinin değişiminin, ortaya çıkan ısıl gradyenlerin, sıcaklıkların, artık gerilmelerin ve deformasyon dağılımını ve oluşumunu parça düzeyinde nasıl etkilediğini herhangi bir üretim yapmadan öngörebilmek amacıyla bir modelleme çalışması yapılmıştır. Bu çalışma sonuçları deneysel olarak doğrulanamadığı için, kullanılan modelin doğrulanması amacıyla, literatürde yer alan benzer modelleme teknikleri ve simülasyon yazılımları kullanılarak doğrulanmış deneysel çalışmalardan elde edilen sonuçlar kullanılmıştır.

Anahtar Kelimeler: Eklemeli Üretim, Lazerle Metal Toz Ergitme, Proses Parametreleri, Proses Modelleme, Simülasyon, Simulation Utility for Netfabb.

SUMMARY

As an emerging and innovative industrial production technology, Additive Manufacturing (AM) allows for realization of three-dimensional shapes with complex geometries based on a layer-by-layer incremental manufacturing concept with high degrees of customization compared to traditional metal manufacturing processes such as forming, cutting and casting. However, despite the numerous advantages associated with additive manufacturing, the use of different combinations and the presence of a large number of process parameters, as well as their complex effects on product performance are a major obstacle to the use of these processes in many applications. Due to the use of non-optimized process parameters, part failure rates can be quite high especially during the first-time production of 3D metal parts Therefore, to successfully manufacture metal parts at the very first attempt, it is imperative that metal additive manufacturing processes are made predictable and reliable by eliminating costly and time-consuming trial and error attempts. To prevent wastage of both metal material and machine operating time as a result of repetitive production of faulty parts, it is therefore critical to simulate potential defects or cracks that may exceed the recommended tolerances for a particular part before initiating the printing process.

In this work, a modelling study using Autodesk Netfabb Simulation Utility software was carried out to predict the extent at which changes in the magnitude of Selective Layer Melting (SLM) process parameters affect the distribution and formation of thermal gradients, temperatures, residual stresses and deformation solely by simulation without actually producing the part itself. Since the results of this study could not be verified experimentally, the model used was verified using results obtained from previously validated experimental studies as well as literature from validated work in which similar modelling techniques and simulation software were used.

Keywords: Additive Manufacturing, Selective Laser Melting, Process Parameters, Process Modelling, Simulation Utility for Netfabb.

ACKNOWLEDGEMENT

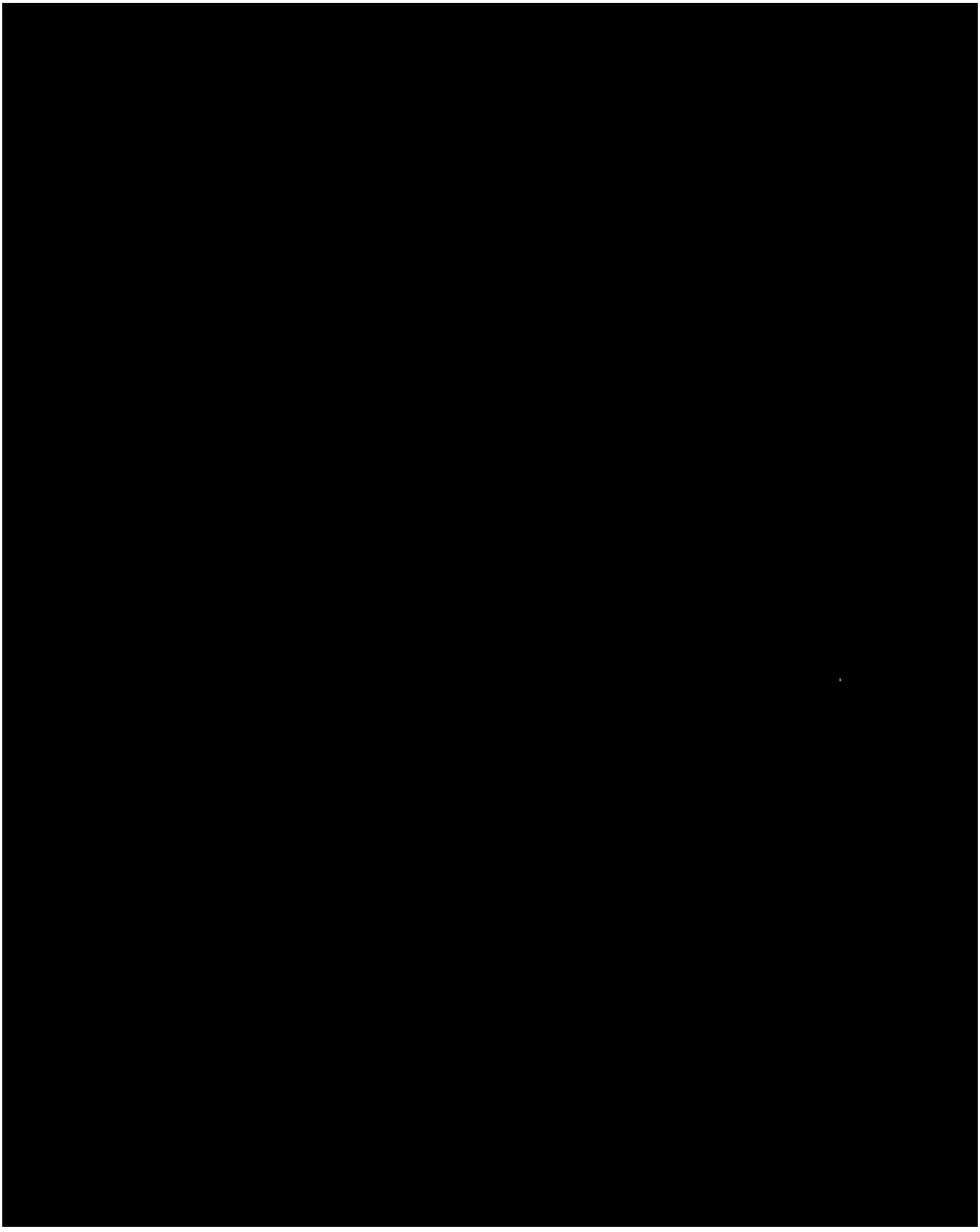

LIST OF CONTENTS

Page

LIST OF CONTENTS

LIST OF FIGURES

Figure **Page**

LIST OF FIGURES (continued)

Figure **Page**

LIST OF FIGURES (continued)

Figure **Page**

LIST OF FIGURES (continued)

Figure **Page**

LIST OF TABLES

Table **Page**

LIST OF SYMBOLS AND ABBREVIATIONS

Symbol	Description
mm	Millimetre
µm	Micrometre
Ø	Diameter
λ	Wavelength
°C	Degree Celsius
α + β	Alpha-Beta
≤	Less than or equal to
~	Approximate
η	Laser absorption efficiency
U^0	Initial nodal solution vector estimate
U^i	Nodal solution vector of the current iteration
U^{i+1}	Nodal solution vector of the preceding iteration
R	Residual vector
$\frac{dR^i}{dU}$	Stiffness matrix
R^i	Residual vector for the current iteration
ρ	Density
Cp	Isotropic heat capacity
T	Temperature
t	Time
x_j	Position vector
q_i	Heat flux vector
Q	Body heat source
T_∞	Ambient temperature
T_0	Initial temperature
T^{ref}	Reference temperature
k(T)	Isotropic temperature dependent on thermal conductivity

LIST OF SYMBOLS AND ABBREVIATIONS (continued)

Symbol	Description
a	Width of the ellipsoid in the y-direction
b	Depth of the ellipsoid in the z-direction
c	Length of the ellipsoid in the x-direction
q_c	Heat flux due to convection
T_s	Surface temperature
q_{rad}	Heat flux due to radiation
ϵ	Surface Emissivity
h	Heat Transfer Coefficient
σ	Stefan-Boltzmann constant
h_{rad}	Heat Transfer Coefficient for radiation
P	Laser Power
v_s	Speed of the laser
σ_m	Von Mises stress
ε_T	Total strain
ε_e	Elastic strain
ε_{th}	Thermal strain
ε_p	Plastic strain
ε_q	Equivalent strain
$\nabla \cdot$	Divergence
C	Fourth-order material stiffness tensor
α	Thermal expansion coefficient
f	Yield function
σ	Stress
σ_{von}	von Mises stress
a_{flow}	Flow vector
σ_{yield}	Yield stress
P	Piola Kirchoff stress tensor

LIST OF SYMBOLS AND ABBREVIATIONS (continued)

Symbol	Description
Pa	Pascal
J	Determinant of gradient of deformation
F	Deformation gradient
D	Displacement gradient
E	Green strain
I	Identity matrix
s	Seconds
kg	Kilogram
deg	degree
W	Watts
x	x coordinates
xy	xy plane
xz	xz plane
y	y axis
z	z axis

Abbreviation	Description
3D	Three-dimensional
3MF	3D Manufacturing Format
AM	Additive Manufacturing
ASTM	American Society for Testing and Materials
CAD	Computer-Aided Design
CO_2	Carbon Dioxide
CPU	Central Processing Unit
CTE	Coefficient of Thermal Expansion
CW	Continuous Wave

LIST OF SYMBOLS AND ABBREVIATIONS (continued)

Symbol	Description
AMF	Additive Manufacturing File
DED	Directed-Energy Deposition
DMP	Direct Metal Printing
DVRT	Differential Variable Reluctance Transducer
EBM	Electron Beam Melting
EOS	Electro-Optical Systems
FEA	Finite Element Analysis
FEM	Finite Element Method
FESEM	Field Emission Scanning Electron Microscopy
LENS	Laser Engineered Net Shaping
LMD	Laser Metal Deposition
LOF	Lack of Fusion
LPBF	Laser Powder Bed Fusion
Nd: YAG	Neodymium-doped Yttrium Aluminium Garnet
LPS	Liquid Phase Sintering
PRM	Processing Parameter
RAM	Random-Access Memory
SEM	Scanning Electron Microscopy
SLM	Selective Laser Melting
SLS	Selective Laser Sintering
SSS	Solid State Sintering
STL	Standard Tessellation Language
TC	Thermocouple
XWB	Extra Wide Body

1. INTRODUCTION AND PURPOSE

Additive Manufacturing (AM) also known by various names such as Layer Based Manufacturing, Additive Layered Manufacturing, Freeform Fabrication, Solid Freedom Fabrication, Rapid Prototyping and more commonly as 3D Printing (Huang et al., 2013) among others has been around for decades, with its first successful patent of an AM process dating back to 1972 as A. Ciraud introduced the concept of metal layer fabrication by powder deposition method using electron or laser beams. (Ciraud, 1972)

The American Society for Testing and Materials (ASTM) F2792 defines Additive Manufacturing as the "process of joining materials to make objects from three-dimensional (3D) model data, *usually layer upon layer*, as opposed to subtractive manufacturing methodologies" (ASTM International, 2013).

AM as a transformative technology can create products with increased efficiency and accuracy in component design, faster product delivery, simplified supply chains, reduced wastage and lower environmental impact. This makes it a more sustainable manufacturing process compared to other convectional manufacturing technologies.(Ford & Despeisse, 2016).

With direct AM processes such as Laser Metal Deposition (LMD), Selective Laser Melting (SLM), Electron Beam Melting (EBM) and Laser Engineered Net Shaping (LENS) methods, the final part is formed by allowing the metal powder to melt completely and solidify into the desired form.(Azam et al., 2018). Optimized processes are known to be able to produce parts with more than 90% density compared to indirect AM methods such as Binder Jetting processes and Selective Laser Sintering (SLS) necessitating post-processing infiltration operations (Yang et al., 2017).

As a subgroup of AM technologies, Powder Bed Fusion (PBF) systems employ laser or electron beams as their thermal energy sources to produce parts whose microstructures and morphologies depend, to a great extent, on the thermal-physical phenomena involved.

Building the part in a powder bed in a layer wise manner is one of the common properties of powder bed fusion processes including Selective Laser Melting, Electron Beam Melting, Selective Laser Sintering, Selective Heat Sintering and Multi Jet Fusion.

Selective Laser Melting, being one of the most applied AM process for metals in highly demanding industries is generally preferred to produce very complex geometries with internal features leading to good mechanical properties comparable to those produced with conventional manufacturing.

The main objective of this study is to demonstrate the individual effects of varying significant SLM process variables, such as the scan speed, layer thickness, laser power, preheating temperatures and built plate thickness by using a commercial SLM modelling software to eliminate the need of a costly and time-consuming trial-and-error approach. These resultant effects from varying the process variables are evaluated on a part level scale to investigate the extent at which they influence the thermal gradients, temperature distribution, displacement magnitudes (distortion) and the residual stresses.

In order to evaluate the accuracy levels of the modelling, a validation of the model is first performed based on the existing literature. Later on, the simulations are run on a complex geometry, selected as an aircraft bracket.

The first chapter of this thesis introduces additive layer manufacturing. The aims and objectives of this study as are also addressed.

In the second chapter, comprehensive literature review of the SLM Process from published literature is presented. Description of SLM process parameters, powder properties and the interaction between the laser and the metal powder is also addressed. In this chapter, the undesired physical behaviour in typical SLM processes and the defects associated with material porosity and induced residual stresses during SLM of Ti6Al4V. The general modelling approach as obtained from various research work is also addressed.

The third chapter addresses the three-dimensional finite element model used for this work. The temperature dependent thermal and mechanical properties for Ti6Al4V used in

the simulation using Autodesk's Simulation Utility for Netfabb are also presented as obtained from previous and current literature. Process parameters and meshing criteria for powder bed part level simulation are also explained here.

The fourth chapter outlines the simulation results by showing the relationships between the thermal gradients, temperature histories, interlayer temperatures, stress results and the varying SLM process parameters. The approach used to validate the model used for simulation is presented here.

In the last chapter, a summary of the findings of this study is addressed. Suggestions for future studies using a similar approach were addressed.

2. LITERATURE REVIEW

2.1. Selective Laser Melting

Selective Laser Melting as a direct AM powder bed fusion process produces three-dimensional (3D) parts by use of a layer by layer build approach that geometrically conforms to a CAD model to selectively melt metal powder particles using a high power-density and focussed laser as a heat source.

With optimized process parameters, SLM is capable of manufacturing near net shape parts with complex geometries and relatively high part densities above 99% while eliminating the need for certain specific tooling requirements (Bian et al., 2017; Kozak & Zakrzewski, 2018; Wang et al., 2018). The process can be used with a large variety of metallic materials such as titanium and nickel-based alloys, aluminium, stainless steels, tool steels, cobalt, chrome, iron, copper and even precious metals for jewellery applications (Bian et al., 2017).

SLM fabricated components (see Figure 2.1 for examples) for both aerospace and medical applications including dental and orthopaedic implants (Brandt et al., 2013; Sing et al., 2016; Tan et al., 2017; Wehmöller et al., 2005) presenting the notable production challenging attributes associated with curved surfaces and porosity, can directly be produced, even as functional prototypes.

A typical system for an SLM machine, as shown in Figure 2.2, consists of a 50-700 W single or multiple laser beam and galvano scanner unit, a build platform where the base plate is mechanically fixed on, temperature sensors, control unit, inert gas supply and circulation unit, powder feeder and coating mechanisms. Galvano scanners have been used for laser beam XY positioning to targeted coordinates (Buls et al., 2013). Build chambers of varying dimensions can be used depending on the manufacturer's configuration and the intended build rate (Poprawe et al., 2014). Currently, the maximum build size in the SLM

machines is limited to build envelope (L x W x H) of 500 x 280 x 875 mm (SLM Solutions Group AG, 2020).

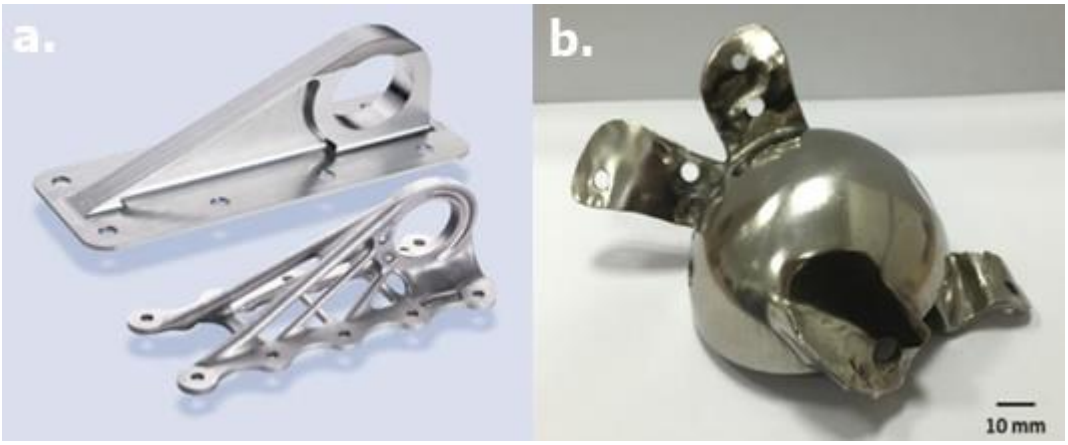

Figure 2.1. Typical applications of SLM: a) Bionic cabin bracket for the Airbus A350 XWB aircraft, b) Polished hip joint implant (Sing et al., 2016).

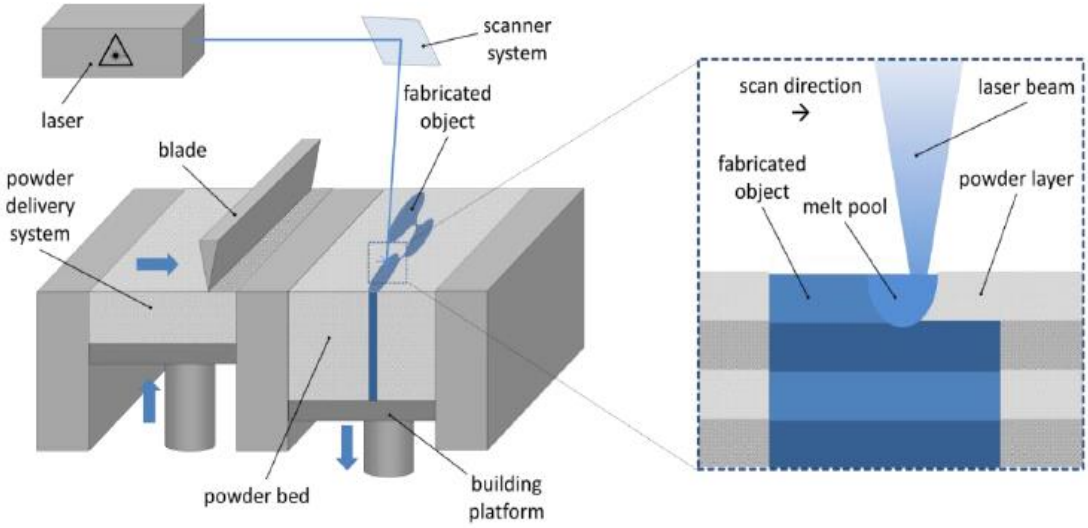

Figure 2.2. Schematic of typical SLM machine setup (Leitz et al., 2018).

The machine control unit provides an interface with the user in which monitoring, adjustment and control of crucial process parameters is done. A computer is also needed to facilitate for CAD models in either Standard Tessellation Language (STL) or Additive Manufacturing File (AMF) format to be edited or sliced in preparation for use as guiding geometries in the layer building stage.

Notable manufacturers for SLM systems with varying architecture and functionality are EOS GmbH, Renishaw, 3D Systems, SLM Solutions and Concept Laser GmbH among others. (*A Comprehensive List of All the Metal 3D Printer Manufacturers*, 2018).

Table 2.1. Technical Specifications of Common SLM machines.

Manufacturer	**Model**	**Build Volume (L×W×H) mm**	**Laser Power/Type**	**Max. Scan Speed (m/s)**	**Focus Diameter approx. (µm)**	**Layer Thickness (µm)**
Concept Laser	Laser Mlab	50-90 x 50-70 x 80	100W/Fiber laser (CW)	7	50	15 – 30
	Laser Mlab R	50-90 x 50-70 x 80	100W/Fiber laser (CW)	7	50	15 – 30
	Mlab 200R	100 x 100 x 100	200W/Fiber laser (CW)	7	75	15 – 30
	X Line 2000R	800 x 400 x 500	2 x 1kW/ Fiber laser (CW)	7	100 –500	30 – 150
	M2 Series 5	245 x 245 x 350	1 or 2 x 400W/ Fiber laser (CW)	4.5	70 - 500	20 - 80
	M Line Factory	500 x 500 x 400	4 x 400W (or 1kW)/Fiber laser		50 – 500	20 – 100
SLM Solutions	SLM® 125	15 x 125 x 125	1x 400W/Fiber laser	10	70 - 100	20 - 75
	SLM® 280	280 x 280 x 365	1 or 2 x 400W/Fiber laser 1 or 2 x 700W//Fiber laser 1x 700W and 1x 1kW Fiber laser (Dual)	10	80 - 115	20 - 90
	SLM® 500	500 x 280 x 365	2 or 4 x 400W/Fiber laser 2 or 4 x 700W//Fiber laser	10	80 - 115	20 - 75

Table 2.1. Technical Specifications of Common SLM machines (continued)

SLM Solutions	SLM® 800	500 x 280 x 850	4 x 400W/Fiber laser 4 x700W//Fiber laser	10	80 - 115	20 - 90
3D Systems	DMP Flex 100	100 x 100 x 80	100W/Fiber laser	No data*	No data*	10 - 100
	ProX DMP 200	140 x 140 x 100	300W/Fiber laser	No data*	No data*	10 - 100
	ProX DMP 300	250 x 250 x 305	500W/Fiber laser	No data*	No data*	10 - 100
	ProX DMP 320	275 x 275 x 380	500W/Fiber laser	No data*	No data*	10 - 100
Renishaw	AM 125	120 x 120 x 125	100W/200W/Yb-fiber laser	2	35	20 - 100
	AM 250	250 x 250 x 300	200W/400W/Yb-fiber laser	2	70	20 - 100
	AM 400	250 x 250 x 300	400W/Yb-fiber laser	2	70	20 - 100
	RenAM 500	250 x 250 x 350	4 x 500W/Yb-fiber laser	2	80	20 - 100
EOS	EOS M 100	Ø 100 x 95	200W/Yb-fiber laser	7	40	No data*
	EOS M 290	250 x 250 x 325	400W/Yb-fiber laser	7	100	No data*
	EOS M 300-4	300 x 300 x 400	4 x 400W/Yb-fiber laser	7	100	No data*
	EOS M 400	400 x 400 x 400	1kW/Yb-fiber laser	7	90	No data*

* The official data sheets showing the detailed technical specifications did not reveal these values.

The SLM process, from part design to fabrication involves a series of steps that translate the part geometries from a 3D-CAD data file into successfully melted layers of

fully built components (see Figure 2.3). The CAD file, usually in Stereo Lithography (STL) format, is processed to create support structure for geometries with overhanging parts and slice data that corresponds to each layer.

The part build process begins in the building chamber after a thin layer, usually 20–200 µm (Shi et al., 2016) of the selected metal powder is uniformly placed on the substrate plate by use of a recoater blade, which may be a soft or hard blade, depending on the machine specifications or application needs.

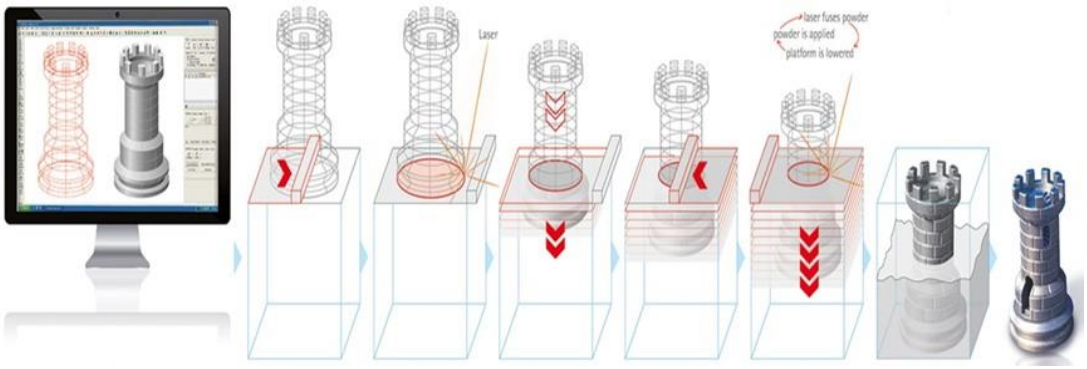

Figure 2.3. Steps in the SLM Process (*EOS Industrial 3D Printing - Process, Method and Benefits*, n.d.)

Laser types used in most SLM systems are Yb-fiber, Nd: YAG (neodymium-doped yttrium aluminium garnet laser) and CO_2 lasers with wavelengths, λ, of 1.07, 1.06 and 10.6µm respectively. The laser properties such as the power and beam diameter are known to have a significant effect of the part microstructure and build rates as widely addressed in the literature (Choo et al., 2019; Do & Li, 2016).

After powder deposition on the build plate, pre-heating can be done. The pre-heating of the powder bed and substrate has a significant effect on minimizing thermal induced residual and cyclical stresses as it lowers the thermal gradients (Aggarangsi & Beuth, 2006; Buchbinder et al., 2014; Zaeh & Branner, 2010) and improves the surface quality of SLM produced parts.(Savalani & Pizarro, 2016). More importantly, pre-heating is carried out to eliminate the humidity of the powder to enable a strong connection between the first layers and the build plate (Yasa, 2018).

Suggested pre-heating temperatures for alloys such as Ti-6Al-4V in literature are between 200-500°C (Vilaro et al., 2011). However, the SLM machines generally have a maximum preheating temperature of 200 °C (Yasa, 2018). The high energy density laser is then directed to the powder bed to initiate the melt and selective fusion of the targeted areas on the x-y-plane depending on the area to be scanned coming from the CAD file. Upon completion, the build platform is lowered to a depth of equal magnitude to the selected layer thickness and a new powder layer is deposited.

In the solidification phase, the melt tracks of the newly melted layer then fuse together with those of the previously solidified layer. The successive layers that constitute of the final part are then scanned and lowered down until the entire build is complete. The unmelted metal powder is collected and sieved for later use.

Since the part is built in a powder bed and the thermal conductivity of powder in comparison to bulk material is too low, support structures (see Figure 2.4 b.) are necessary to avoid warping, cracking and deformations led by residual stresses occurring during the SLM process. Lattice-like support structures such as those shown in Figure 2.4 a. are generally used to improve heat dissipation (Hanzl et al., 2017) and provide support for both overhanging surfaces (Herzog et al., 2016).

The presence of a protective gas atmosphere consisting of argon or nitrogen gas prevents or minimizes possible contamination and oxidation of the melt pool at elevated temperatures. With titanium alloys, it is critical to keep the residual oxygen content in the build chamber below 0.1% and argon gas is preferred to prevent nitride formation (Attar et al., 2014; Kumar et al., 2014).

Crucial processes involved in the part fabrication by SLM such as melting and solidification are also greatly influenced by the selected laser properties such as wavelength, mode (CW or pulsed), energy distribution, pulse energy and repetition rate (Lee et al., 2017).

The correlation between an increase in layer thickness and increased production time was observed in SLM produced 1Cr18Ni9Ti stainless steels (M. Ma et al., 2015). Similarly, a decrease in surface quality was also realized (Kozak & Zakrzewski, 2018). Reduced layer

thickness can result to improved melting and part density (Sufiiarov et al., 2017) and may potentially decrease part surface roughness by reduction of the staircase error effect (Bian et al., 2017).

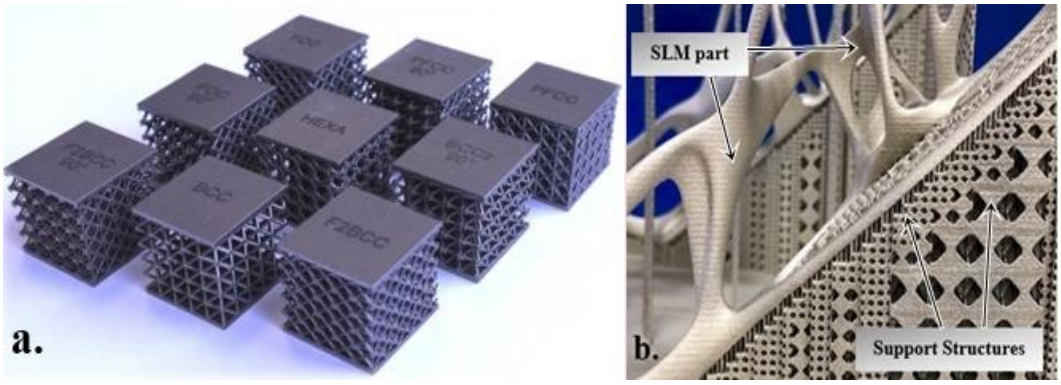

Figure 2.4. a). Typical lattice structures in Additive Manufacturing (Hanzl, Zetkova, and Dana 2017) b.) Support structures on an SLM produced part (Stevenson 2018.)

2.1.1. SLM of Ti6Al4V

As a widely used α + β titanium alloy for advanced aerospace applications, Ti6Al4V, also referred to as Ti64, offers exceptional material properties such as high strength-to-weight ratio, excellent fatigue and corrosion resistance (Harris, 2011; Inagaki et al., 2014). Ti6Al4V is also considered to occupy about 50% of the global market share of titanium products (S. Liu & Shin, 2019). The high specific strength to weight ratio property contributes to its prevalence in the manufacture of compressor blades and casings for aerospace applications (Kuroda et al., 2015). As an aerospace application, Ti6Al4V is used to manufacture fan blades and cases for aircraft engines as the working temperatures in the front part of the engine do not exceed 300 °C (Inagaki et al., 2014).

Compared to pure titanium, the higher fatigue resistance and bio inert properties due to its α+β microstructure is attributed to its wide use in medical applications such as joint replacements (Munsch, 2017), hip prothesis and dental implants (Elias et al., 2018). However, the higher Young's modulus of Ti6Al4V in comparison to bone can potentially cause pain when used in some biomedical applications such as stress shielding of the femur

(Shah et al., 2018). Similarly, the released Al and V metal ions from the Ti6Al4V implants can also predispose its users to systemic carcinogenic effects (Elias et al., 2018).

As a drawback, the parts produced using selective melting of Ti6Al4V have martensitic microstructure that has high hardness and low ductility characteristics (Chlebus et al., 2011). As a post processing step of the process, various types of heat treatment are preferred to improve its mechanical properties (Borisov et al., 2015).

Vrancken et al. 2012 observed that the high cool rates used to increase part densities for Ti6Al4V parts resulted to low ductility despite the achieved high tensile strengths due to the prevailing acicular martensite microstructural composition (Thijs et al., 2010;Simonelli et al., 2012; Vrancken et al., 2012).

The Yb-fiber and Nd:YAG lasers (Figure 2.5). are suitable for metal part production as their shorter wavelengths make it suitable for AM for materials, such as metals, whose reflectivity decrease with corresponding a decrease in laser wavelength (Okamoto et al., 2004).

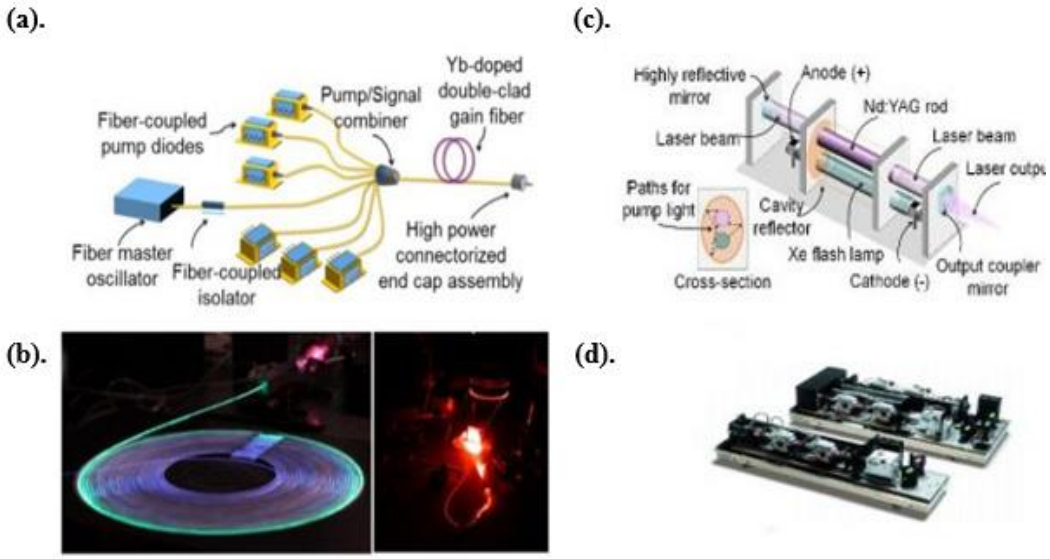

Figure 2.5. Common Lasers for SLM of Metals: (a) Schematic of an Yb-fiber laser, (b) Yb-fiber lasers, (c) Nd:YAG laser schematic showing key parts,(d) Commercial Nd: YAG laser (Lee et al., 2017)

The Yb-fiber and Nd:YAG lasers are suitable for metal part production as their shorter wavelengths make it suitable for AM for materials, such as metals, whose reflectivity decrease with corresponding a decrease in laser wavelength (Okamoto et al., 2004). As an advantage during SLM of metals and their alloys, Yb-fiber lasers have gained much attraction owing to their much smaller sizes and higher beam qualities and efficiencies (see Table 2.3).

As a multifactorial based AM process, SLM is greatly influenced by various parameters attributed to the laser, powder properties and the laser melting process. Some critical SLM parameters (see Table 2.2.) that demand proper selection to achieve high part performance in terms of improved mechanical properties, microstructures and dimensional accuracies include laser power, spot size, scan speed, scanning strategy, layer thickness, hatch spacing as well as powder characteristics such as morphology, flow properties and composition (Lu et al., 2015; Yap et al., 2015).

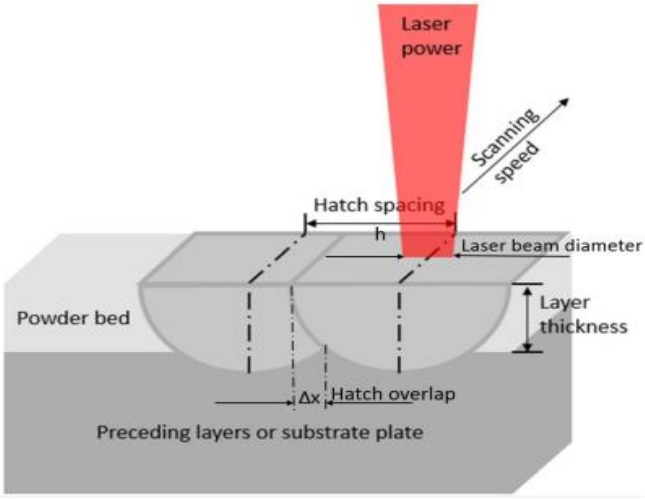

Figure 2.6. Schematic of various SLM parameters. (Yap et al., 2015)(H. Zhang & LeBlanc, 2018).

The energy density (E_d), also referred to as the energy input in SLM is influenced by the laser power, scan velocity, powder layer thickness and the hatch spacing as shown in (2.1)(Shipley et al., 2018).

$$E_d = \frac{P}{v_s\, h\, d} \tag{2.1}$$

Where the energy density (J/mm^3), laser power (W), layer thickness (mm), hatch spacing (mm) and the scan speed (mm/s) are represented by E_d, P, d, h and v_s respectively. However, crucial factors that also influence the energy density such as the direction of gas flow, laser diameter and the hatch style are not accounted for in (2.1) (Prashanth et al., 2017).

Table 2.2. Main SLM Process Parameters

Laser-related	**Scan-related**
Laser source and power Laser beam diameter Laser wavelength	Scan speed Scan spacing Scan pattern
Powder-related	**Temperature-related**
Powder shape, size, density and morphology Particle distribution Layer thickness	Temperature distribution Powder bed temperatures

The laser power can be adjusted automatically to effectively control melt pool sizes. The choice of a particular laser power setting is often influenced by the powder material properties as well as the application needs. With a selected laser power value, multiple energy densities can be achieved by varying the laser beam spot size (Kumar et al., 2014).

Table 2.3. Properties of lasers used in metal SLM (Abliz et al., 2014; Lee et al., 2017)

Laser Type	**Nd: YAG laser**	**Yb-fiber laser**
Operational wavelength	1.06 μm	1.06 -1.09 μm
Efficiency	10-20% (Diode Pump)	10-30%
Output power Continuous Wave (CW)	≤ 16 kW	≤ 10 kW
Operation mode	CW and Pulse	CW and Pulse
Pump source	Laser diode	Laser diode
Beam quality factor (mm·mrad)	0.4 – 20.0	0.3 – 4.0

The laser spot size can be considered to be the measured laser beam's diameter on the powder bed (see Figure 2.6.). The magnitude of the spot size can range from 30 μm to 600 μm, with typical values for predominant SLM systems set between 50 μm and 180 μm (Herzog et al., 2016). Variations in energy density can be achieved upon increments or decrements of the spot size (Kumar et al., 2014).

As a critical requirement, the scan or hatch spacing which the measured distance between consecutive laser beams or adjacent scan vectors (Rafi et al., 2013) should be preferably lesser than the melt pool width to guarantee enough overlap (Vrancken, 2016).

With a variety of scanning strategies available for SLM processing, the resultant effects that arise from use of various scan strategies have been observed across various works. L. Parry et al. 2016 compared the unidirectional and alternate scan strategies and observed that the latter resulted to reduced residual stress inducing temperature gradients.

J. P. Kruth et al. 2012 claimed that the island scanning strategy (see Figure 2.7 a.) which is a Concept Laser GmbH patented scanning option that utilizes random short scans on the x-y plane, could potentially minimize cracking and residual stresses. Vrancken 2016 observed that the texture of SLM produced parts was also greatly influenced by rotation of a particular scan strategy.

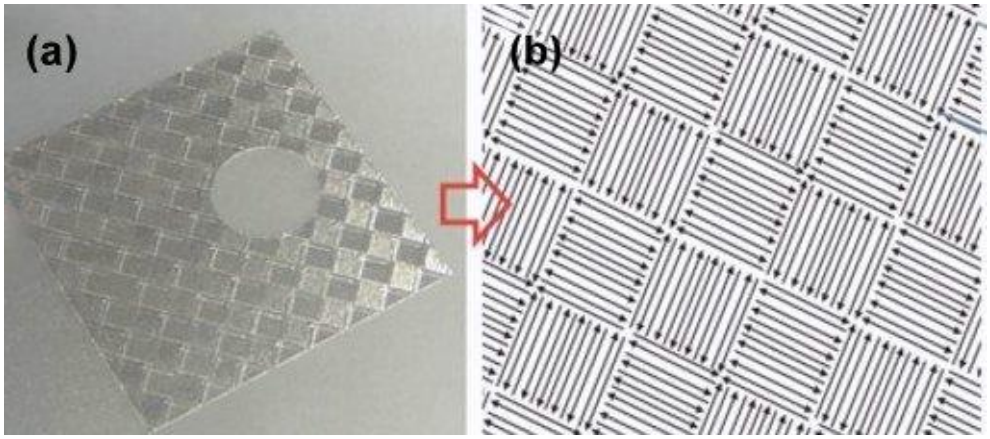

Figure 2.7. a.) Part produced using island scanning strategy and b.) schematic showing the island scans.(Lu et al., 2015)

2.1.2. Powder Properties for SLM

Powder properties such as particle size, shape and distribution have a significant effect on the efficiency of the melting process for metals. Other powder properties, such as thermal conductivity, absorptivity/relativity, chemical composition also influence the interaction of the laser and material during the SLM processing.

Gas atomized spherical metal powders (see Figure 2.8.) facilitate for relatively high powder bed density and flowability resulting to their preference in AM when compared to other shapes (Trevisan et al., 2017). The optimal powder size distribution has to be carefully selected as larger particles have a lower pack density and require high energy amounts to be efficiently melted while smaller particles may cause fumes that further complicating the layer building process (H. Zhang and LeBlanc, 2018) despite the latter having advantages of higher pack densities and reduction in surface roughness (Sutton et al., 2016).

Generally, a good mix of small and large particles is preferred so that the powder bed properties can be optimized.

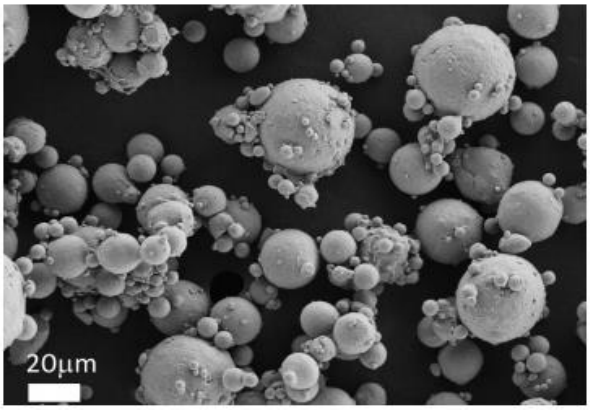

Figure 2.8. Gas atomized aluminium powders of different sizes (1-30 µm) as observed from a Field Emission Scanning Electron Microscopy (FESEM) image. (Trevisan et al. 2017)

Studies by B. Liu et al. 2011 indicated that an increase in density of parts produced at low laser energy intensities and powders constituted of varying sizes. The minimum layer thickness, from which the powders melt to form, is also determined by the metal powder size as it can only be equal or smaller than the powder size distribution in use (Kumar et al., 2014).

To a considerable extent, good powder flowability during the build as investigated by B. Liu et al. 2011 is essential to attain a constant and homogeneous layer thickness, as a necessary requirement for uniform laser energy absorption. Thijs et al. 2010 investigated the effects of the zig-zag, unidirectional and cross-hatching scan strategies for plasma atomized,

spherical Ti-6Al-4V powder. They determined that both the hatch spacing and the scan speed, to a considerable extent, influenced the resultant hardness and width of the melt pool and that grain growth preferentially occurred in the direction of the build.

2.2. The Laser - Material Interaction

As a multifactor process, physical behaviour of SLM produced parts are widely influenced by laser parameters, powder material properties, process temperatures, scan strategies and the thermal-physical phenomena (see Figure 2.9). The laser power, spot size, scanning strategy and the hatch spacing among other parameters highly influence the type of the binding mechanisms which can result to Solid State Sintering (SSS), Liquid Phase Sintering (LPS), partial melting and complete melting (J. P. Kruth et al., 2005). The absorption of the laser beam's energy initiates the melting process that causes to an overall decrease in volume. The loose powder, and the partially melted powder in the re-melted zone form a melt pool (Pal & Drstvensek, 2018).

Heat transfer through conduction, radiation and convection mechanisms occur as metal evaporation dissipates heat from the melt pool (Chen et al., 2018). However, uneven heat distribution from the resultant melt pool to its close environment due to the protective gas atmosphere and other different heat transmission media present is responsible for the Marangoni effect, which is a resultant effect of tangential gradients of surface tension in the melt pool and possible gaseous bubble entrapment (Chen et al., 2018).

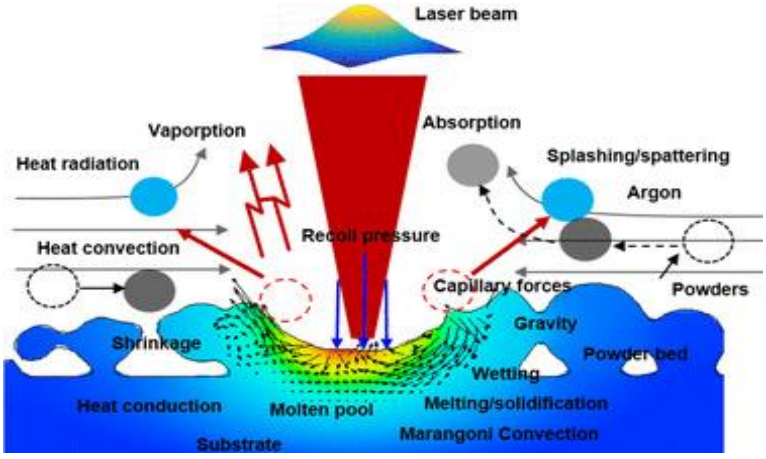

Figure 2.9. The physical phenomena in SLM (Chen et al., 2018)

As a prerequisite for fabricating high-quality parts using SLM, prediction of thermal behaviour and melt pool flow characteristics is paramount. The recoil pressure and Marangoni force have been suggested to be among the major forces that for the occurrence of melt flow instability (Qiu et al., 2015).

In addition to heat conduction, other physical phenomena that are likely to be influenced by either the SLM process parameters or the metal powder material properties include radiation, laser energy transmission and absorption, wetting, balling, splashing, capillary forces, rapid melting and solidification (Antony & Arivazhagan, 2015).

2.3. Undesired Physical Behaviour

The presence of unwanted phenomena in SLM such as the melt pool instability, material spattering, keyhole and balling effects greatly contribute to the increased porosity and reduced densities (Pal & Drstvensek, 2018).

Material splattering (see Figure 2.10.) that occurs in the metal powder, molten metal melt or in the mixture of partially molten metal powder and the latter is regarded as a key unwanted phenomenon in SLM since it induces uneven material distribution and bad surface quality (Anwar & Pham, 2016; Wang et al., 2016).

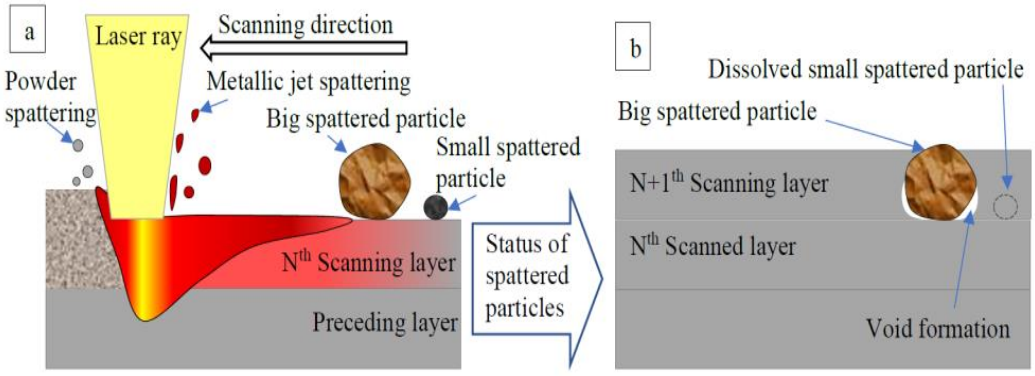

Figure 2.10. Schematic diagrams showing (a) powder and metallic jet spattering, (b) the defects associated with spattering. (Pal & Drstvensek, 2018)

Splattering, as investigated by Pal and Drstvensek 2018, occurs due to trapped gas expansion and explosion, thermal shock and recoil pressure from either the laser (Han et al.,

2017) or metal vapor. Material spattering behaviour is influenced by certain metallurgical properties such as the molten metallic viscosity, thermal conductivity and specific heat (Pal and Drstvensek, 2018). Optimization of process parameters, powder particle shape and size can considerably control splattering.

The balling effect, which is the spheroidization of the liquid melt pool, is attributed to various phenomena. Bauereß et al., 2014 in their work on defect generation and propagation mechanisms attributed it to insufficient metal material for liquid formation during melting.

D Gu et al. 2012; Baauw et al. 2015 associated the balling effect with melt track irregularities or discontinuities that result from melt pool instabilities due to deteriorated wettability between the molten metal material and underlying substrate. Melt pool splashing and high melt flow velocities have also been identified as causative effects of the balling phenomena (Dai & Gu, 2014; Dongdong Gu et al., 2012; Qiu et al., 2015). As a critical defect to SLM, balling results to part surface roughness and increased porosity which hinders production of fully dense parts. Optimized laser power density is crucial in prevention of balling as D Gu et al. 2012 in his work linked both low and high laser power densities with an increase of balling effect and splash induced balling respectively.

Similarly, the use of properly selected scan speeds can prevent melt pool instabilities that otherwise induce balling (Shi et al., 2016). As a remedy, Zhou et al. 2015 observed that remelting the surface, preferably by use of a second laser, while using appropriate laser exposure times to attain a balanced dynamic viscosity of the melt pool can minimize the balling effect in metals have considerably high thermal conductivity.

2.4. Defects in SLM Processed Ti-6Al-4V

Defects in SLM manufactured parts such as those depicted in Figure 2.11. that often lead to part failure or reduced part performance can arise from the aforementioned complex physical phenomena and possibly from unoptimized process parameters. However, even with optimized SLM process parameters, defects like porosity could also occur to a lesser extent (Kasperovich and Hausmann, 2015).

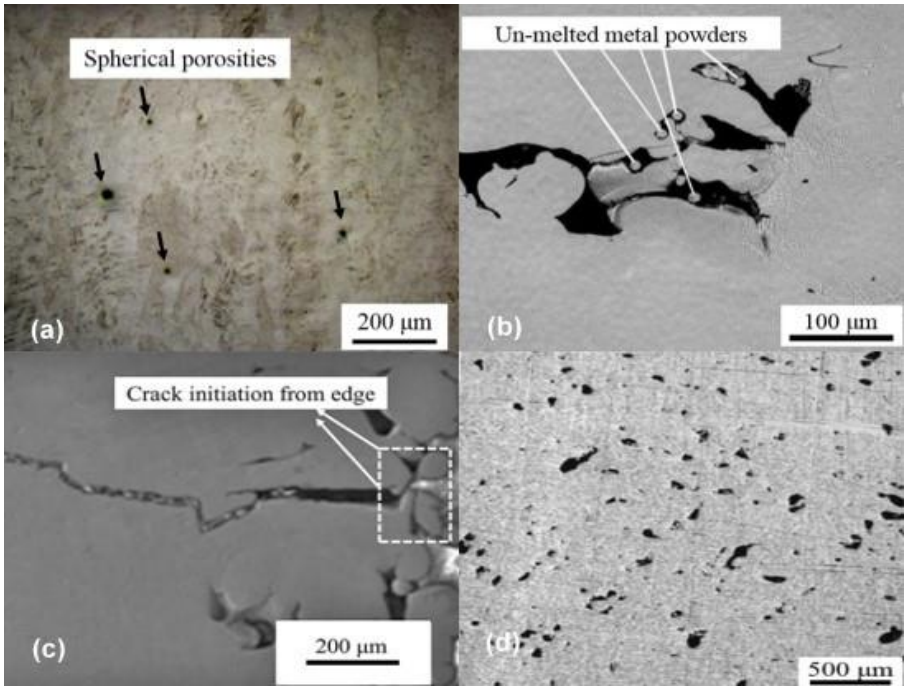

Figure 2.11. Optical images of defects in SLM fabricated Ti-6Al-4V parts: (a) Spherical porosities (b) Lack-of-Fusion (LOF) defects and un-melted Ti-6Al-4Vpowder. (c) SEM image showing crack initiation (d) incomplete fusion holes formed at 120 W and scanning velocity of 1500 mm/s (B. Zhang et al., 2017)

In general, defect sources attributed to SLM in literature (Attar et al., 2014; Gong et al., 2014)(Seifi et al., 2016) stem from partially melted or unmelted metal powder particles, gas entrapment in either atomization or melt pool solidification, lack of fusion (B. Zhang et al., 2017) and layer delamination (Yasa et al., 2009); (Kempen et al., 2013). Defect formation could also be attributed to powder properties such as composition, morphology and the particle size distribution (Gorsse et al., 2017).

Other notable defects in SLM processed Ti6Al4V include: dimensional inaccuracies (Kozak & Zakrzewski, 2018), stress related cracking, dimensional warping (Mumtaz et al., 2011), and microstructural defects such as balling and porosity (Xia et al., 2017) that are observed to greatly influence dynamic mechanical performance of SLM processed Ti6Al4V parts (Leuders et al., 2013).

2.4.1. Porosity

As a prominent defect associated with SLM, porosity has been associated with certain scanning strategies as well as with application of either insufficient or excessive laser energy intensities and adversely affects the mechanical performance (Borisov et al., 2015; Zhao et al., 2016). Aboulkhair et al. 2014 focused on the design of a scan strategy in an effort to minimize porosity.

Thijs et al., 2010 observed that the melt pool behaviour and stability highly influence the degree of porosity with the pores occurring either as spherical as shown in Figure 2.11(a) or irregularly shaped with the latter being attributed to unstable molten pool shapes. The irregular, non-spherical pores are process-induced as their occurrence is as a result of insufficient laser energy application and spatter ejection (Sames et al., 2016). Great concern from this pore type arises as they predispose fabricated parts to increased stress concentrations that can result to crack nucleation and initiation and ultimately failure during operation (Deng, 2018).

The spherical gas pores mainly form from two sources. The protective gas going in the melt pool fails to escape before solidification as a result of the high cooling rates (Leuders et al. 2013). Secondly, entrapped gases in the metal powder during the gas atomization process may lead to porosity in the final part (B. Zhang, Li, and Bai 2017).

Lack-of-fusion (LOF) defects also referred to as incomplete fusion holes are resultant effects of insufficient laser energy to adequately penetrate the melt pool (B. Zhang et al., 2017). Deposition of a new layer before complete melting of the metal powders complicates the re-melt process and can result to formation of incomplete fusion holes (Gong et al., 2014) located between the scanned tracks and the new deposited layer.

2.4.2. Residual Stresses and Cracks

Residual stresses in the SLM process are attributed to the high thermal gradients (L. Parry et al., 2016) (Vastola et al., 2016) and high cooling rates involved in the process due to rapid solidification from the melting temperature to low preheating temperature.

Extensive research identifies residual stresses as a causative effect of part warping, delamination, build-part detachment from the substrate plate (see

Figure 2.12 (a)) and crack formation (see Figure 2.12 (b) (Y. Liu et al., 2016; Mercelis & Kruth, 2006).

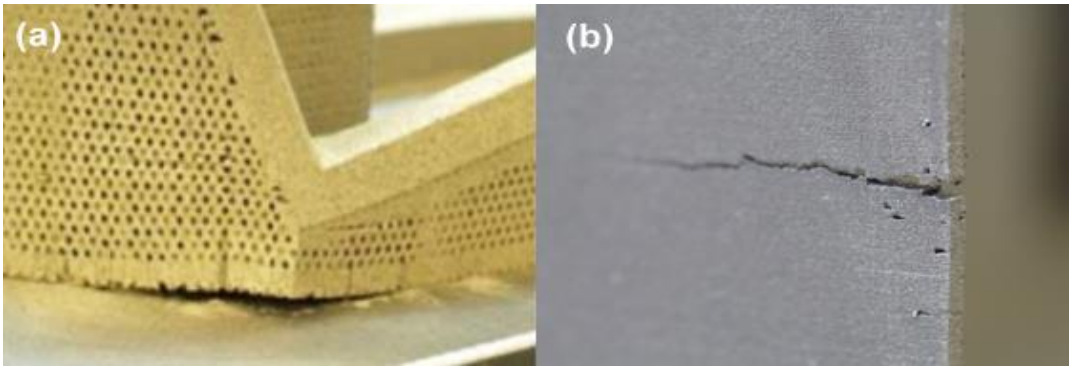

Figure 2.12. Effects of residual stress: (a) build-part detachment from substrate plate (Zaeh & Branner, 2010) and (b) Crack on Ti-6Al-4V part.(L. A. Parry, 2018)

With subsequent layer addition on top melted layers, an increase in residual stresses was observed (Y. Liu et al., 2016) as thermal cycling transforms the tensile stresses on previously formed hotter layers to compressive stresses (Mercelis & Kruth, 2006). As maximum longitudinal residual stresses are attributed to parallel scan vectors that increase in length (Jean Pierre Kruth et al., 2012), available literature scanning strategies that minimize residual stress formation suggests the use of strategies that have minimal increments of the scan vector length (L. A. Parry, 2018). Reduction of the residual stresses causing thermal gradients by preheating has widely been documented in available literature (Ali et al., 2017; Li et al., 2018; Vrancken et al., 2015). However, the machines currently available in the market are limited in terms of preheating temperatures because high temperatures lead to cake formation and difficulties in recycling of the unused powder.

2.5. Modelling Approaches in Selective Laser Melting for Metals

As a laser powder bed fusion AM processes, simulation in SLM can categorized in scale level as micro, meso and macroscopic (Kolossov, 2005). At the macroscopic level,

simulations are performed on a workpiece level to predict residual stresses and distortions by using the part geometry (Kushan et al., 2018; Michaleris, 2014).

SLM simulations at the particle level can be considered to be at micro or meso scale. In this level, modelling is focused on the particle morphology, the laser effect on the melt pool behaviour and the flow of the liquid metal particles (Khairallah et al., 2016). Various numerical techniques such as the finite element (FE) can be used to evaluate phenomena occurring at the particle level which includes the melt pool dynamics (Kushan et al., 2018).

Multi-scale modelling, particularly on a microscopic level facilitates the prediction of mechanical properties of SLM produced parts from the consequential modelling of the material's microstructural evolution. On a macroscopic scale, evaluation of the sintering kinetics and densification process can potentially aid in part geometry prediction.

Thermal aspects of the SLM process such as the heat input, melt pool depth, temperature distribution and history are predicted by the thermal simulation while deformations (part distortion) and residual stresses are predicted by the mechanical simulations (Kushan et al., 2018).

Although SLM modelling research has tremendously increased to industrial demand to make it more predictable, current approaches are centred on the use of thermal modelling techniques paired with various phenomena to simulate key process attributes such as residual stresses, temperature fields, part density or even critical defects such as part distortion.

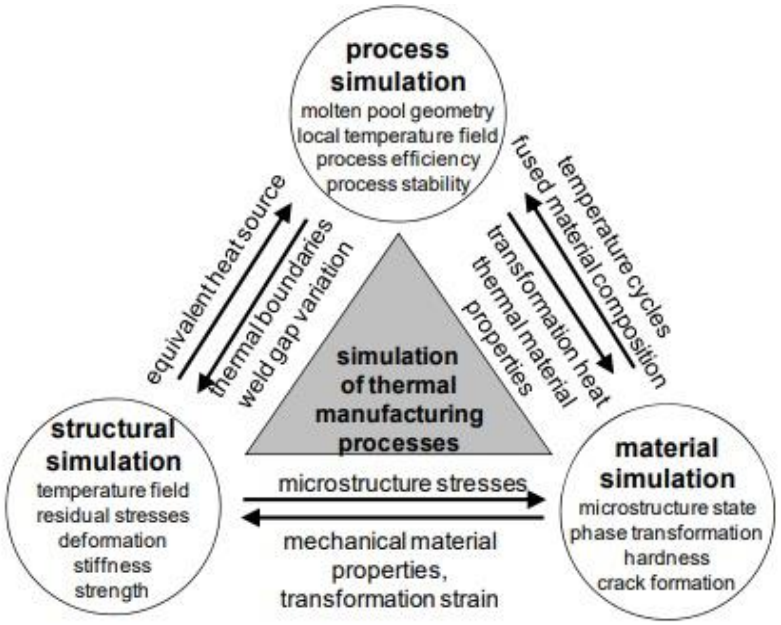

Figure 2.13. The simulation approach for SLM (Papadakis et al., 2012).

Despite the limited availability of modelling tools that can near accurately predict thermo-mechanical cycles and defect causing residual stresses, predictive modelling essentially reduces the time and cost that would otherwise arise from an experimental trial and error approach.

Accurate and effective modelling the SLM process, as with other AM processes, is a challenging task as key aspects of the process may require individual modelling. These include material addition, temperature dependence of the thermal properties, mechanical and thermal boundary conditions. Space and time discretization of the problem to obtain practical results also demands for a comprehensive understanding of available commercial code in addition to immense computational resources.

Validation of the modelled SLM process in such a way that it only predicts the build part history without interfering with the build machine's configuration or operation also presents a modelling difficulty (Gouge & Michaleris, 2017). In their detailed review, King et al. 2015 addressed the complex physics and computational challenges involved in modelling and simulation at both part and powder scales. Modelling challenges can also result from numerical or measurement uncertainties as reviewed by Moges et al. 2019. As a solution to this challenges, Sames et al. 2016, suggested modelling by coupling AM models

across various scales with physics-based attributes such as phase changes and thermo-mechanics.

2.5.1. Part Level Modelling of the SLM Processes

The typical thermomechanical-based FEM system for prediction of residual stresses, distortion and simulation of temperature fields consists of independent thermal and mechanical models and an interaction technique or coupling method (see Figure 2.14).

The pre-processing stage of the thermal model fundamentally allows for a user defined attributes such and inputs such as the CAD part geometry, meshing strategies, governing initial boundary conditions, applied loads and material specific properties. The resultant equations from the discretized governing partial differential equation for all the elements present and their respective solutions are assembled into a global equation in processing stage. Post-processing of the solved global equation provides visual results, such as those of the temperature fields.

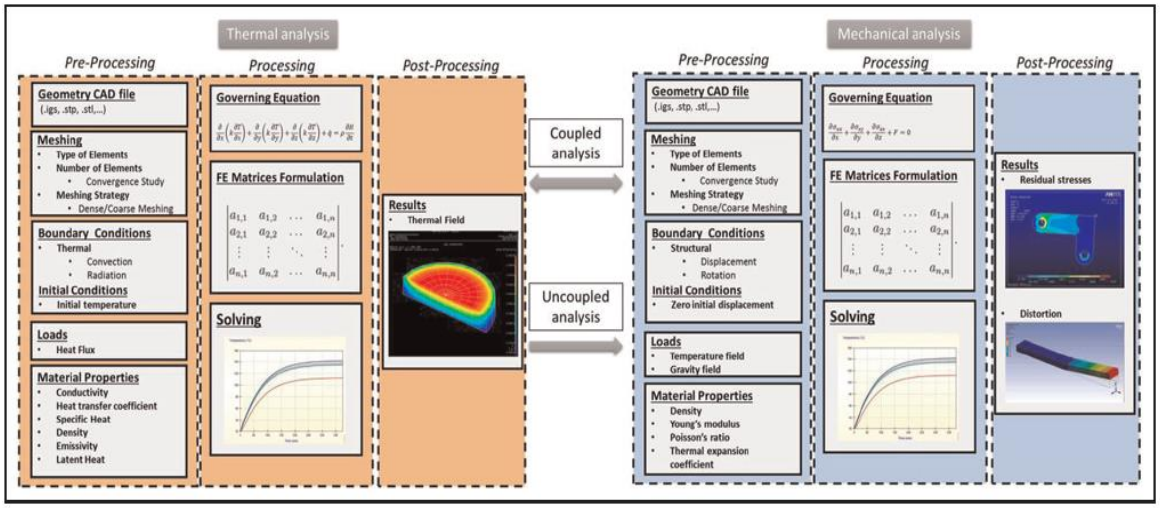

Figure 2.14. Schematic for a typical thermomechanical model for SLM (Schoinochoritis et al. 2015)

The mechanical model that aims to predict residual stresses and distortion on the part geometry follows a similar approach. The previous temperature fields from the thermal model are then incorporated as an applied load (Schoinochoritis et al. 2015).

The interaction criterion to achieve a thermo-mechanical model can in the simplest form be categorized as either be coupled or uncoupled. The uncoupled model is based on the assumption of unidirectional relationship between the thermal and mechanical behaviours. As such, the thermal history only influences the outcome of the mechanical behavior and not vice versa (Lindgren, 2001). Similarly, interactions between thermal history or temperature and mechanical aspects such the stress fields are not analysed (Schoinochoritis et al. 2015).

In the coupled method, as shown in Figure 2.15, analysis of the thermal and mechanical fields are performed in such a way that the converged solution of temperature field from the initial time step is incorporated as an input for subsequent use with the temperature dependent material properties to obtain a new mechanical behavior.

Figure 2.15. Thermal and Mechanical behavioural relationship in a coupled thermo-mechanical model.

Similarly, certain mechanical behaviour such as the plastic deformation is also considered to acquire solutions of the temperature field. As a result, new temperature dependent material properties are generated after solving the thermal field.

2.5.2. Finite Element Modelling

The finite element modelling, FEM, of the SLM process is multifaceted phenomena that integrates a thermal model, a material model and a laser-material interaction model for it to be realized. The thermal model represents the progressive thermal input of moving heat source, while the material and laser-material interaction models define temperature-dependent material properties and account for the occurring transient thermomechanical phenomena, respectively (Fu & Guo, 2014).

Commercially available software used for FEM and simulation include MSC Simufact Additive, Ansys Additive Print, Atlas 3D Sunata, Additive Works Amphyon and Autodesk Netfabb Simulation Utility (Peter et al., 2020).

The part geometry in FEM is divided into elements and nodes that bind adjacent elements together. The processing time is further divided in time steps as a discretization technique that significantly aids in faster solving of the complex transient model solutions. From a modelling perspective, for Direct Energy Deposition (DED), welding and Powder Bed Fusion AM processes, similar approaches to a considerable extent have been adopted while considering their respective limitations (Gouge and Michaleris, 2017). However, the use of a much smaller laser spot size (~100 μm) and the speed of deposition in LPBF and DED respectively that demands for more rigorous spatial and temporal discretization (Denlinger et al., 2016).

As a drawback, discretization methods attributed to finite element modelling of LPBF process consequently result to the need for more computing power. Removal of the built plate (Neugebauer et al., 2014) and assuming perfect insulation capabilities of the metal powder during the thermal analysis (Paul et al., 2014; Song et al., 2015) are some of the strategies that have been applied to reduce the computational times.

Due the complexity and computational strain involved, research has steered towards the use of layer-by-layer simulations and application of analytical methods in an effort to perform moving heat source simulations.

Advancements in finite element modelling and analysis have significantly shortened design-to-part production time spans (Megahed et al., 2016). Models based on a finite element analysis approach to evaluate the causative temperature gradients responsible for residual stress in Ti6Al4V have been also reviewed by Saxena et al. 2016 and Ali, Ghadbeigi, and Mumtaz 2018.

Modelling an AM process using a finite element approach also requires that the thermal losses and the elasto-plastic stresses incurred during the part build process to be

considered. The microstructural and the resultant material property changes are known to further complicate the modelling process.

Material deposition in an existing numeric model consequently results to the addition of new equations. Currently the two general approaches in AM that model material deposition are Quiet and the Dead-Alive methods (Costa et al. 2005; Van Belle et al. 2012) with each method presenting its own advantages and drawbacks. The quiet element method allows for material addition by use of a severe reduction or scaling factor of the material properties in such a way that they can only be realized in the model after deposition of the material elements while the Dead-Alive method allows for addition for new equations over the model's history (Schoinochoritis et al. 2015; Gouge and Michaleris 2017).

The challenge with modelling of the heat source can be attributed to the resultant thermal gradients that arise during melting and the complexities involved in an attempt to measure the precise magnitude and shape of the input energy volume. The thermal losses through conduction, free and forced convection and radiation have to be considered to achieve an effective finite element model.

Temperature dependent material properties that are known to have a particular correlation to thermal history such as the density, emissivity, specific heat capacity and the thermal conductivity (Schoinochoritis et al. 2015), yield strength (L. Ma & Bin, 2007),Young modulus (Jiang et al 2002) and the thermal expansion coefficient (Hussein et al., 2013; Van Belle et al., 2012) have to be considered for accurate modelling as they are likely to contribute, to a certain extent, to residual stresses and part distortion (Schoinochoritis et al. 2015).

3. METHODS AND PROCEDURES

Based on the approach discussed in §2.5.1, thermal and mechanical models for thermomechanical modelling of SLM process using Ti6Al4V were used in this study. Autodesk® Netfabb® Local Simulation (product version 2020) software which uses a non-linear decoupled finite element-based 3D transient thermo-mechanical solver is employed for predictive simulation at a part scale level. As a pre-build analytical and defect prediction tool in this study, Autodesk Netfabb Local Simulation was used to create and analyse both the pre-processing and post-processing part building processes.

3.1. The Weakly Coupled Thermo-Mechanical Model

The weakly coupled modelling approach used this work in which the thermal history is initially investigated and its results are used as thermal load file for subsequent use to simulate a mechanical response was adopted from Autodesk® Netfabb® Local Simulation (product version 2020) software that uses a non-linear decoupled finite element based 3D transient thermo-mechanical solver designed for predictive modelling in both LPBF and DED build process(Autodesk Help, 2020d).

The Galerkin approach has been adopted to form a weak formulation from the governing physics equations that sequentially allows the energy balance and the stress equilibrium to be used as the governing equations for the both the thermal and mechanical problems respectively (Autodesk Help, 2020).

As a result, the weak formulation generates a displacement or temperature solution vectors, U, a residual vector, R. and a stiffness matrix dR/dT. Upon application of the Newton-Raphson method to the initial solution vector estimate, U^0, (3.1). can be used iteratively to obtain a definitive value of the residual vector, R within a particular tolerance. The values U^i and U^{i+1} are preceding and current solution vectors respectively (Autodesk Help, 2020b).

$$U^{i+1} = U^{i} - \left[\frac{dR^{i}}{dU}\right]^{-1} R^{i} \tag{3.1}$$

3.1.1. The Thermal Model

The thermal model used in this work and the governing equations required to obtain the temperature fields as well as the necessary thermal boundary conditions are as incorporated in Autodesk Netfabb Local Simulation's 3D transient thermo-mechanical solver (Autodesk Help, 2020d).

Considering a body with an isotropic specific heat capacity, C_p, at a temperature, T, constant density, ρ, and at a time, t (s), the governing thermal equation required to achieve a thermal equilibrium can be formulated as:

$$\rho C_p \frac{dT}{dt} = -\frac{\partial\left(q_i(x_j, t)\right)}{\partial x_i} + Q(x_j, t) \tag{3.2}$$

where values Q, x_j and q_i are represent the body heat source, position and heat flux vectors respectively. As an initial working condition, the temperature, T_0 is considered to be at an ambient temperature, T_∞. For this work, 25°C was used as the ambient temperature and preheating temperature was 200°C.

$$T_0 = T_\infty \tag{3.3}$$

The heat source and surface heat losses by radiation and convection are then realized by application of a Neumann boundary condition in two parts. From the Fourier's conduction equation, the heat flux vector (q_i) can be expressed as a function of temperature (T) and position vector (x_i) with *k(T)* as the isotropic temperature dependent thermal conductivity.

$$q_i = -k(T)\frac{\partial T}{\partial x_i} \tag{3.4}$$

The temperature for the first-time step is considered to be either equal to the build plate's preheating temperature or the ambient temperature. As initial conditions, the temperatures of the subsequent time steps are then used as nodal temperatures that are discretely obtained from the last completed iterative time step.

The heat source *Q*, in (3.2 is modelled from the Goldak ellipsoid model (see Figure 3.1) that has a three-dimensional (3D) Gaussian distribution (Autodesk Help, 2020c; Denlinger et al., 2016).

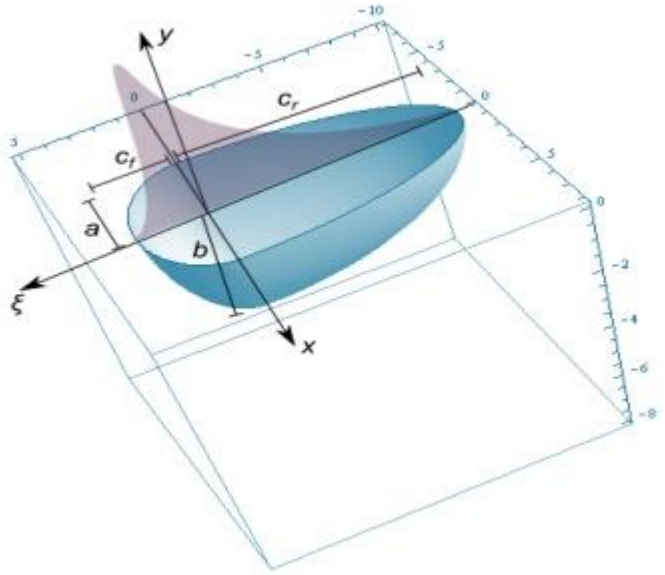

Figure 3.1. Goldak's double ellipsoidal model (Flint et al., 2013; Goldak et al., 1984)

$$Q = \frac{6\sqrt{3}P\eta}{abc\pi\sqrt{\pi}} \exp\left(-\frac{3x^2}{a^2} - \frac{3y^2}{b^2} - \frac{3(z + v_s t)^2}{c^2}\right) \tag{3.5}$$

With a pre-determined laser power, P, and an absorption efficiency, η, the ellipsoidal dimensions; a, b, and c are the corresponding values to the transverse, melt pool depth and longitudinal magnitudes with a moving heat source (the laser) at a speed, v_s. The local coordinates as x, y, and z are also represented in (3.5).

Modelling heat loss by convection and radiation is achieved by the use of Newton's law of cooling and the Stefan-Boltzmann law, respectively. For heat loss by convection, the relationship between the heat flux, q_c, surface temperature, T_s and the heat transfer coefficient, h, is expressed as given in (3.6).

$$q_c = h(T_s - T_\infty) \tag{3.6}$$

With q_{rad} as the heat flux, ϵ as the surface emissivity and σ as the Stefan-Boltzmann constant, the heat loss by radiation is simply modelled from Equation (3.7) below.

$$q_{rad} = \epsilon\sigma\left({T_s}^4 - {T_\infty}^4\right) \tag{3.7}$$

For linearized radiation, (3.7). can be expressed as;

$$q_{rad} = h_{rad}(T_s - T_\infty) \tag{3.8}$$

Where the heat transfer coefficient, h_{rad} can be obtained from the above equations and expressed as (3.9). below

.

$$h_{rad} = \frac{\epsilon\sigma\left({T_s}^4 - {T_\infty}^4\right)}{(T_s - T_\infty)} = \epsilon\sigma\left({T_s}^2 + {T_\infty}^2\right)(T_s + T_\infty) \tag{3.9}$$

3.1.2. The Mechanical Model

The mechanical model as embedded in Autodesk Netfabb Local Simulation's 3D transient thermo-mechanical solver is implemented as follows:(Autodesk Help, 2020d).

The stress equilibrium which is used as the governing equation for mechanical responses is shown in(3.10).;

$$\nabla.\boldsymbol{\sigma} = 0 \tag{3.10}$$

The magnitude of the stress, σ, is obtained as a product of the material's stiffness tensor, C, as a fourth order tensor and the elastic strain, ε_e as in (3.11). below.

$$\boldsymbol{\sigma} = \mathbf{C}\varepsilon_{\mathrm{e}} \tag{3.11}$$

Considering the small deformation theory, the magnitude of the total strain, ε_{T}can be calculated as the sum of the elastic strain, ε_{e} , thermal strain, $\varepsilon_{\mathrm{th}}$, and plastic strain, ε_{p} as shown in (3.12).

$$\varepsilon_{\mathrm{T}} = \varepsilon_{\mathrm{e}} + \varepsilon_{\mathrm{th}} + \varepsilon_{\mathrm{p}} \tag{3.12}$$

The thermal strain for small deformations is calculated through the use of Equations (3.13), (3.14) and (3.15).

$$\varepsilon_{\mathrm{th}} = \varepsilon_{\mathrm{th}} j \tag{3.13}$$

$$\varepsilon_{\mathrm{th}} = \alpha(T - T^{ref}) \tag{3.14}$$

$$j = [1 \quad 1 \quad 1 \quad 0 \quad 0 \quad 0]^T \tag{3.15}$$

where the terms, T^{ref} and α as the reference temperature and the material's thermal expansion coefficient respectively.

For this model, the plastic strains for small deformations are obtained by the implementation of the von Mises yield criterion as well as the Prandtl-Reuss flow rule. The relationship between the yield function, *f*, the von Mises' stress, σ_{von}, flow vector, a_{flow}, the material's yield stress, σ_{yield} as well as the equivalent plastic strain, ε_{q}, is as indicated in Equations (3.16), (3.17) and (3.18).

$$f = \sigma_{von} - \sigma_{yield}(\varepsilon_{\mathrm{q}}, T) \leq 0 \tag{3.16}$$

$$\dot{\varepsilon}_{\mathrm{P}} = \dot{\varepsilon}_{\mathrm{q}} a_{flow} \tag{3.17}$$

$$a_{flow} = \left(\frac{\partial f}{\partial \sigma}\right)^{T} \tag{3.18}$$

Taking into consideration that any large deformations expected in this work may occur in a particular spatial location of a part x and vary to a considerable extent from a relatively undeformed reference, X, the stress equilibrium equation was formulated using P as the first Piola Kirchoff stress tensor as indicated:

$$\nabla_{\mathrm{X}}.P = 0 \tag{3.19}$$

The first Piola Kirchoff stress tensor is obtained using the stress tensor, σ and the determinant of gradient of deformation, J, as in (3.20) below.

$$P = \mathrm{J}\sigma \cdot \mathrm{F}^{-\mathrm{T}} \tag{3.20}$$

Where the deformation gradient, F, with respect to the undeformed reference, X, is:

$$\mathrm{F} = \frac{\mathrm{dx}}{\mathrm{dX}} \tag{3.21}$$

The displacement gradient, D, which is used obtain the Green Strain, E, is the difference between the deformation gradient and the identity matrix, I. as shown in (3.22) below.

$$\mathrm{D} = \mathrm{F} - \mathrm{I} \tag{3.22}$$

The solutions of the Green Strain, E, are then determined as in (3.23) below:

$$\mathrm{E} = \frac{1}{2}((\mathrm{D} + \mathrm{D}^{\mathrm{T}}) + (\mathrm{D} \cdot \mathrm{D}^{\mathrm{T}})) \tag{3.23}$$

3.2. Part Level Multi Scale Simulation

3.2.1. CAD Part Preparation

For this work, Autodesk Netfabb Ultimate 2020.2 and Simulation Utility for Netfabb 2020.2 were used as the FEA simulation and analysis tools on an Intel(R) Core (TM) i7-4700HQ CPU @ 2.40GHz,16 GB RAM PC. The CAD part file for a cabin bracket (see Figure 3.2) designed for the Airbus A350 XWB aircraft was added to Autodesk Netfabb Ultimate for preparation. Using an embedded automatic repair function, the STL file from the CAD part was then created investigated for any mesh related errors such as border edges, intersecting faces or holes.

A closed, error free meshed cabin bracket geometry as depicted in Figure 3.3, required for FEA simulations using Netfabb Ultimate software package was centrally placed on the build platform. The part dimensions were scaled by 60% to fit in a bounding box of 67.54 × 27.30 × 27.09 mm to minimize computational load and simulation times. After executing the part repair functionality embedded in the software, the scaled part was comprised of the properties in Table 3.1.

Figure 3.2. CAD part used for the simulation.

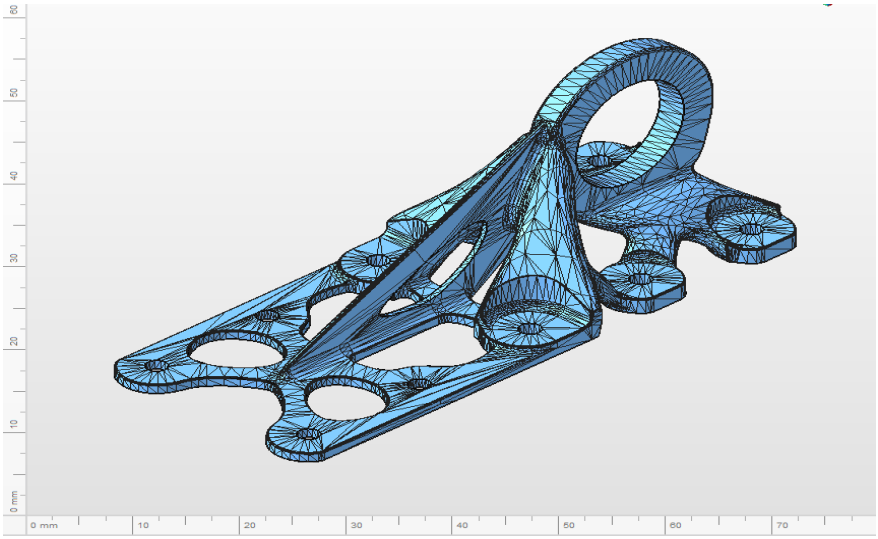

Figure 3.3. The closed, error free mesh used for simulation

Table 3.1. Scaled part properties after STL repair.

Triangles	16908
Edges	25362
Bad Edges	0
Shells	1
Points	8416
Boundary Length (mm)	0

Volume support structures (Figure 3.4 a. and Figure 3.4 c.) that served as both as mitigation aids against part deformation and anchors to the build plate for the cabin bracket were then automatically generated on the critical areas (see Figure 3.4 b) using the default support script for SLM for areas with volume support (see Figure 3.5).

The area with volume support script used in this study consisted of a wired structural pattern with trapeze top and bottom connections to the part. The wired wall pattern as used in volume support that had the properties in Table 3.2.

The new build part and support structures were then imported into Netfabb Simulation Utility in the 3D Manufacturing Format (3MF) type as this file format supports the export and import of part colour and textures that are otherwise not supported by the STL file format.

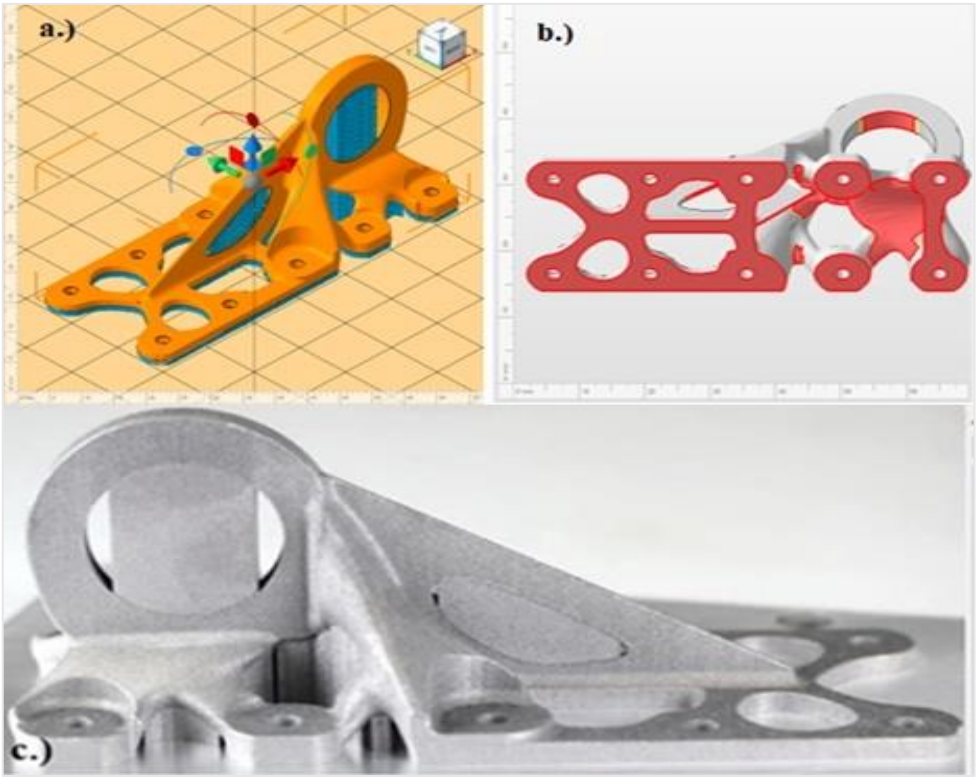

Figure 3.4. a.) Simulated volume support structures b.) Critical areas (in red) that require anchorage. c.) volume support structures on original part.

Table 3.2. Properties of the volume support structures.

Pattern Type	Wired wall
Height	1.30mm
Width	2.33mm
Interval height	0.7mm
Interval width	0.7mm

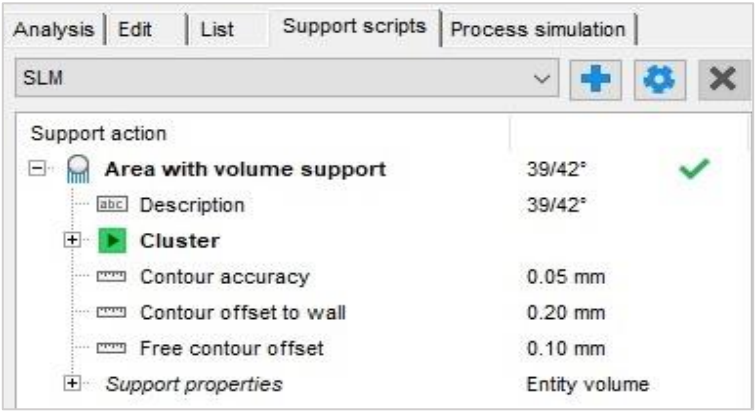

Figure 3.5. Default support script for SLM in Netfabb Simulation Utility.

3.2.2. Material Properties for SLM Ti-6Al-4V powder

The material used for this work was an α–β titanium alloy, Ti-6Al-4V, with the thermal and mechanical properties indicated in Table 3.3 as selected from the Simulation Utility for Netfabb material database. This material properties were referenced from R. R. Boyer 2010; Cardarelli 2001; R. Boyer et al 1994 and MatWeb 2020.

Table 3.3. Thermal and mechanical properties of Ti-6Al-4V powder.

Density (kg/m^3)	4430						
Melting Temperature (°C)	1600						
Emissivity	0.54						
Latent heat of fusion							
Latent heat of fusion (J/kg)	365000						
Solidus Temperature (°C)	1500						
Liquidus Temperature (°C)	1770						
Stress Relaxation Temperature(°C)	690						
Coefficient of Thermal Expansion (CTE)							
Reference Temperature (25°C)							
Temperature (°C)	20				500		
Thermal Expansion (µm/m-°C)	8.6				9.7		
Thermal Conductivity							
Temperature (°C)	93	205	315	425	540	650	
Conductivity (W/m °C)	7.3	9.1	10.6	12.6	14.6	17.5	
Specific Heat							
Temperature (°C)	93	204	315	426	537	649	760
Specific Heat (J/kg/°C)	565	574	603	649	699	770	858
Elastic Modulus							
Temperature (°C)	0				800		
Elastic Modulus (GPa)	105				62.8		
Poisson's Ratio	0.34				0.34		
Plasticity							
Temperature (°C)	0				800		
Stress (MPa)	777				417		
Plastic Strain	0				0		

3.2.3. Process Parameters for Simulation

The simulation utility feature in Autodesk Netfabb was used to create Process Parameter (PRM) files with variable SLM process parameters. With Netfabb, the generated PRM file accounted for the thermal and mechanical properties for the selected Ti-6Al-4V alloy. PRM files with varying process specific parameters, such as the laser power, layer

thickness, heat source absorption efficiency, laser beam diameter and the scan speed were generated (see Figure 3.6) to investigate the effect of their variance during part production on the residual stresses and deformations.

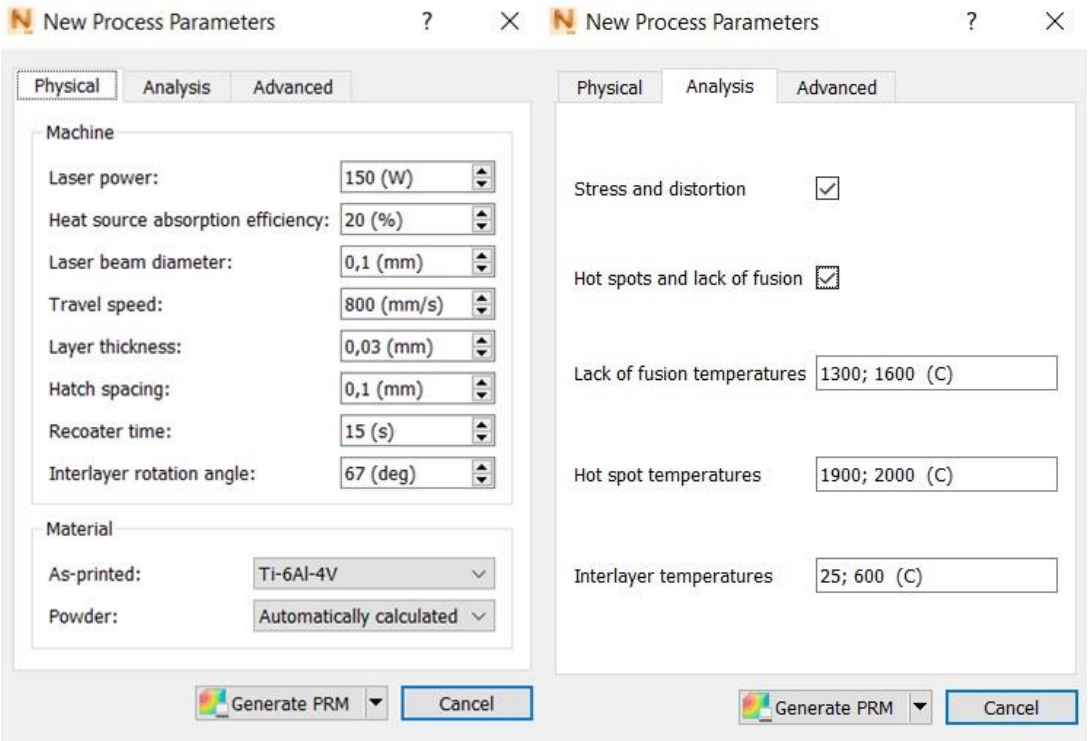

Figure 3.6. Customized Processing Parameter File (PRM) generation interface using Ti6Al4V.

The relationships between the magnitude of various key SLM process inputs, i.e. laser power, scan speeds and layer thickness with regard to crucial aspects that influence the part quality or post-production performance such as the displacement, elastic and plastic strains, Cauchy stresses, von Mises stresses during the fabrication process were simulated and investigated.

Laser power inputs between 150-300 W with increments of 50 W from the preceding power input were applied as indicated in Table 3.4. For the study of the effect of varying scan speeds, travel speeds of 600 mm/s, 800 mm/s,1000 mm/s and 1200 mm/s were selected individually to create PRM files. A similar approach was then used to create PRM files for the investigating the effect of layer thickness with respect to the aforementioned aspects

using layer thickness of 0.02 mm, 0.04 mm and 0.06 mm. The other process parameters were held constant as indicated in Table 3.4 and Table 3.5 respectively. The layer thickness simulations used the process parameters in Table 3.6. The scanning strategy used for his work was linear (one directional) with an interlayer rotation angle of 67° and the homogenized support structures were built with same process parameters as the part.

The "Lack of Fusion temperature" is the temperature below which, the material (in this case Ti6Al4V) fails to melt completely. This can be defined by the material's liquidus or solidus temperature. The "Hot spot temperature" is the temperature at which, if exceeded, predicted overheating capable of deteriorating the build quality is reached (Autodesk Help, 2020e). The temperature used as liquidus temperature for Ti6Al4V was 1600°C (Mishra et al., 2018).

Table 3.4. PRM for varying laser power inputs for Ti-6Al-4V simulations

Laser Power (W)	**150**	**200**	**250**	**300**	**350**
Heat source absorption efficiency (%)	20				
Laser Beam Diameter (mm)	0.1				
Travel Speed (mm/s)	800				
Layer Thickness (mm)	0.03				
Hatch Spacing (mm)	0.1				
Recoater Time (s)	15				
Interlayer rotation angle (deg)	67				
Lack of fusion temperatures (°C)	1300		1600		
Interlayer temperatures (°C)	25 - 600				
Hot spot temperatures (°C)	2000		3000		

The effect of preheating the built plate at 200°C and 450°C using the process parameters in Table 3.4 and a laser power of 150W was investigated. Similarly, the effect of increasing the built plate thickness was also investigated using the process parameters indicated in Table 3.4, a 150W laser power setting and a preheating temperature of 200°C. The built plate thicknesses used for this study were 12.5mm, 25mm and 50mm.

Table 3.5. PRM for varying travel speeds for Ti-6Al-4V simulations.

Travel Speed (mm/s)	**600**	**800**	**1000**	**1200**
Laser Power (W)	150			
Laser Beam Diameter (mm)	0.1			
Heat source absorption efficiency (%)	40			
Layer Thickness (mm)	0.02			
Hatch Spacing (mm)	0.16			
Recoater Time (s)	10			
Interlayer rotation angle (deg)	67			
Lack of fusion temperatures (°C)	1600			
Interlayer temperatures (°C)	25 - 800			
Hot spot temperatures (°C)	1900			

Table 3.6. PRM for varying layer thickness for Ti-6Al-4V simulations.

Layer Thickness (mm)	**0.03**	**0.04**	**0.05**	**0.06**
Laser Power (W)	150			
Laser Beam Diameter (mm)	0.1			
Heat source absorption efficiency (%)	20			
Travel Speed (mm/s)	800			
Hatch Spacing (mm)	0.1			
Recoater Time (s)	15			
Interlayer rotation angle (deg)	67			
Lack of fusion temperatures (°C)	1600 and 1900			
Interlayer temperatures (°C)	25 - 800			
Hot spot temperatures (°C)	1900			

A machine configuration of EOS M 290, a single laser and the generated process parameter file from Netfabb's Processing Parameter (PRM) file data base were then selected for simulation (see Figure 3.7).

The build plate material was set to match the deposition material, in this case Ti-6Al-4V, for the entire simulation. The built plate size was capped to fit the base dimensions of the part and its thickness was set to 50 mm. Built plate thicknesses of 12.5 mm and 25 mm were also used to investigate the effect of varying the built plate thickness. An initial temperature of the build plate was set to 200 °C to mimic the preheating process of typical SLM processes. The bolt release was simulated for the mechanical constrains and the built plate's dimensions were snapped fit the cabin bracket's size (see Figure 3.8).

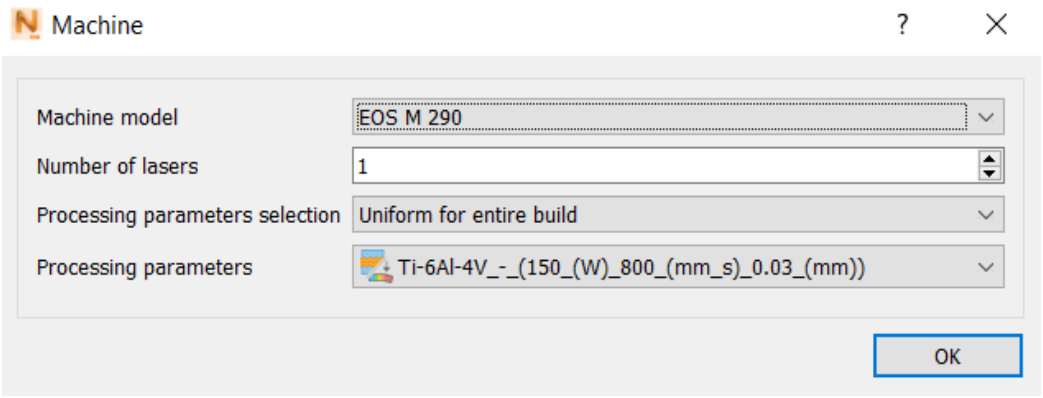

Figure 3.7. Machine Settings interface for Simulation Utility.

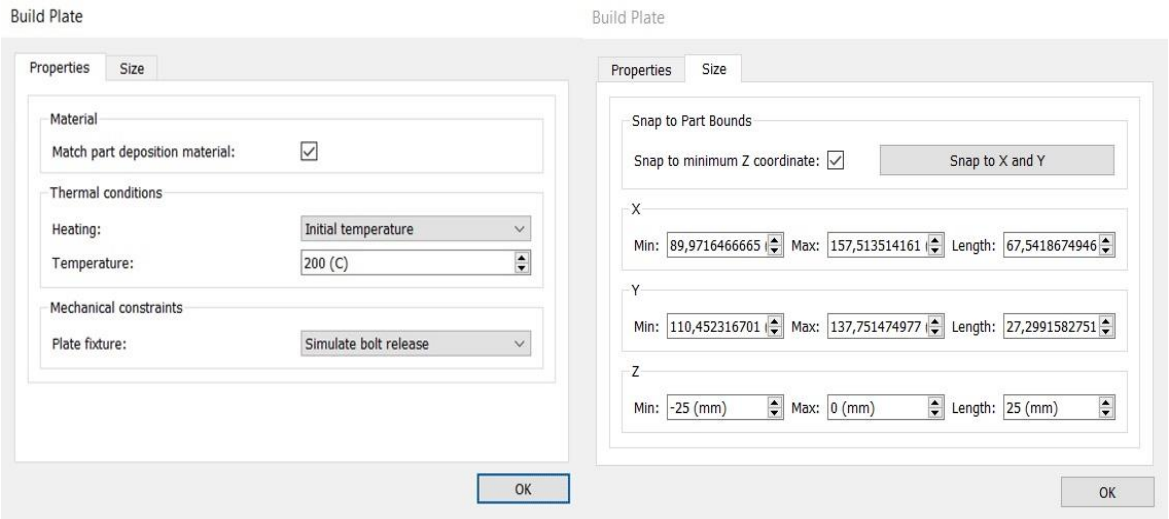

Figure 3.8. Customized built plate size and properties used for the simulations.

The thermal boundary condition of uniform heat loss was applied with a heat loss coefficient of 2.5×10^{-5} W/mm^2 °C that ensured a constant convection boundary condition on every surface of both the part and build plate. This value was obtained from numerous trial and error simulations after comparison with the experimental results used in the validation. The ambient temperature used for the simulation was 25°C (see Figure 3.9).

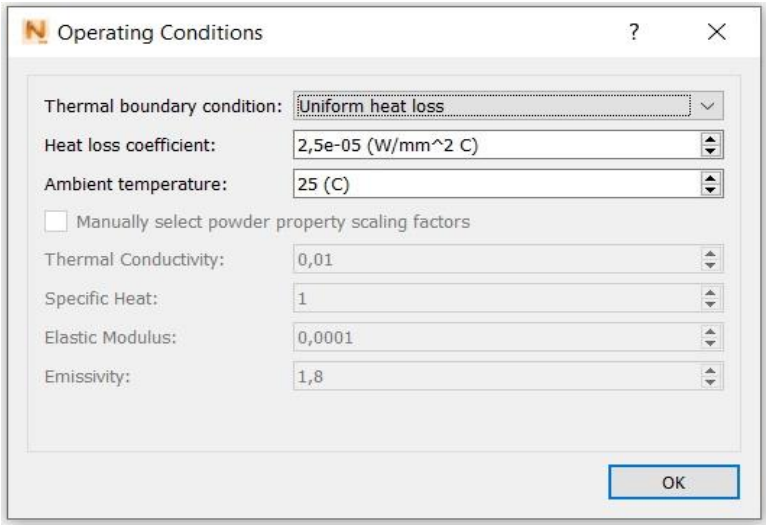

Figure 3.9. Operating conditions used for the simulation.

Heat treatment process was simulated by subjecting the part to 800°C for two hours which was adopted from the EOS Titanium Ti64 Grade 5 material data sheet for the EOS M 290 (EOS GmbH, n.d.). The material annealing temperature was set at 760 °C (Donachie, 2000).

For the solver settings, thermal and mechanical analysis was selected to allow the software to calculate and generate results in terms of the thermal gradients, Cauchy stresses, von Mises and principal stresses as well as the elastic and plastic strain. The structural plasticity simulation option was also selected to enable the calculation of plasticity effects on the model (see Figure 3.10).

The recoater tolerance, as used in Simulation Utility for Netfabb, is the clearance between the recoater blade and the point at which maximum upward deflection of a previous build occurred. This customizable clearance was expressed as a percentage of the depth of the last formed powder layer.

The default recoater tolerance of 80% in Netfabb Simulation Utility as shown in Figure 3.10 was used to guarantee that previously formed layers could not deflect upwards or overlap by margins greater than 20% of into the newly formed layer. Any deflection that occurred beyond the 20% limit was automatically recorded as a recoater blade interference assuming that a solid hard recoating blade is employed.

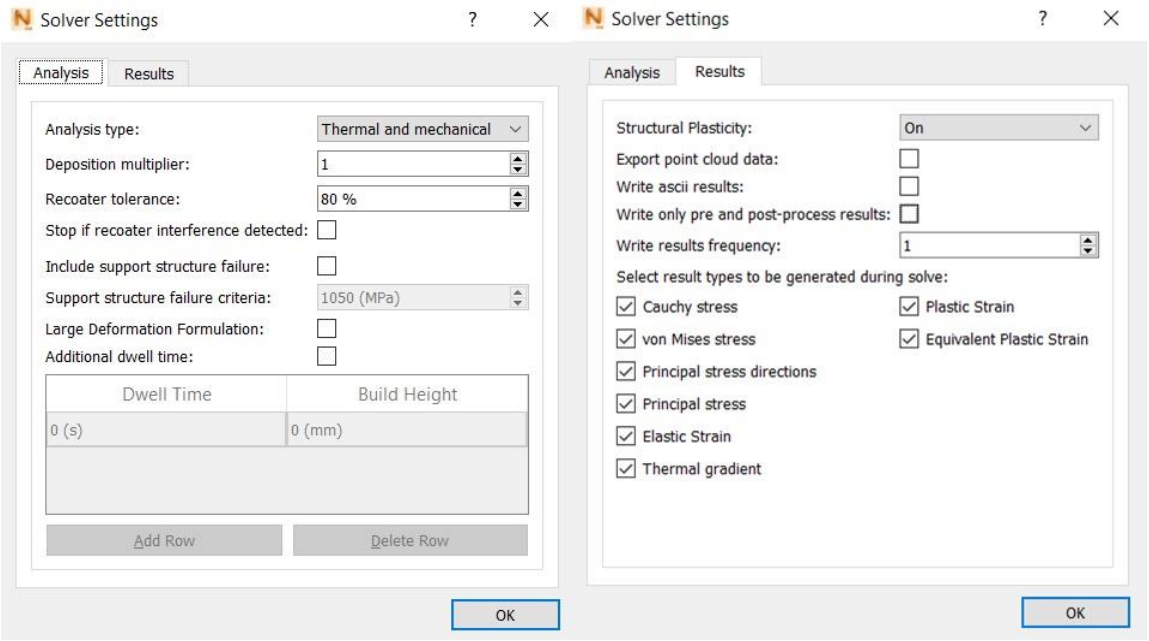

Figure 3.10. Solver Settings used for the simulations.

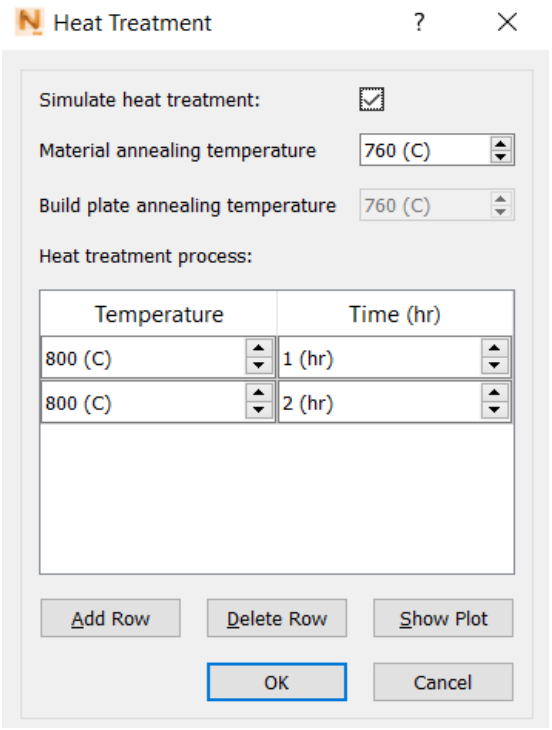

Figure 3.11. Heat treatment process used for simulation.

3.2.4. Mesh Generation and Solving

The meshing method for this work was based on a wall thickness approach to create auto-generated meshes. This approach was dependent on the minimum wall thickness and a

selected padding tolerance. The “Padding Tolerance” of 0.05mm was used to ensure that the STL part could be expanded by 0.05mm in any direction.

The wall thickness test was passed when a minimum thickness threshold of 1.00 mm and surface threshold of 12% was used in the wall thickness analysis tool in Netfabb. For the mesh density settings using the wall thickness approach, Netfabb Local Simulation 2019 is configured to allow for accuracy levels - Fastest, Fast, Accurate and Most Accurate with each level allowing a particular number of minimum elements and coarse generations as shown in Table 3.7.

Table 3.7. Accuracy Options for Mesh Settings in Netfabb Local Simulation 2019

Accuracy	**Number of Elements in the minimum wall thickness**	**Coarsening generations**
Fastest	2	3
Fast	2	2
Accurate	3	1
Most Accurate	4	0

The meshes generated from the fastest, fast and accurate options were then investigated to evaluate the best option for this simulation. The “Accurate” option was selected (see Figure 3.12) as it presented geometrically accurate meshing within considerable computational times as shown in Figure 3.13.

The “Accurate” option ensured that the thinnest geometric part contained at least two elements as recommended simulation criteria in the software manual to allow part distortion (Autodesk Help, 2020). A maximum adaptivity level of 5 was used in this work as recommended by Netfabb for powder bed-based simulations. This ensured that for any given simulation, the mesh could only be coarsened up to a maximum of five times.

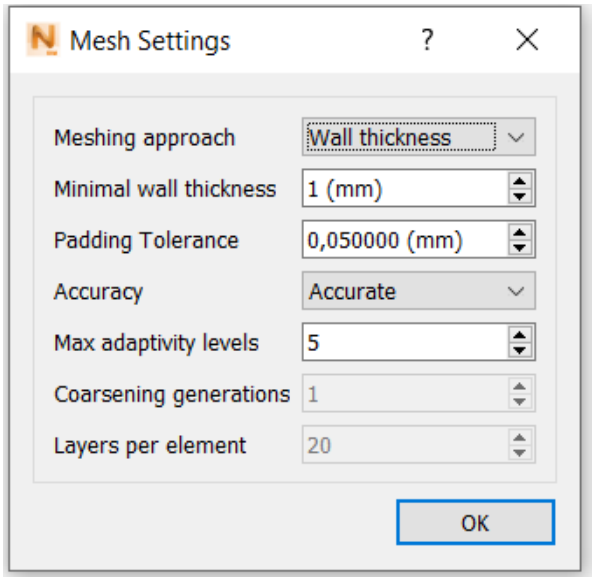

Figure 3.12. Mesh Settings selected for simulation.

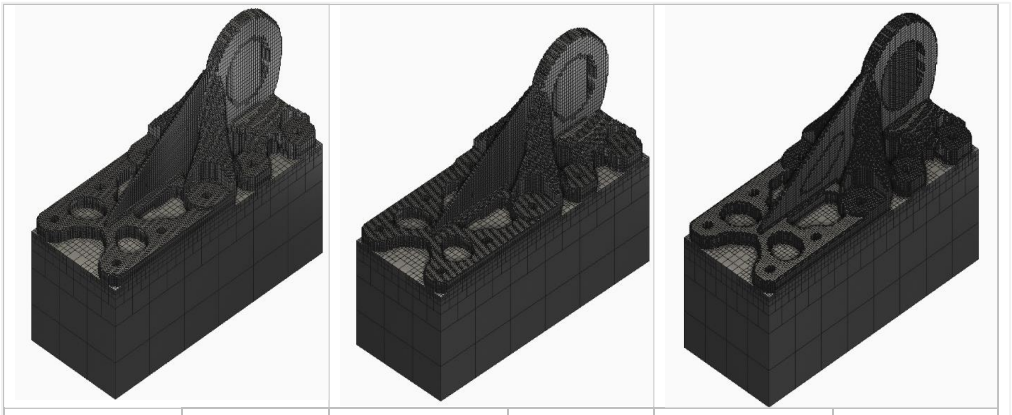

Meshing Option:	Fastest	Meshing Option:	Fast	Meshing Option:	Accurate
Elements:	73173	**Elements:**	73173	**Elements:**	135895
Nodes:	124041	**Nodes:**	124041	**Nodes:**	228609
Layer-Nodes:	1240410	**Layer-Nodes:**	2356779	**Layer-Nodes:**	12116277

Figure 3.13. Generated Meshes for the Fastest, Fast and Accurate options.

3.3. Powder Bed Part-Level Analysis of the Simulation Results

The effects of increasing process parameters such the laser power, scan speed and layer thickness on the thermal gradients, temperature histories, displacement magnitudes, Cauchy and von Misses' stress magnitudes were investigated at an infinitesimal level using five nodal points (see Figure 3.14) during various build times.

Using the process parameters generated in the PRM file as explained in section 3.2.3, the simulations, the results for the varying laser power and scan speed simulations were investigated after varying build times. For the laser power simulations, the thermal results were investigated after 354s, 1185s, 2529s 7055s, 9993s, 11972s, 16175s and after heat treatment which occurred after 123511 s. The mechanical results were further investigated after heat treatment, substrate removal and support removal operations were completed.

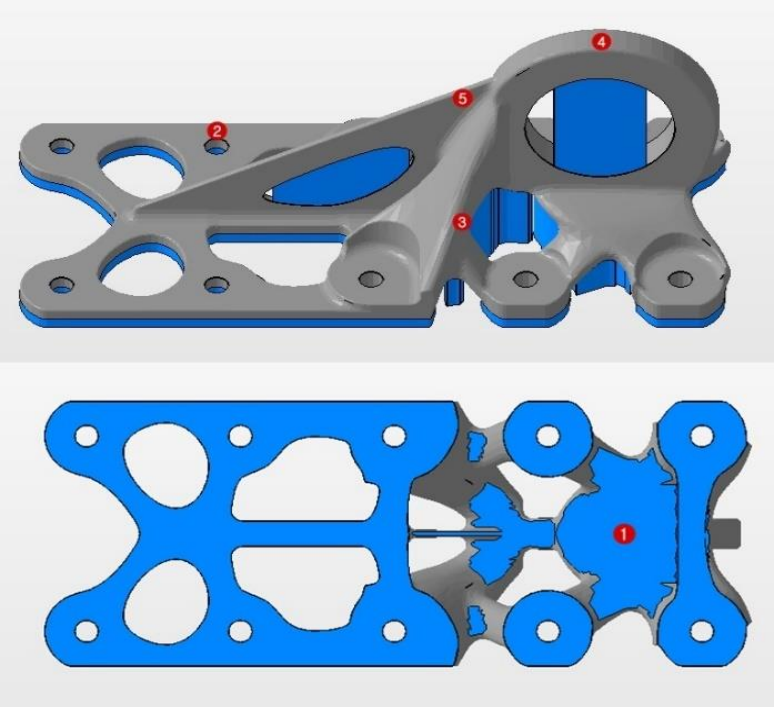

Figure 3.14. The location of the 5 nodes on the part geometry.

Table 3.8. Selected nodal points for the investigation of the effect of varying laser power and scan speeds and their respective x, y and z coordinates.

	Node location	**X (mm)**	**Y (mm)**	**Z (mm)**
Node 1	Support Structure	144.85	124.10	0.00
Node 2	Solid Part	108.44	136.47	1.62
Node 3	Solid Part	132.71	115.14	3.24
Node 4	Solid Part	145.90	124.10	28.08
Node 5	Solid Part	129.02	124.10	19.44

The effect of increasing layer thickness from 0.03 mm to 0.06 mm by increments of 0.01mm was investigated using thermo-mechanical results from the five nodal points (see Table 3.4.)

Using these nodal points, the predicted extent at which lack of fusion volume percentages at 1300°C and at 1600°C as well as the hot spot volume percentages at temperatures above 1900°C after heat treatment phase were also investigated and compared with the results emanating from proceeding increments the same parameters.

4. RESULTS AND DISCUSSION

4.1. Model Validation

The simulation results obtained from the use of Autodesk Netfabb Simulation's Pan Solver have been extensively validated using experimentally obtained results in numerous studies. In one particular study by Yılmaz et al. 2020 done to investigate the effect of single and multiple part production by SLM on the displacement and residual stresses.

The comparison between results from the experimental and Finite Element Analysis for the maximum temperatures using Ti6Al4V was 93% (see Figure 4.1). The experimentally measured temperatures were accurately obtained using a thermal-imaging camera using a thermal emissivity constant of 0.34.

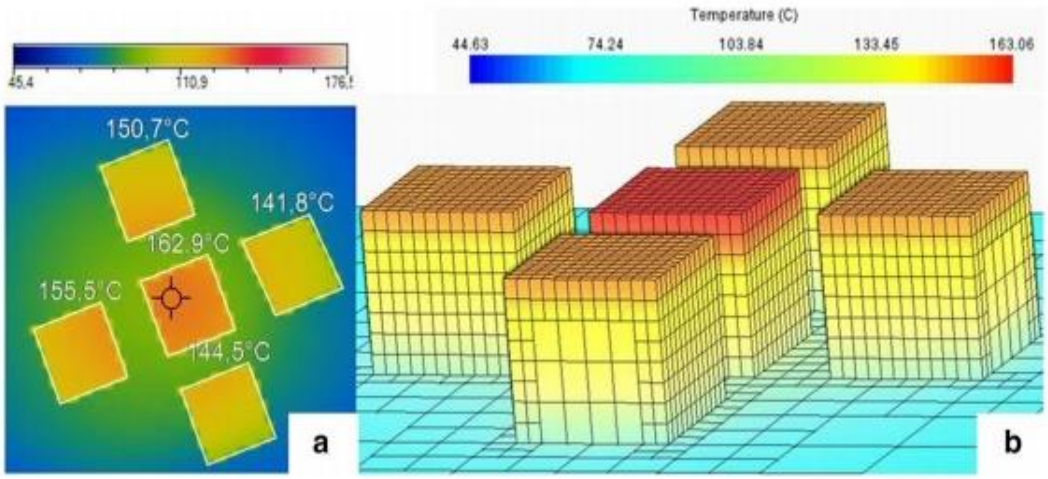

Figure 4.1. Results from a). experimental and b). FEA simulation (Yılmaz & Kayacan, 2020).

Denlinger et al. 2017 in their in situ experimental validation of temperature and distortion measurements by the Laser Powder-Bed Fusion process comparison between the experimental in situ measurements and simulated results yielded a 5% maximum error. In the thermomechanical modelling of large parts in additive manufacturing, Denlinger et al.

2014 obtained a maximum difference of 29% between the experimental and simulation results.

To validate the model used in this work, experimental results for displacements obtained by Dunbar, 2016 were compared with the simulation results. In his work, Dunbar, 2016 used an EOS 280 machine, default Ti6Al4V material properties as supplied by the manufacturer and a model geometry of 31.8 × 31.8 × 0.24 mm placed on a built plate of 89.0 × 36.9 × 3.2 mm (see Figure 4.2). The completed build part is shown in Figure 4.3.

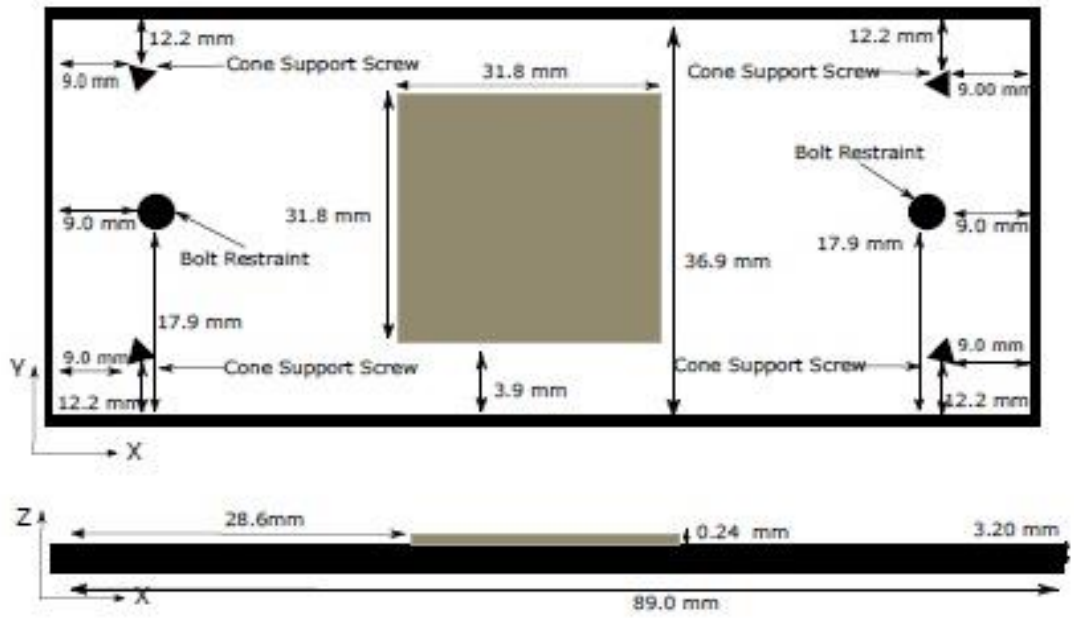

Figure 4.2. Build geometry and substrate dimensions for the experiment (Dunbar, 2016).

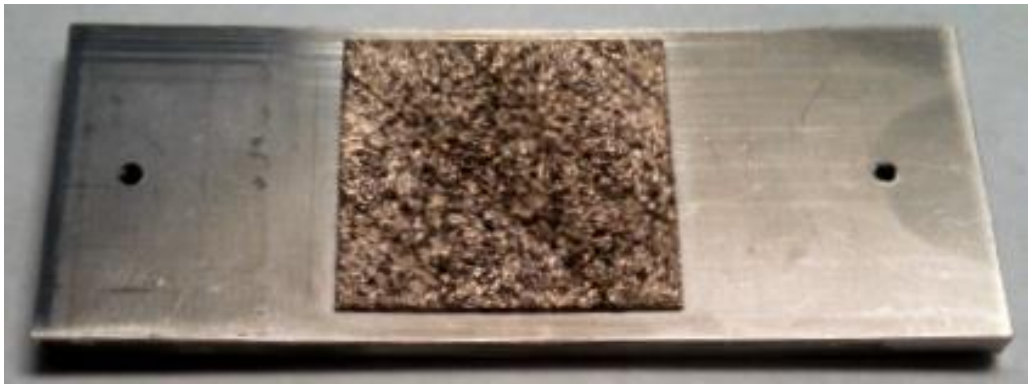

Figure 4.3. Completed build part with similar geometry (Dunbar, 2016).

Similar processing parameters as used by Dunbar, 2016 (see Table 4.1) were used to create a processing parameter file (PRM) as shown in Figure 4.4 to mimic the exact experimental process. The displacement in the build direction was measured using a differential variable reluctance transducer (DVRT) while the temperatures were measured using K-Type thermocouples (TC). The differences between the experimental and simulation results were then investigated to determine the accuracy of our model.

Table 4.1. Processing parameters as used in the experiment (Dunbar, 2016).

Processing Parameter	**Magnitude**
Laser Power	280 W
Scan Speed	1200 mm/s
Layer Thickness	30 µm
Hatch Spacing	0.14 mm
Hatch Rotation	67 deg

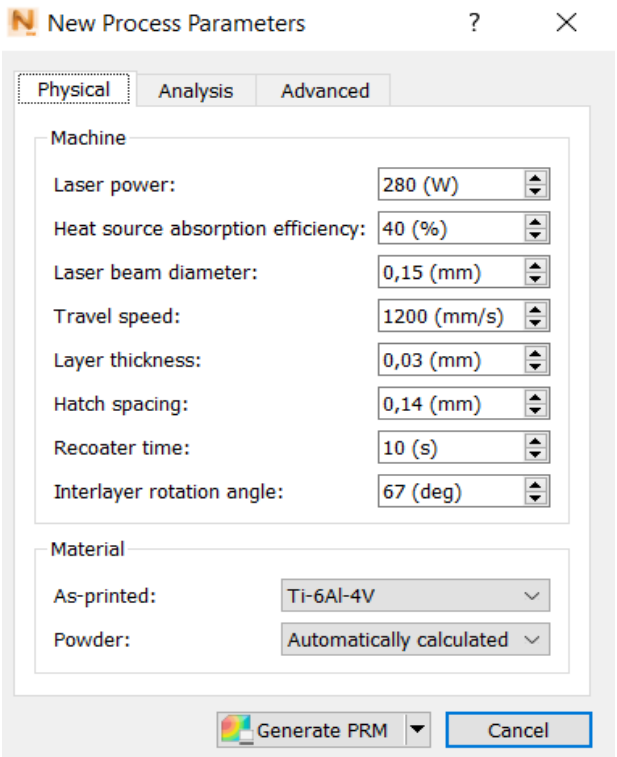

Figure 4.4. Processing parameters as used for the simulation.

Using a layer-based approach, mesh settings shown in Table 4.2 were used to generate a mesh of both the part and substrate as shown in Figure 4.5 b. The displacement

results from the simulation were as indicated in Figure 4.8. The probe tool in Simulation Utility software was then used to acquire the distortion magnitudes that corresponded to the exact positions as measured using the differential variable reluctance transducer (DVRT).

Table 4.2. Mesh settings used for simulation.

Mesh Parameter	**Magnitude**
Maximum adaptivity level	3
Coarsening Generation	1
Layer per element	8

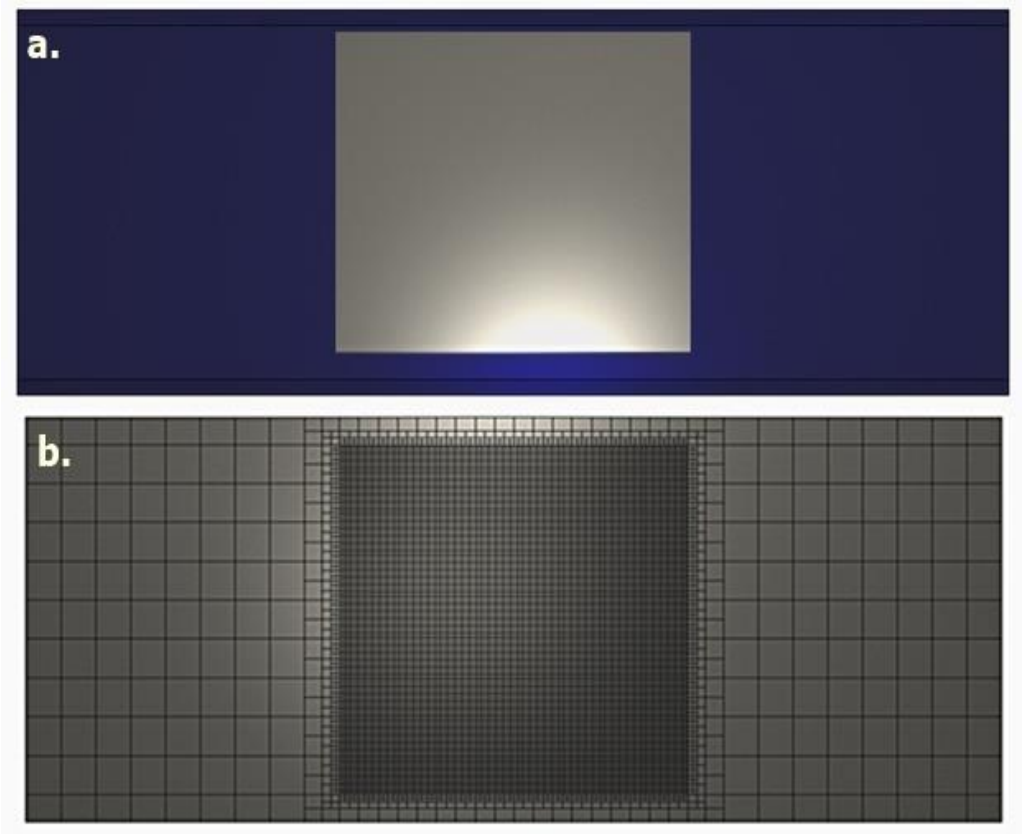

Figure 4.5. Part Simulation a). Part on the substrate and b.) Mesh results.

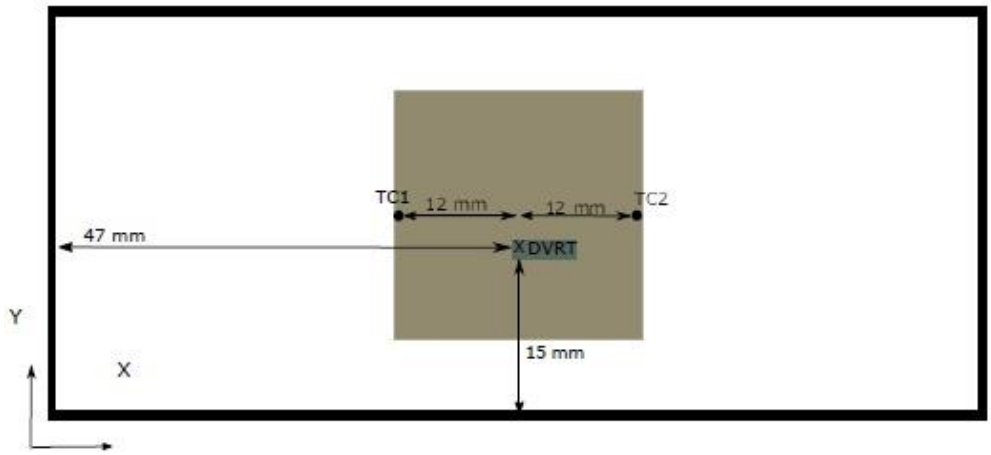

Figure 4.6. Point X where the distortion was experimentally measured.

The experimentally measured final distortion on point X (see Figure 4.6) by the DVRT sensor was 0.67mm (see Figure 4.7). The measured displacement magnitude on the simulation results that corresponds to point X as shown in Figure 4.8 was 0.47mm. This corresponded to a 29.9% maximum error. The magnitude for this error could be attributed to possibility that the simulation was done using a thermal boundary condition that estimated heat loss as opposed to one that allowed conduction to loose powder.

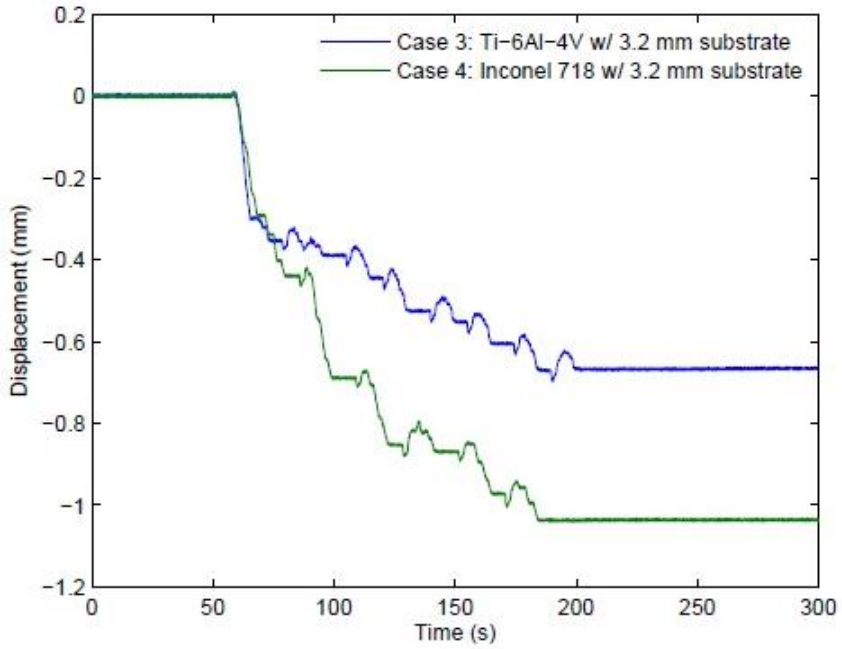

Figure 4.7. Distortion in the Z axis using a 3.20mm thick build plate (Dunbar, 2016).

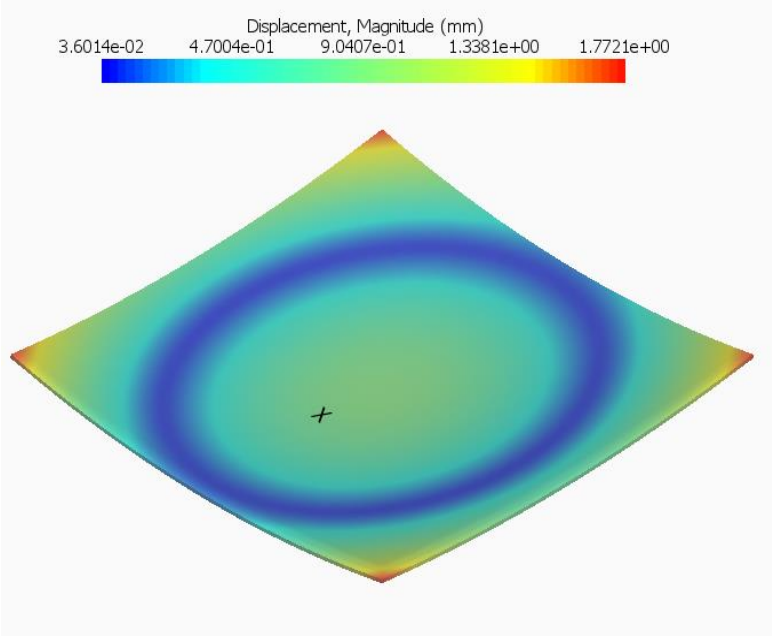

Figure 4.8. Simulated displacement magnitudes and the corresponding location of point X.

4.2. Effect of Increasing Laser Power

The first layer of the part was built at a z height of 1.62 mm after completion of a two-layer support structure after 708 s. The support structure matching the Ti-6Al-4V deposition material was then created after a z height of 0.54 mm. Both the part and support structure were then created simultaneously until the maximum z build height of 28.62 mm. The predicted thermal gradients using Autodesk® Netfabb® Local Simulation utility were only availed after heat treatment stage and not after substrate and support removal. Regardless of the laser power, each of the five simulations had 135863 elements, 228564 nodes and a build completion time of 123511 s (approx. 34.3 hours).

4.2.1. Temperature History and Thermal Gradients

After completion of the first six-layer groups, which consisted of both the part and support structures, it was observed that the maximum temperature at each layer occurred at same build part location regardless of the laser power settings. However, the maximum temperature increased with the addition of each new layer and with each 50 W increment in laser power as shown in Figure 4.9.

The distinctive sharp increase in the maximum temperature in the third layer group (see Figure 4.9) which was primarily the first non-support structure layer of the build part after the completion of the second layer group could be attributed to the lattice structures of the support structures which could have acted as a “heat sink” for the downward dissipation of the heat energy.

Fluctuations in the maximum temperatures and thermal gradients observed in next layer groups until build completion were possibly due to the varying geometrical profiles as shown in Figure 4.10.

After heat treatment, the maximum temperature for all the simulations was about 767°C which was close enough to the selected annealing temperature of 760°C. This stabilization in temperature could have resulted from the completion of the manufacturer’s recommended heat treatment whose objective was to relieve impending residual stresses and increase the Ti6Al4V alloy material’s ductility.

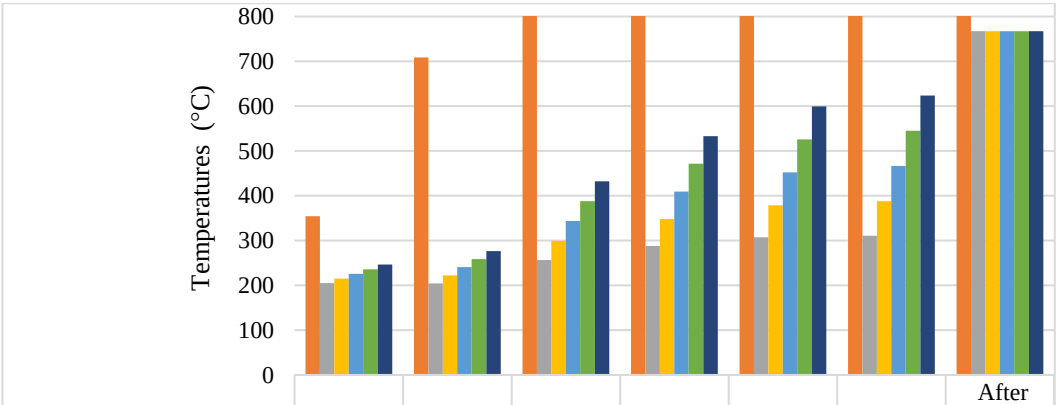

	Layer 1	Layer 2	Layer 3	Layer 4	Layer 5	Layer 6	After Heat Treatment
Time (s)	354.11	708.35	1184.82	1663.69	2139.06	2528.83	123511.29
150 W	204.69	204.63	256.52	288.13	307.35	310.86	767.48
200W	214.94	222.35	299.51	347.97	378.91	387.73	766.93
250W	225.39	240.4	343.67	409.58	452.42	466.38	766.93
300W	235.84	258.45	387.83	471.2	525.92	545.03	766.93
350W	246.29	276.5	431.99	532.81	599.43	623.68	766.93

Figure 4.9. Maximum temperatures at the first six layer groups and after heat treatment.

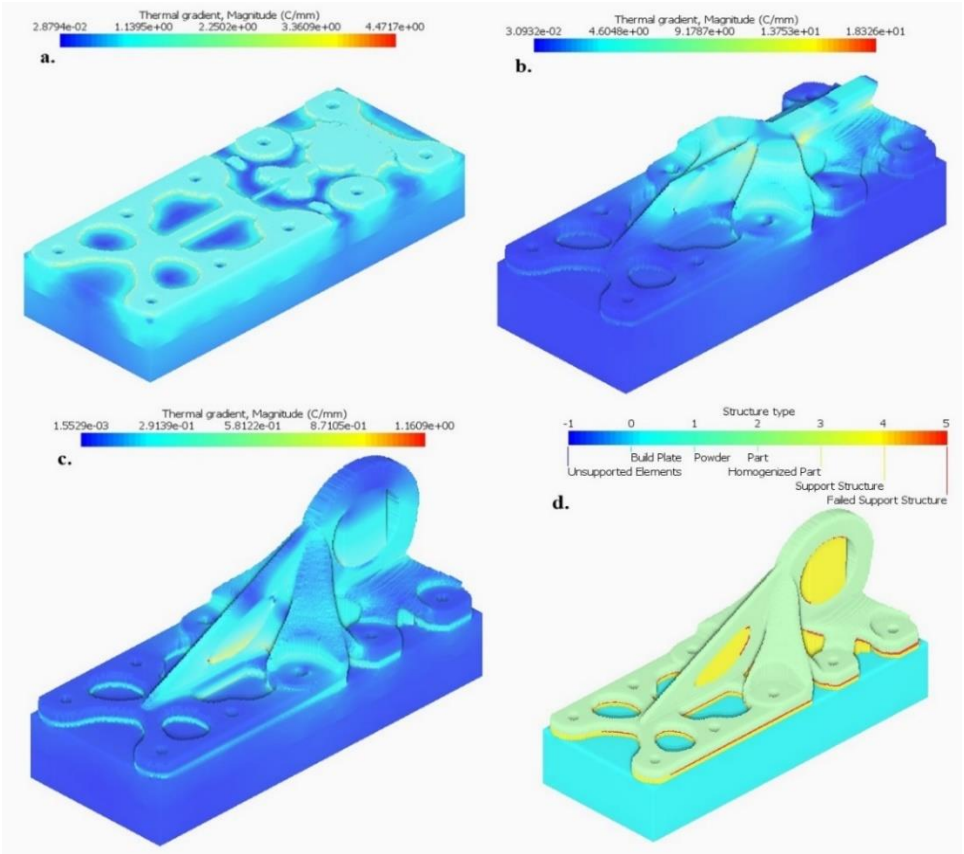

Figure 4.10. Build simulation using a 300W laser at: a.) 354 s, b.) 7055 s c.) 16175 s and d.) after heat treatment.

As expected, the thermal gradient on the z axis at node 1 and 3 (see Figure 4.11.) increased with increasing laser power. Similarly, an increase in the thermal gradients along the same axis over time within the same laser power setting was evident, possibly due to the preheating effect from the newly formed layers.

After 7055 s, at which the build height was at 10.80 mm, the predicted thermal gradients at node 3 on the x, y and z direction were considerably higher than those of node 1 for all the all the laser power settings. It was also observed that their magnitudes were highest in the z axis and least in the x axis.

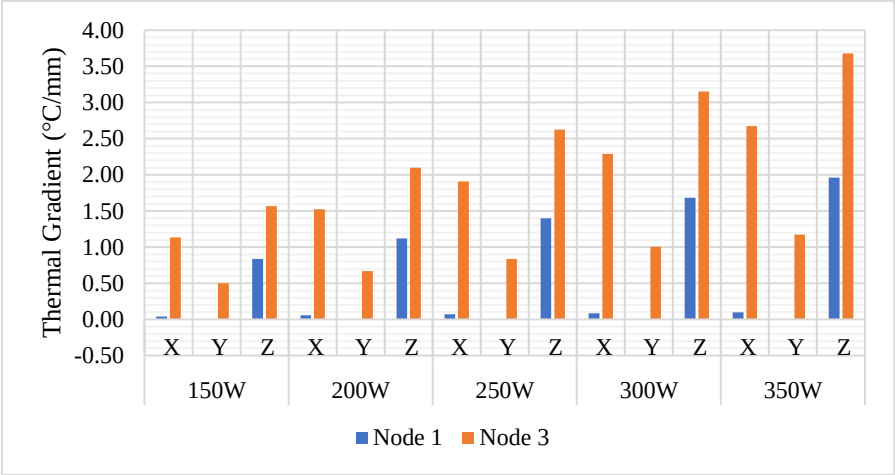

Figure 4.11. Thermal Gradients at node 1 (support structure) and node 3 (build part) at 7055s.

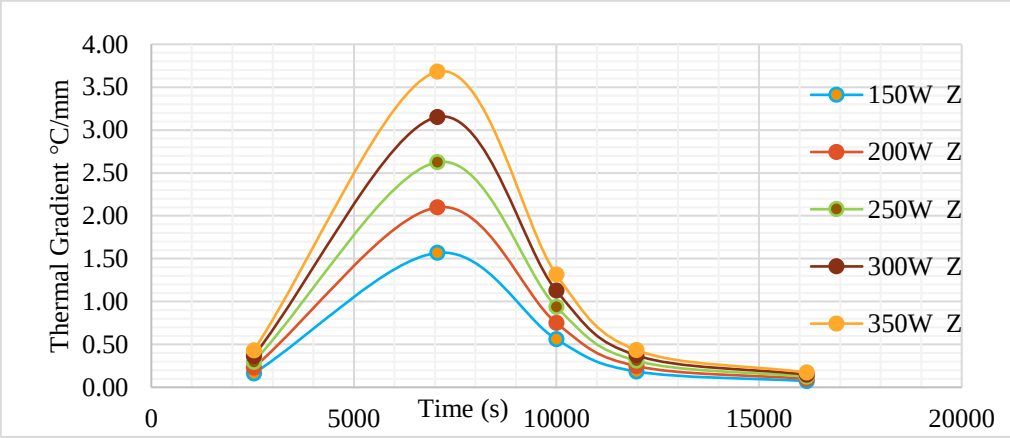

Figure 4.12. Thermal Gradients on the z axis at node 3 at build time of 7055 s.

The decline in the thermal gradients in the z axis that occurred after 7055 s for all the five laser power simulations as shown in Figure 4.12 could be as a result of the increased heat dissipation towards the substrate as the previously formed layers could now conduct more heat towards the much cooler regions closer to the substrate

.

Although node 5 had the highest thermal gradients on the z axis compared to node 1 and 3 after printing the last layer at 16175s as shown in Figure 4.13, the thermal gradients in all the three nodes increased with increasing laser power settings. After heat treatment, all the thermal gradients in the same axis at the five nodes were evened out to equal values with the highest occurring in the Z axis as shown in Figure 4.14. Compared to the thermal

gradients in the last build layer before heat treatment at 16175 s, a significant decline in the thermal gradient was achieved from heat treatment.

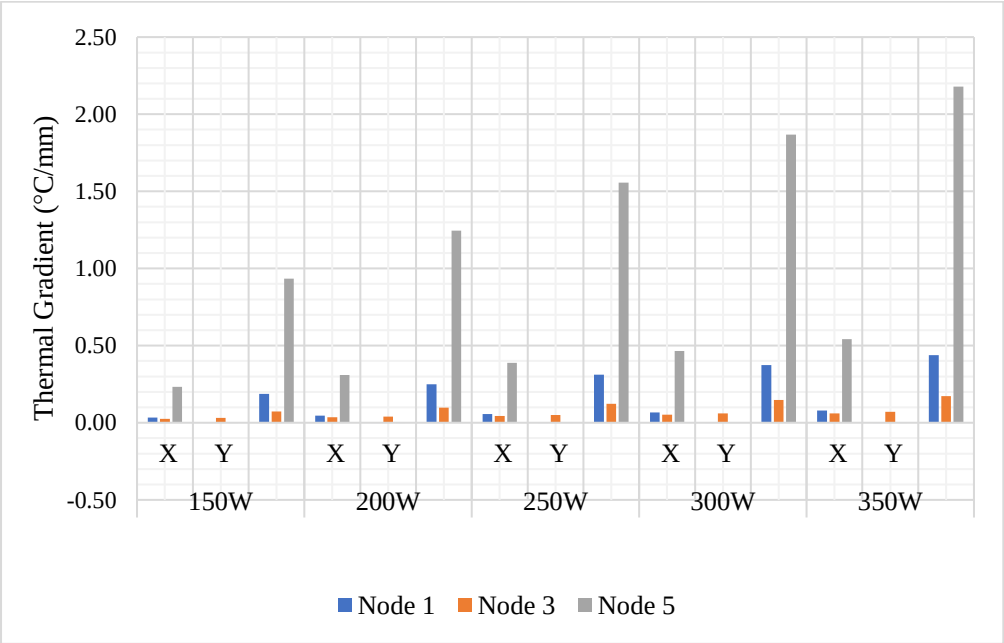

Figure 4.13. Thermal Gradients at node 1, 3 and 5 for 150–350W laser power simulations at the last build layer.

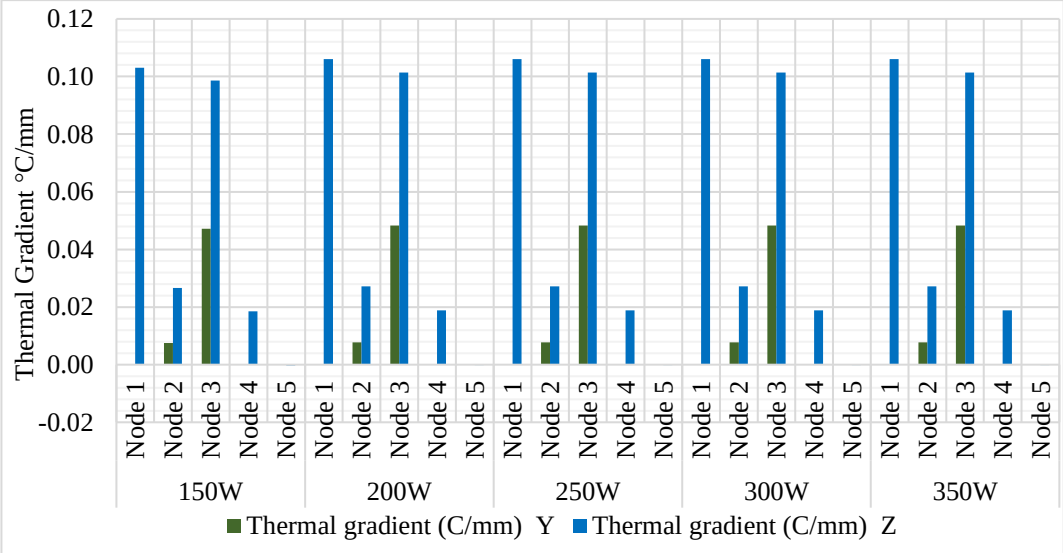

Figure 4.14. Thermal gradients after heat treatment at 123511 s.

4.2.2. Interlayer Temperatures

The interlayer temperatures for all the node points increased with increments of laser power after heat treatment (see Figure 4.15) due to the resultant increase in heat energy arising from the increased laser power. The higher interlayer temperatures at the part's base as indicated in Figure 4.16 were possibly as a result of the preheating effect of the substrate.

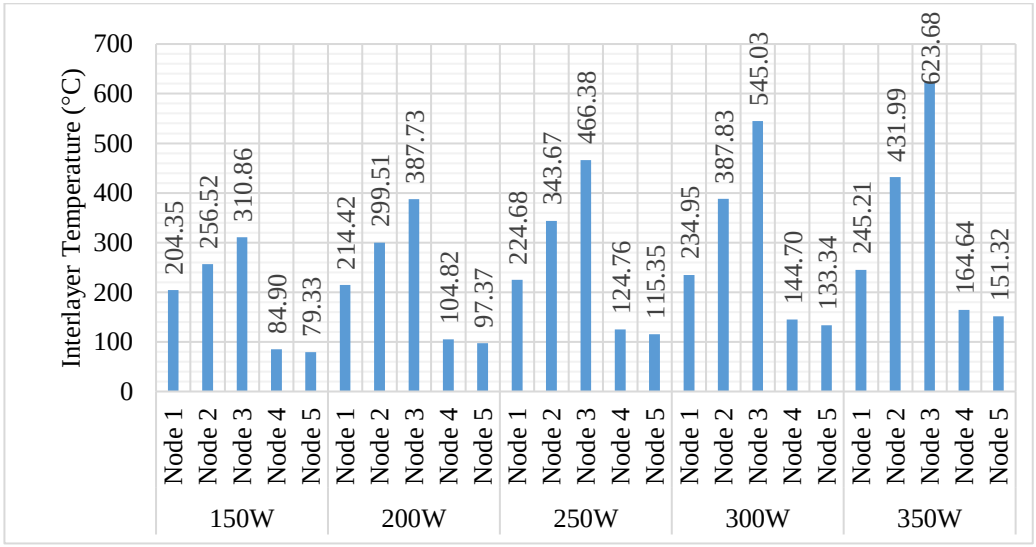

Figure 4.15. Effect of increasing laser power on the interlayer temperatures after heat treatment at 123511 s at the nodes.

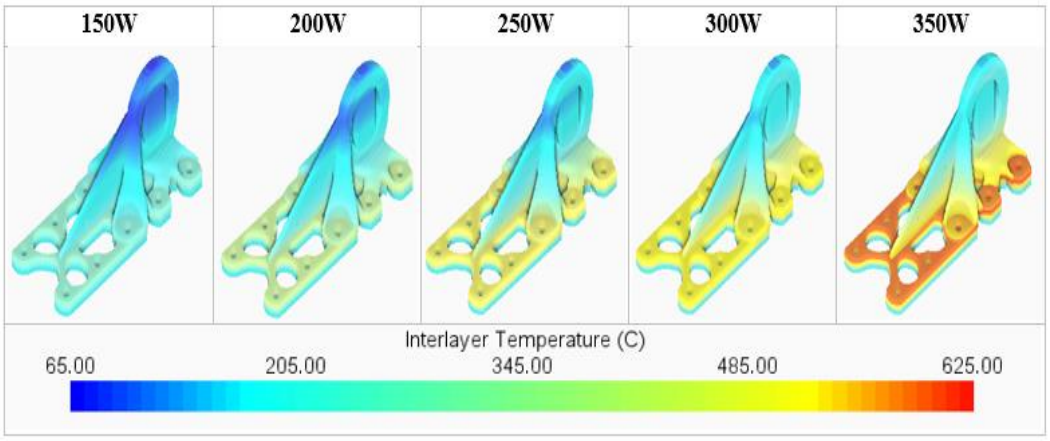

Figure 4.16. Global effect of increasing laser power on the interlayer temperatures.

4.2.3. Displacement Results

After applying heat treatment, the overall displacement profile was identical regardless of the laser power (see Figure 4.17 a.) with the maximum displacements for the entire build occurring at the node point located at x: 156.99 y:135.19 z:1.08 mm (see Figure 4.17 b.). The maximum displacement values of 0.68 mm, 0.58 mm, 0.57 mm, 0.57 mm and 0.52 mm were obtained using the 150 W, 200 W, 250 W, 300 W and 350 W laser powers respectively.

After removing the build plate and supports, the displacement magnitude declined rapidly. This could have been attributed to the possibility that the built plate which matched the Ti6Al4V deposition material could have experienced some distortion and hence its removal resulted to a slight decrease in displacement.

The influence of increased laser power on the displacement across the five laser powers settings for both the entire build as shown in Figure 4.18 and at the nodal points (see Figure 4.19.) was not directly correlated.

Part warpage observed using a magnification factor of 5 indicated upward part warpage at the base positions as illustrated in Figure 4.17. c. compared to a displacement compensated part depicted in Figure 4.17 d.

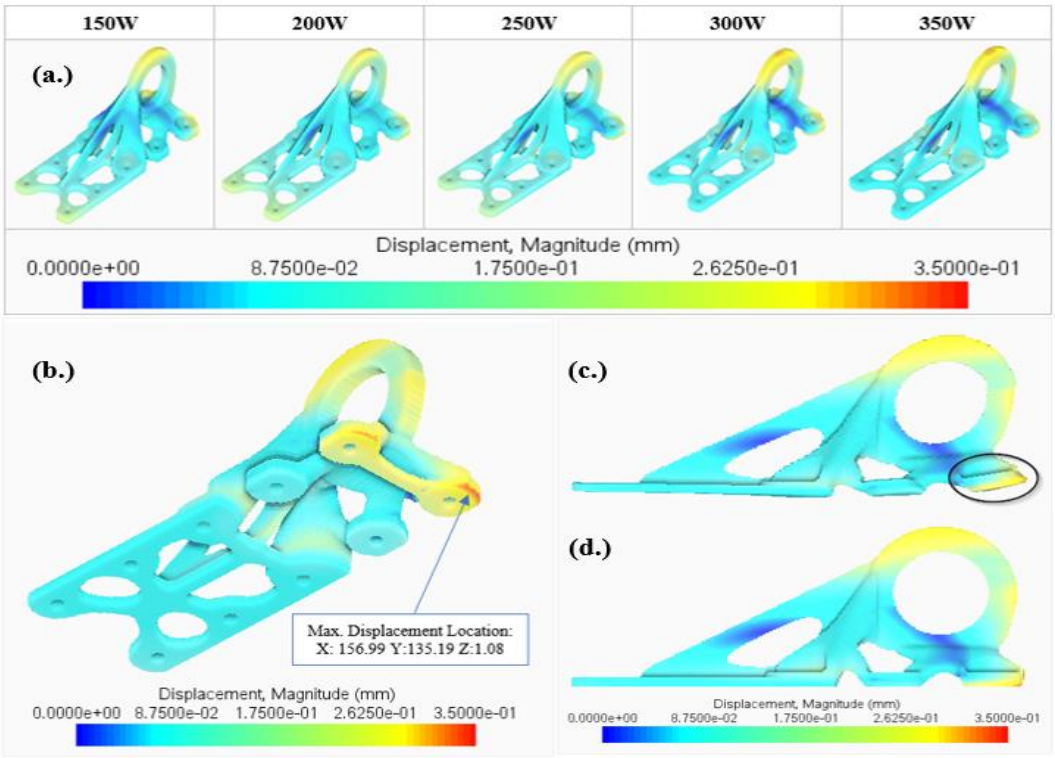

Figure 4.17. Simulation using varying Laser Power: a.) Displacement profile b.) Maximum displacement location c.) Part warpage d.) Displacement compensated part.

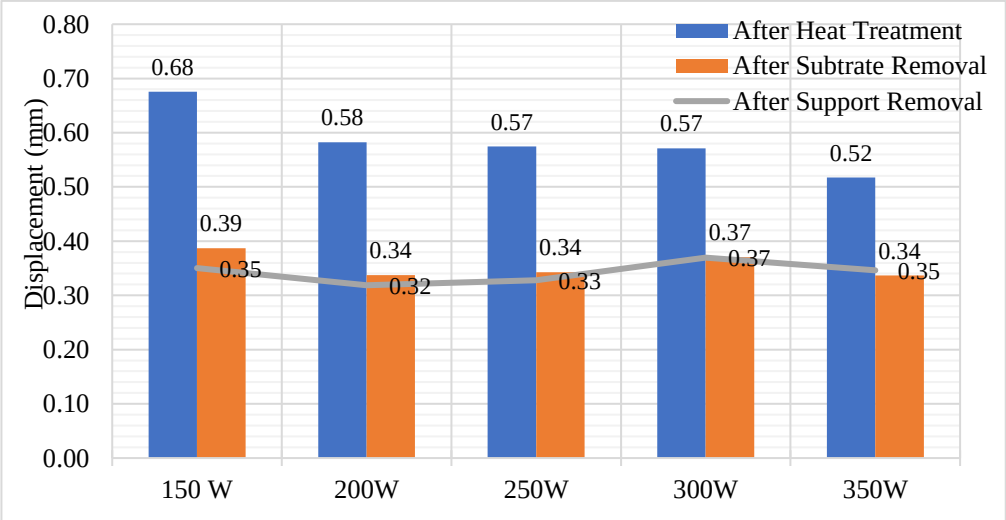

Figure 4.18. Maximum displacement magnitudes after heat treatment, substrate removal and support removal for the entire build.

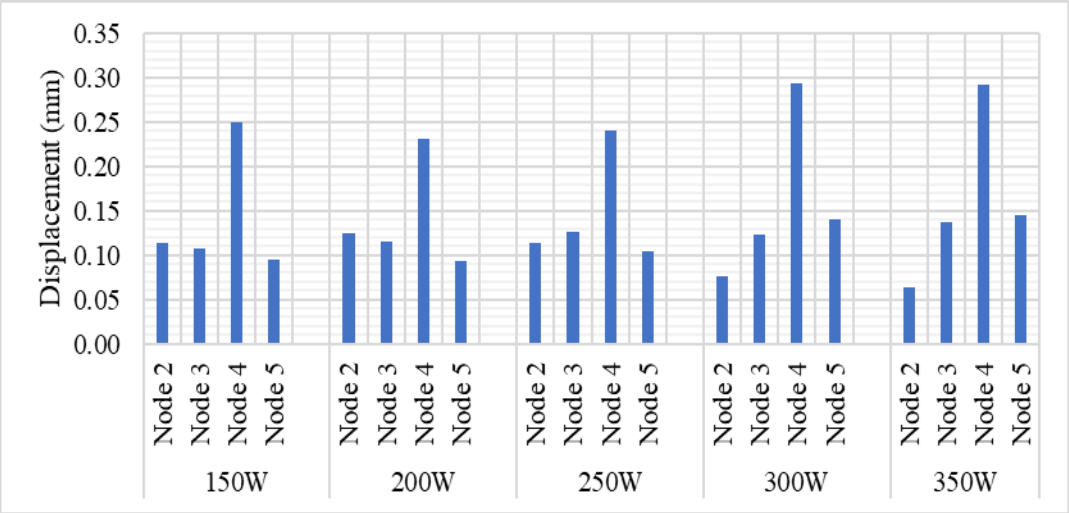

Figure 4.19. Displacement magnitudes after support removal at the 5 nodes.

4.2.4. Stress Results

At 800°C, the residual stresses after support removal declined to a significant extent compared to those before heat treatment and substrate removal as expected. However, the increments in the laser power did not seem to produce any major changes in the Cauchy and von Mises stress magnitudes as shown in Figure 4.20.

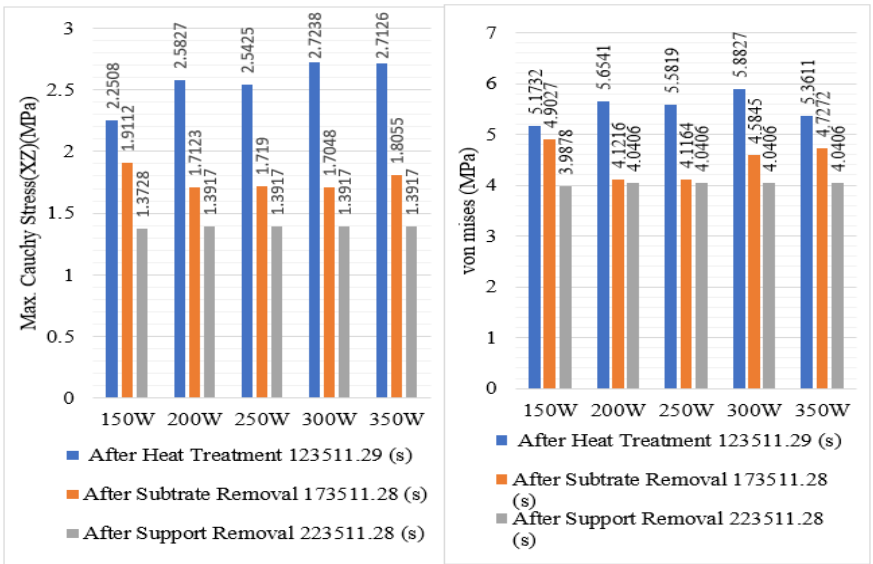

Figure 4.20. Maximum Cauchy Stress in the XZ axis and von Mises stress in the last three production stages.

4.3. Effect of Increasing Scan Speed

Due to the different build completion times that arose from the different scan speeds, the node points in Table 3.8 were investigated after the build heights of 3.24 mm, 11.88 mm and 28.08 mm respectively. The times at which each build simulation corresponded to the three build heights is indicated in Table 4.3.

Table 4.3. Times at which simulations were at build heights of 3.24 mm,11.88 mm and 28.08 mm

Build Height	600mm/s	800mm/s	1000mm/s	1200mm/s
3.24 mm	2676	2529	2253	2148
11.88mm	7981	7658	7165	6961
28.08mm	16596	16175	15574	15318

4.3.1. Thermal Gradients and Temperature History

After a build height of 3.24 mm, the highest temperature and thermal gradients values originated from the use of lowest scan speed. The temperature obtained from the use of the 1200 mm/s scan speed was approximately 200°C lower compared to that at 600 mm/s.

Similarly, the thermal gradients were much lower as indicated in Figure 4.21. The parts on node 4 and 5 were later built at a build height of 19.44 mm and 28.08 mm respectively and hence did not have any values at the time when the build height was at 3.24 mm. In terms of the temperature and thermal gradient history across the four scan speeds at build heights of 11.88 mm and 28.08 mm, the same trend is observed similar to that detected after completion of a build height of 3.24 mm despite their decline in magnitude when compared to those at a lower build height (see Figure 4.22 and Figure 4.23.) The simulated heat treatment was done after 123888 s, 123248 s, 122865 s and 122609 s for the 600 mm/s, 800 mm/s, 1000 mm/s and 1200 mm/s scan speeds respectively. At this stage, the temperatures ranged from 762.2°C to 767.2°C and the thermal gradients were all evened out to near equal values of all the four scan speeds as shown in Figure 4.24

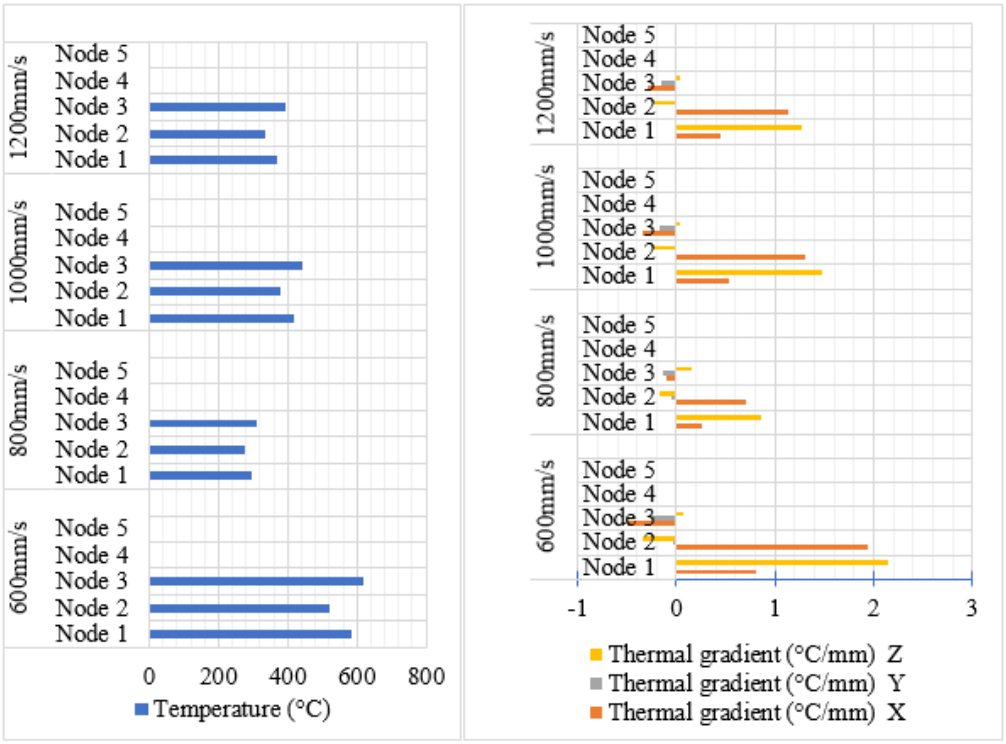

Figure 4.21. Predicted temperatures and thermal gradients at a build height of 3.24 mm.

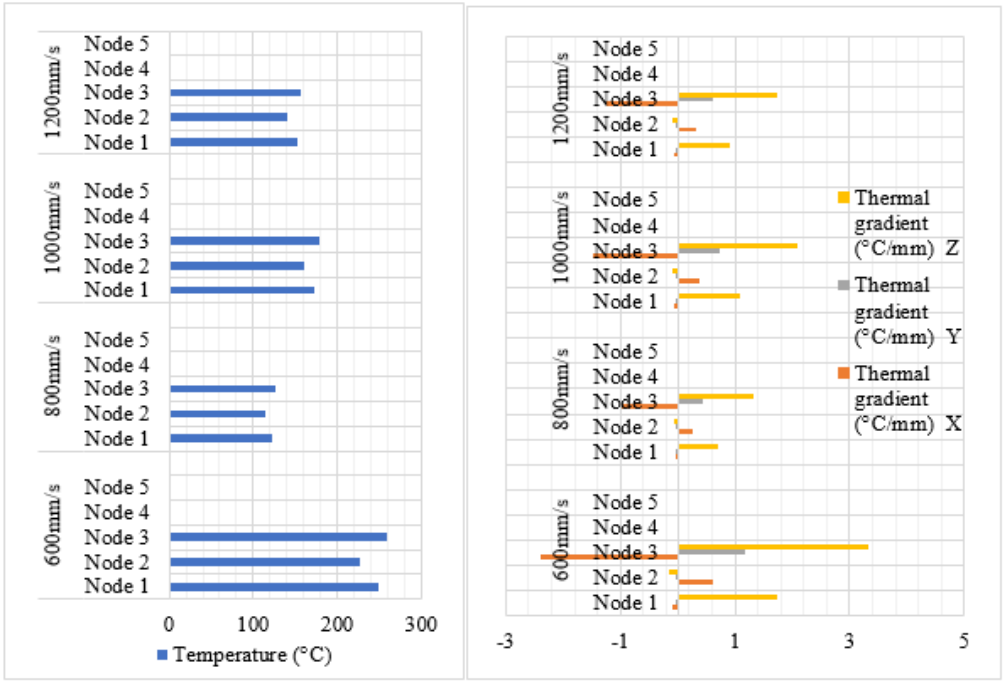

Figure 4.22. Predicted temperatures and thermal gradients at a build height of 11.88 mm.

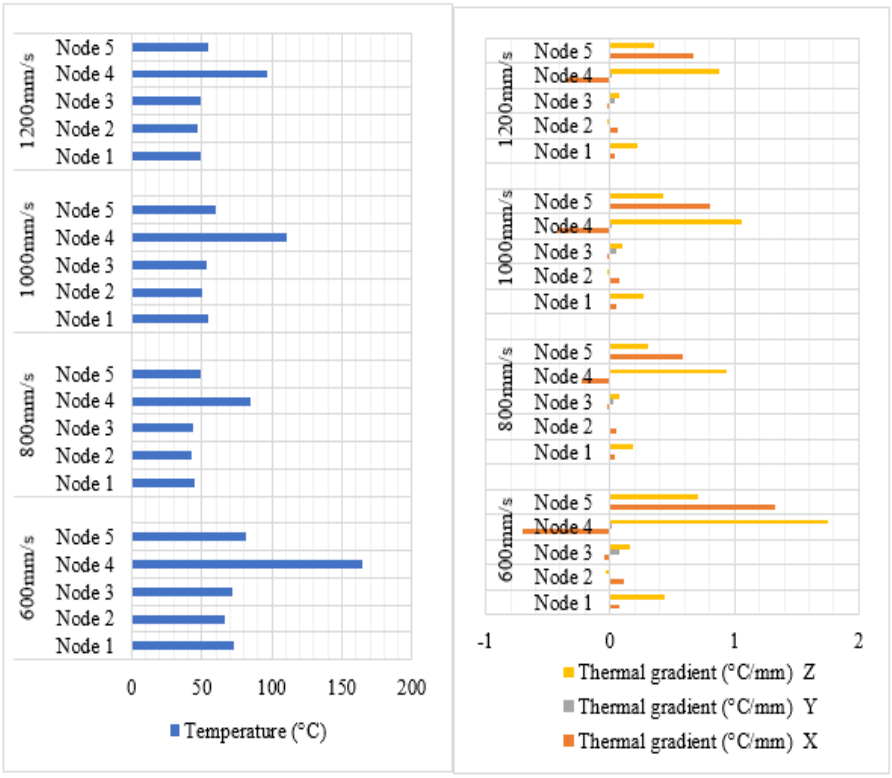

Figure 4.23. Predicted temperatures and thermal gradients at a build height of 28.08mm

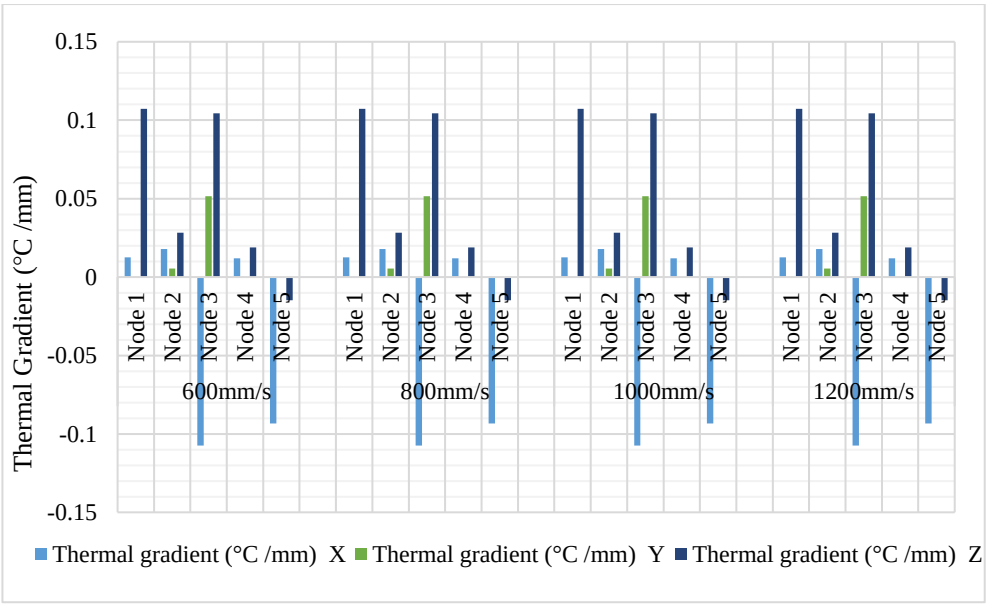

Figure 4.24. Thermal gradients after heat treatment for varying scan speeds.

4.3.2. Interlayer Temperatures

The interlayer temperatures after the simulated heat treatment process nodes declined with increasing scan speeds (Figure 4.25). This phenomenon could be attributed to the higher exposure times of moving laser for the simulations using lower scan speeds.

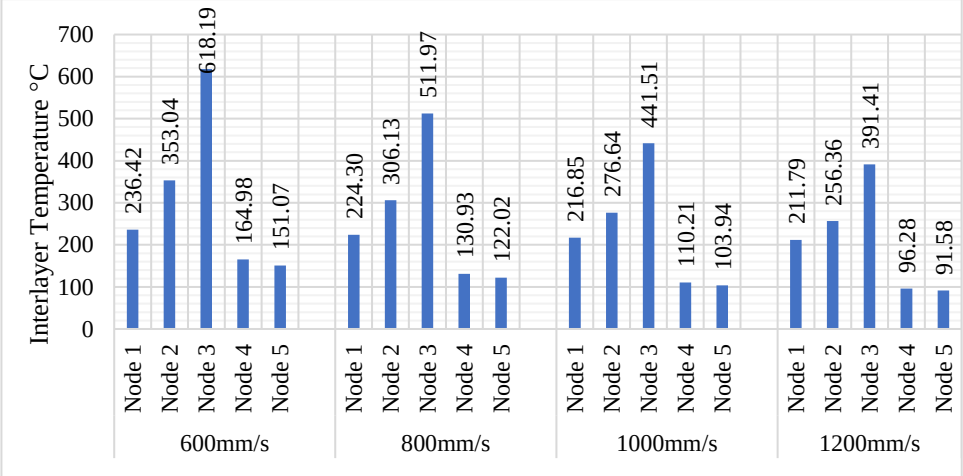

Figure 4.25. Interlayer temperatures after the simulated heat treatment.

4.3.3. Displacement Results

Displacement magnitudes observed immediately after heat treatment using the 1200mm/s and 1000mm/s scan speeds were slightly higher than those obtained from the 600mm/s and 800mm/s scan speeds. (Figure 4.26). However, the subsequent stages of substrate and support removal did not yield any significant changes in the distortion, even in the x and z axis that previously had slightly higher displacement magnitudes. (Figure 4.27)

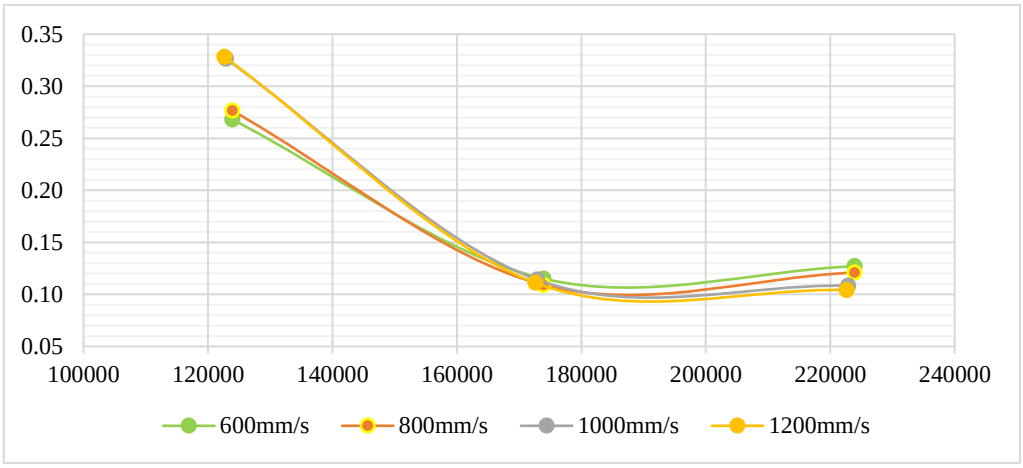

Figure 4.26. Displacement magnitudes at node 5 immediately after the heat treatment process.

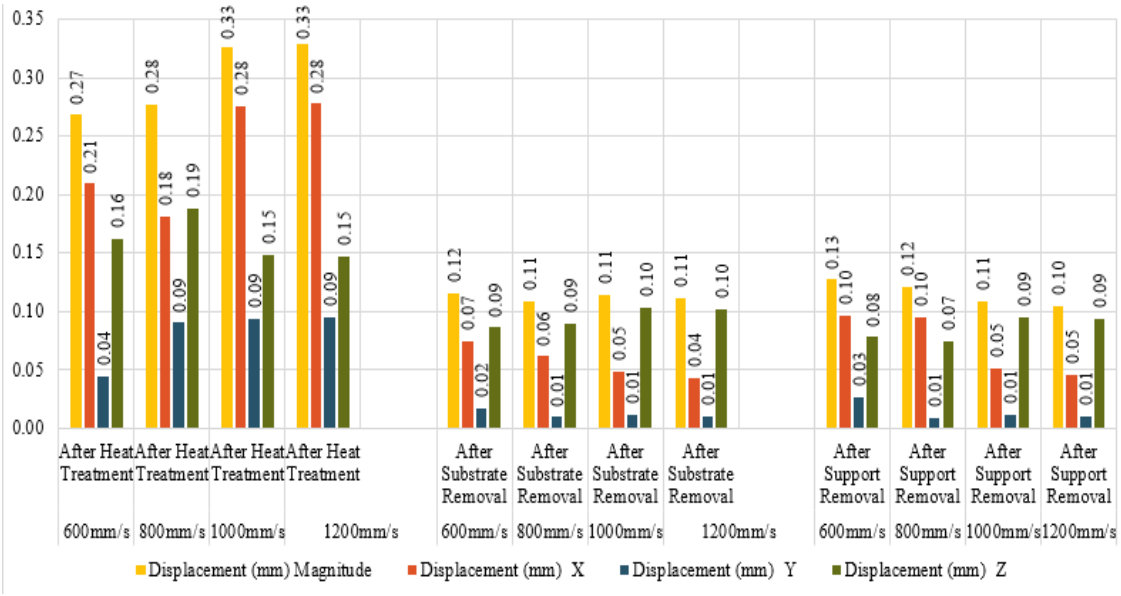

Figure 4.27. Displacements in the x, y and z axis after simulated heat treatment, build plate and support removal at node 5.

4.3.4. Stress Results

As with the displacement magnitudes at node 5, the predicted maximum principal stresses, von Mises and Cauchy stresses were higher with the use of 1200 mm/s and 1000 mm/s scan speeds compared to the much lower scan speeds of 600 mm/s and 800 mm/s. However, no significant differences were found between the 1200 mm/s and 1000 mm/s scan speeds and between 600 mm/s and 800 mm/s.

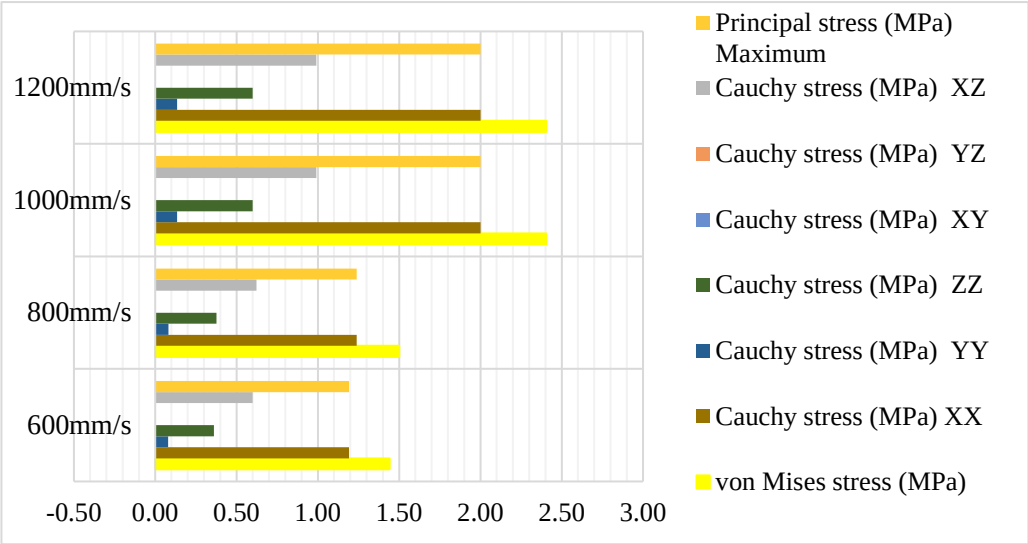

Figure 4.28. The maximum principal stresses and Cauchy stresses at different scan speeds at node 5.

4.4. Effect of Increasing Layer Thickness

Due to difference in layer thicknesses, the various SLM processes such as plasticity, heat treatment, substrate removal and support removal occurred at different times for each simulation. Simulation utility for Netfabb determined that heat treatment for the 0.03mm, 0.04mm, 0.05mm and 0.06mm was completed after 124275s, 119832s, 117318s and 115550s respectively.

Initial results obtained from the use of 0.03 mm, 0.04 mm, 0.05 mm and 0.06 mm layer thicknesses and process parameters in Table 3.6 indicated that 53, 40, 32- and 27-layer groups respectively.

The decrease in layer groups was attributed to the decreasing number of elements and nodes that consequently resulted to the decrease in simulation times and consumed computational power as listed in Table 4.4. Support removal was automatically done after 224,275 s, 219,382 s, 217,318 s and 215,550 s for the 30 µm, 40 µm, 50 µm and 60 µm layer thicknesses respectively.

Table 4.4. Properties of the different layer thicknesses.

Layer Thickness	0.03mm	0.04mm	0.05mm	0.06mm
Number of Layer Groups	53	40	32	27
Number of Nodes	237,838	130,596	66,891	65,775
Number of Elements	143,831	77,877	39,433	39,545
Peak RAM (GB) used for Thermal Simulation	1.81	0.91	0.53	0.52
Peak RAM (GB) used for Mechanical Simulation	6.34	3.44	1.77	1.76
CPU Wall Time for Thermal Simulation	1856s	776	358	321
CPU Wall Time for Mechanical Simulation	4317s	1570	625	567

4.4.1. Thermal Gradients and Temperature History

After heat treatment, the maximum thermal gradients and temperatures for the entire simulated build parts were as indicated in Table 4.5 below. A maximum temperature of 738°C for the all the layer thickness simulations was located at the same node point as shown by the arrow in Figure 4.30. The thermal gradients after the heat treatment process are shown in Table 4.5.

Table 4.5. Maximum Thermal Gradient and Maximum Temperatures from the varying layer thickness sizes.

Layer Thickness	0.03mm	0.04mm	0.05mm	0.06mm
Maximum Thermal Gradient (°C/mm)	1.87	1.47	1.02	0.09
Maximum Temperature (°C)	738.68	738.91	738.51	738.65

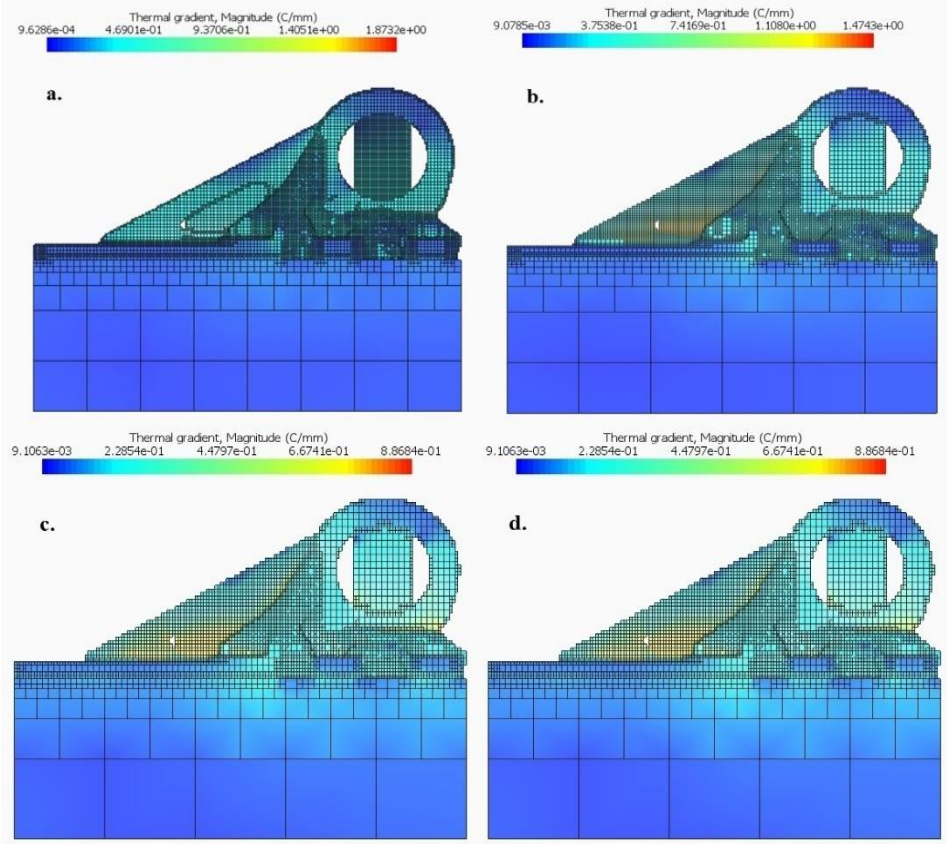

Figure 4.29. Thermal gradients after heat treatment using layer thicknesses of: a.) 0.03mm, b.) 0.04mm, c.) 0.05mm and d.) 0.06mm.

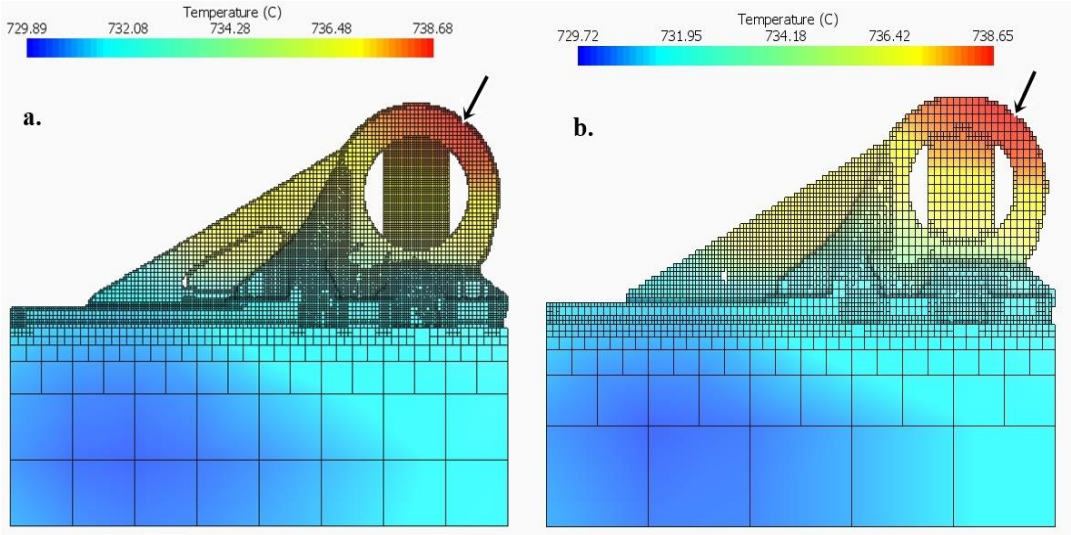

Figure 4.30. Temperature distribution after heat treatment using layer thicknesses of: a.) 0.03mm, b.) 0.06mm.

Due to the simulated heat treatment operations, the thermal gradients on the z axis at the nodal points in Figure 3.14 did not present any significant differences upon increments in the layer thickness as indicated in Figure 4.31.

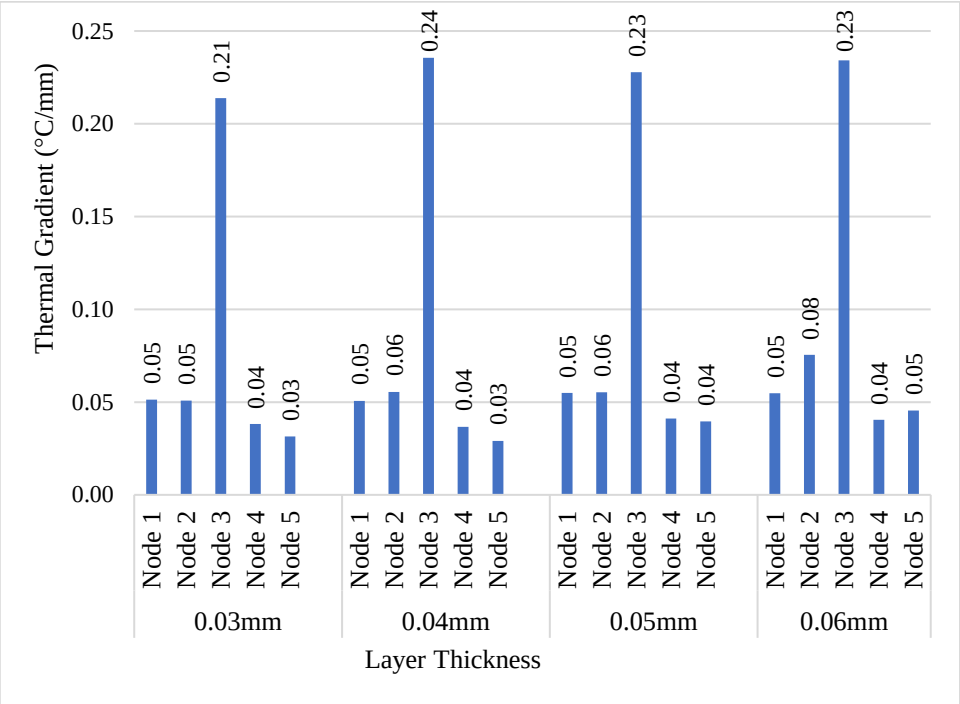

Figure 4.31. Thermal gradients on the z axis for all the 5 nodes.

4.4.2. Interlayer Temperatures

Nodes 2 and 3 experienced higher interlayer temperatures than the other nodes as they were much closer to the substrate and subject to its preheating effect. Interlayer temperatures from node 1 were not incorporated in the results because it was located on the support structure (see Figure 3.14). The highest interlayer temperatures for the entire simulations as observed at node 2 and 3 were realized with use of the 0.06mm layer thickness as indicated in Figure 4.32.

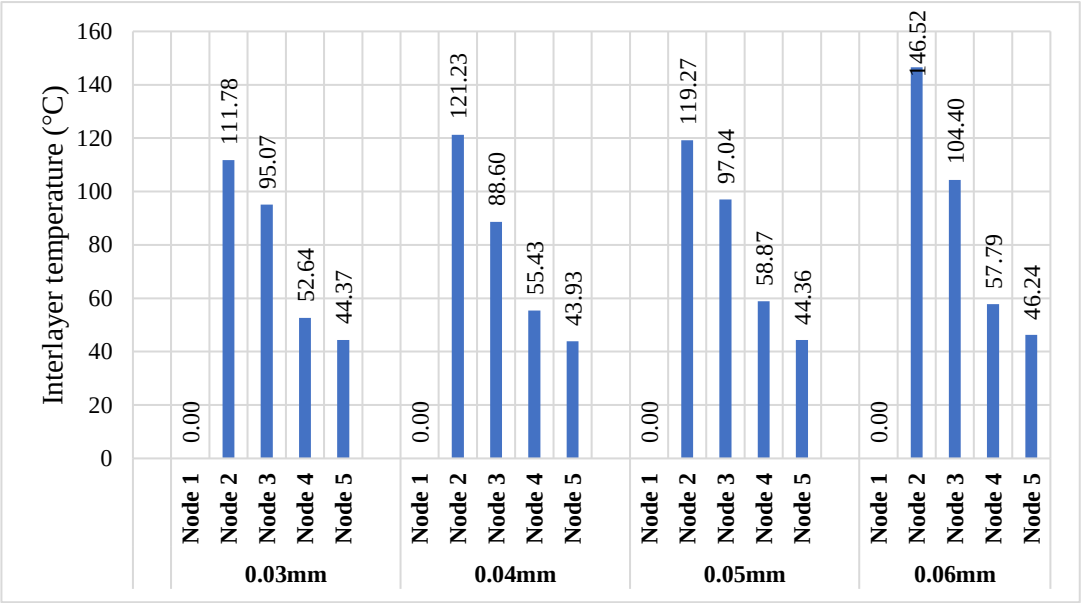

Figure 4.32. Interlayer temperatures for the 5 nodes using varying layer thicknesses after heat treatment.

4.4.3. Lack of Fusion and Hot Spots

At temperatures below 1300°C, lack of fusion (LOF) defects increased significantly with increments of layer thickness. At temperatures below 1600°C, an increase in predicted LOF was also observed to occur with increasing layer thickness at all the nodes. (see Figure 4.33.)

On the same note, it was also observed that the predicted LOF volume percentages were greater than 70% at temperatures below 1600°C, but less than 12% at temperatures below 1300°C. From a practical perspective, this clearly indicated that an undesired amount of LOF defects were likely to render the part to be produced by SLM defective if a layer thickness greater than 0.03mm was used between 1300°C - 1600°C.

Contrary to the above results, at temperatures above 2000°C, an overall decrease in the hot spot volume percentage occurred only at node 3 after an increment of layer thickness from 0.04 mm - 0.06 mm.

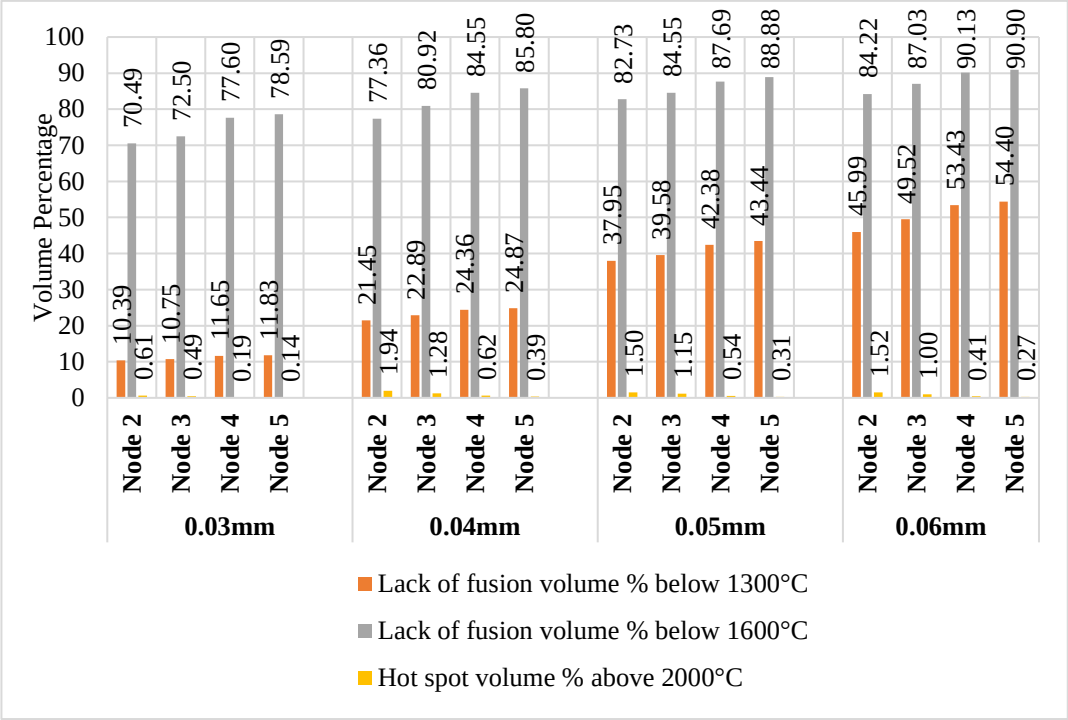

Figure 4.33. Predicted lack of fusion and hot spot volume for varying layer thicknesses after simulated heat treatment.

4.4.4. Displacement Results

The maximum predicted displacements of the entire part after support and substrate removal were 0.35 mm, 0.41 mm, 0.15 mm and 0.48 mm obtained from the use of 0.03mm, 0.04mm, 0.05mm and 0.06mm layer thicknesses respectively. The observed displacement profile for all the simulations is shown in Figure 4.34.

Further investigation of the 0.06mm layer thickness simulation indicated an upward warpage at the front part of the geometry after its distorted STL part was magnified by scale factor of 5 and compared to that of the original undistorted part (see Figure 4.35). In general, no direct correlation between the magnitude of displacement at the nodes and with the increasing layer thicknesses after support removal (see Figure 4.36). However, upon comparison to the other layer thicknesses, the highest displacements were observed at node 4 and 5 using a layer thickness of 0.06mm.

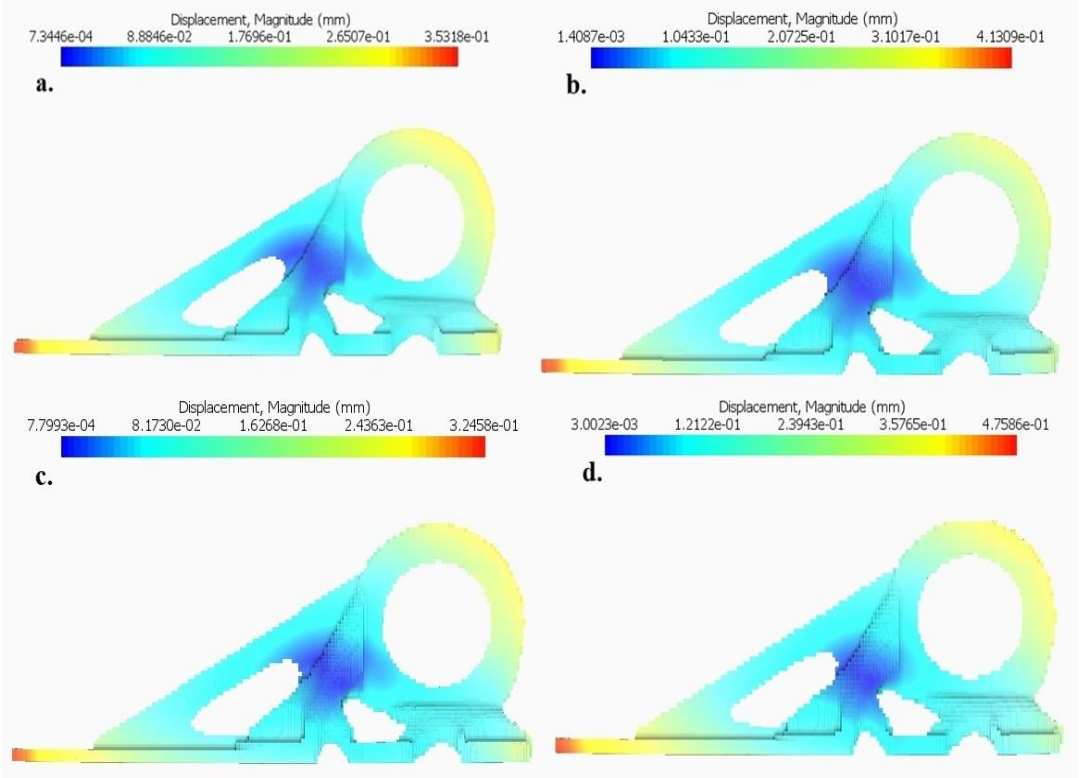

Figure 4.34. Displacement Magnitudes using layer thicknesses of: a.) 0.04mm, b.) 0.05mm and c.) 0.06mm and d.) 0.06mm.

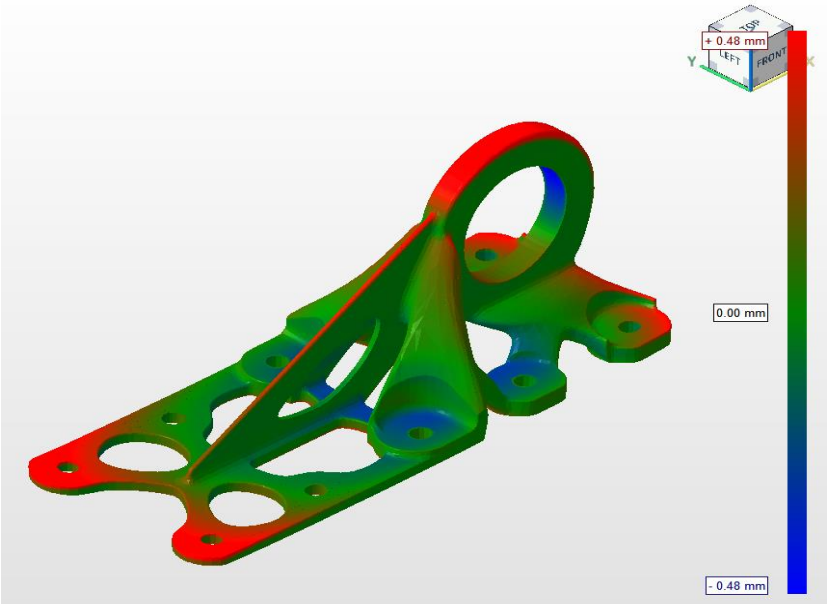

Figure 4.35. Mesh comparison to show distortion after warp magnification of 5 after using a layer thickness of 0.06 mm.

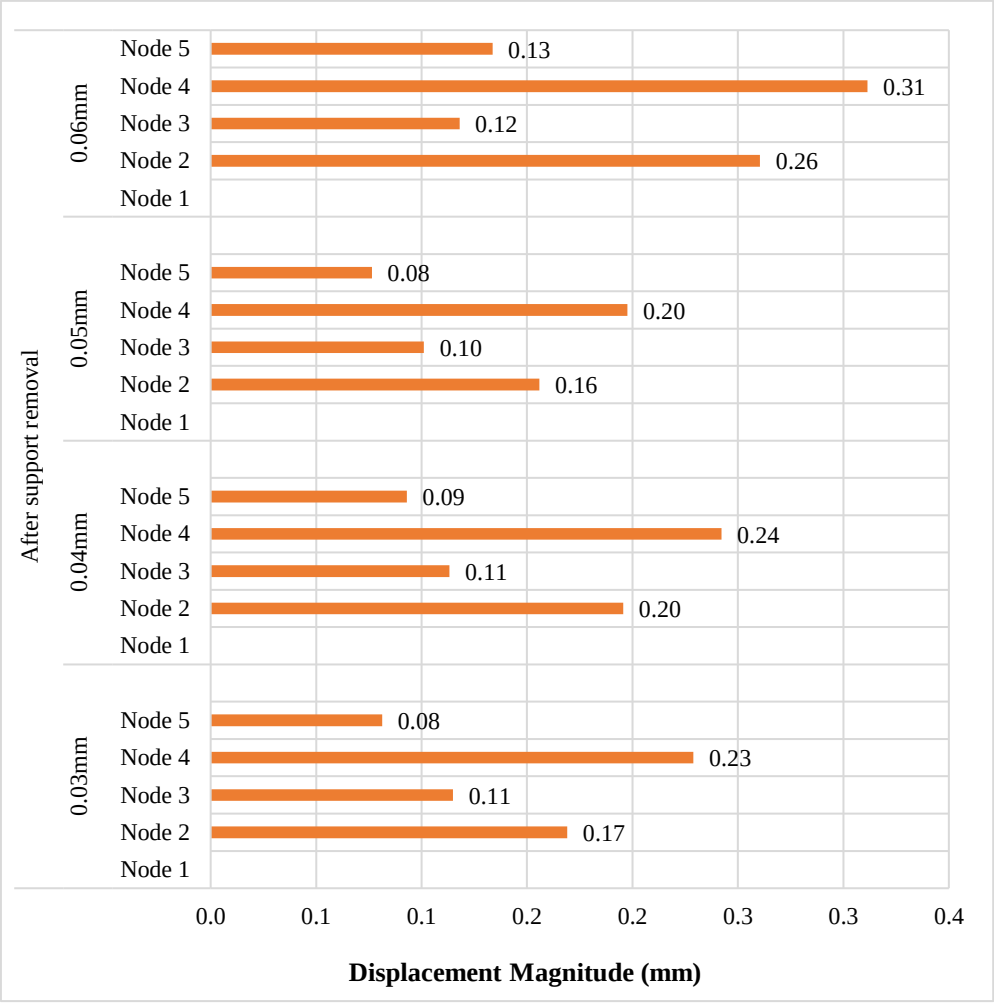

Figure 4.36. Displacement magnitudes after support removal at the node points using varying layer thicknesses.

4.4.5. Stress Results

At the nodes, the von Mises and the principle stresses largely varied with increments of layer thickness and some extent depending on the part geometry. At node 2 and 3, a decrease in the von mises and principle stress occurred after subsequent layer thickness increments. Contrary to these results and with an exception of the stress results observed using a layer thickness of 0.05 mm, node 5 experienced a decrease of the von Mises and the principle stresses with a decrease of layer thickness as shown in Figure 4.37.

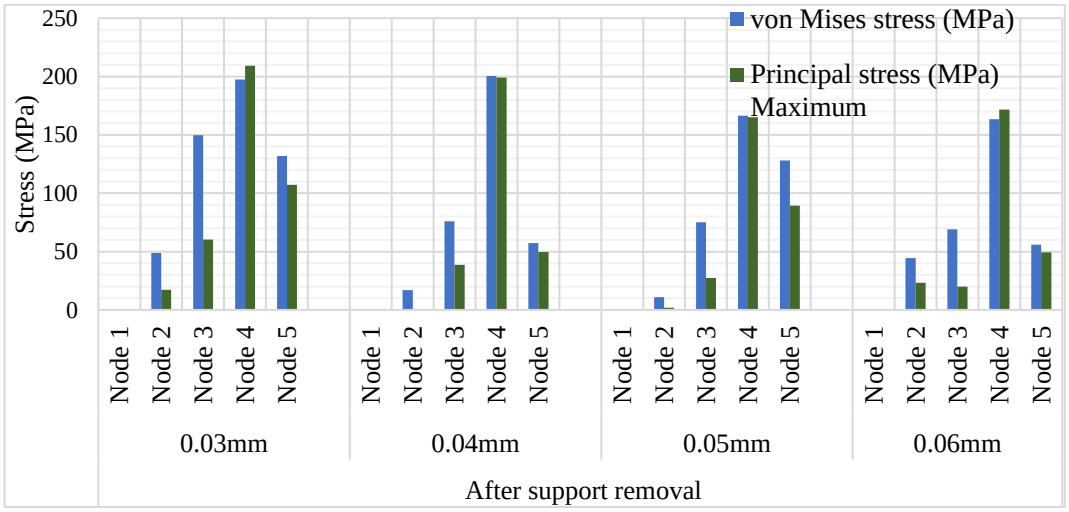

Figure 4.37. The von Mises and maximum principle stress magnitudes in the XZ axis after support removal for varying layer thicknesses.

4.5. Preheating Effect

After 2529 s, which was considered as an early build stage as the build height was 7.02 mm, higher thermal gradients in the z axis in the built plate preheated at 450°C were observed as indicated in Figure 4.38. However, after 12425 s (late build stage), when the build height was at 19.44 mm, the temperatures and thermal gradients decreased significantly (see Figure 4.39) possibly due to the increased height from the build plate.

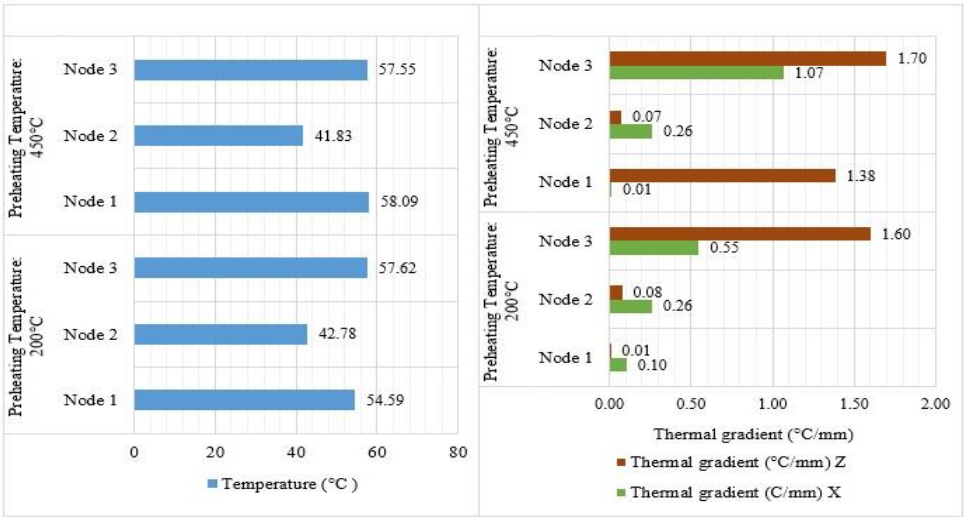

Figure 4.38. Temperature and thermal gradients from build plates preheated at 200°C and 450°C after 2529 s

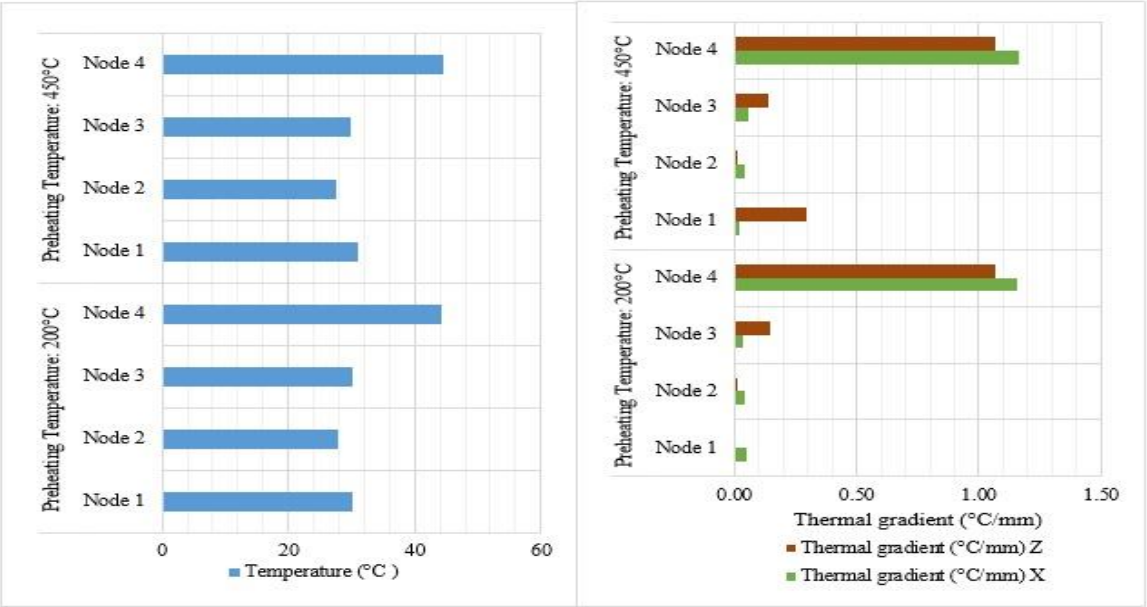

Figure 4.39. Temperature and thermal gradients from build plates preheated at 200°C and 450°C after 12425 s.

After support removal, the displacement magnitudes were much higher at the 450°C preheated built plate than those experienced using a preheating temperature of 200°C (see Figure 4.40). This phenomenon could be attributed to the higher residual stresses induced from using a higher preheating temperature as the von Mises stresses magnitudes obtained from using a preheating temperature of 450°C were higher than those acquired from using a preheating temperature of 200°C (see Figure 4.41).

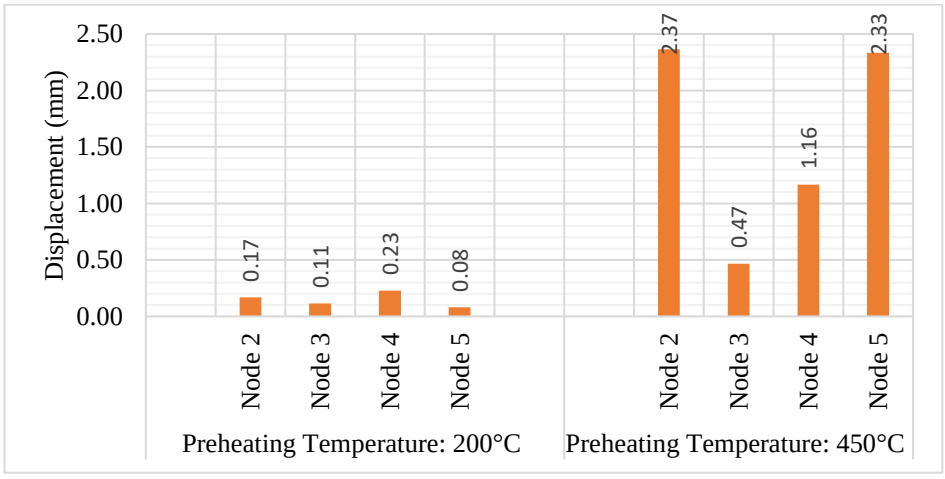

Figure 4.40. Displacement magnitudes after support removal from the build plates preheated at 200°C and 450°C.

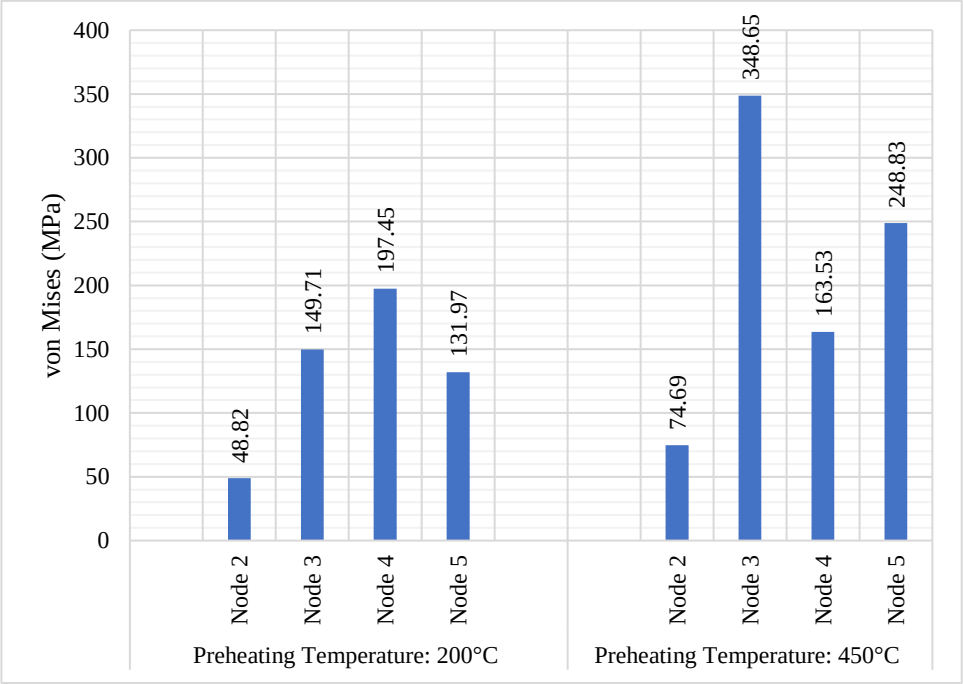

Figure 4.41. The von Mises stress magnitudes after support removal from build plates preheated at 200°C and 450°C.

4.6. Effect of Increasing Build Plate Thickness

After 5354 s, when the built height was 7.02 mm, the temperatures at the nodes decreased with increasing build plate thickness as shown in Figure 4.42. The corresponding thermal gradients in the z-axis were found to increase with increasing built plate thickness (see Figure 4.42).

At a later build stage time of 12426 s, when the built height was 19.44 mm, the built plate thickness did not significantly influence the thermal gradients and temperatures (see Figure 4.43). This could be attributed to the possibility that built had more time to effectively allow more heat dissipation on the build part during the late build stages.

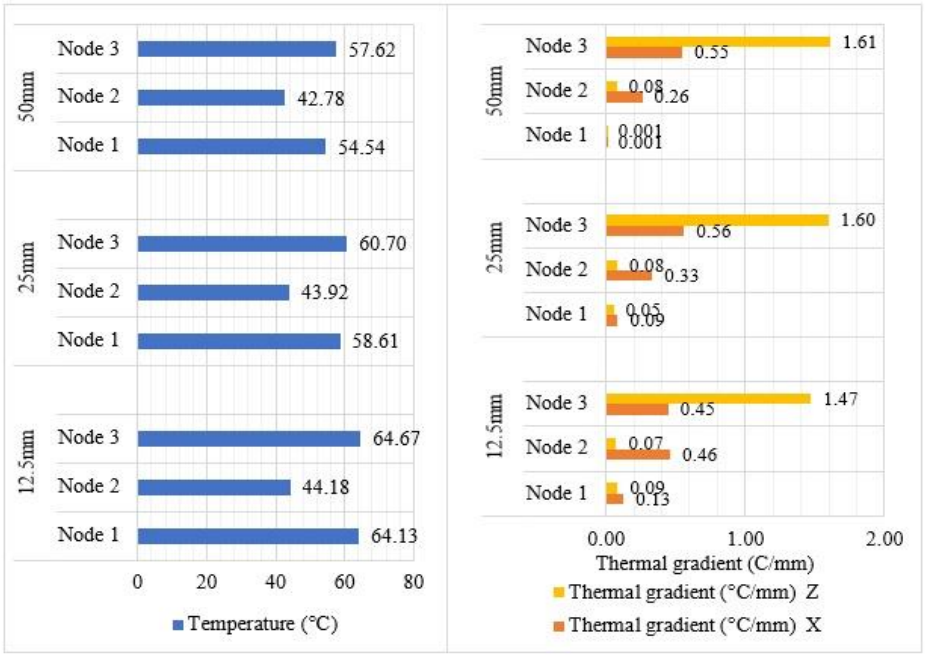

Figure 4.42. Temperature and thermal gradients from a 12.5 mm, 25 mm and 50 mm build plate on the nodes after 2529 s.

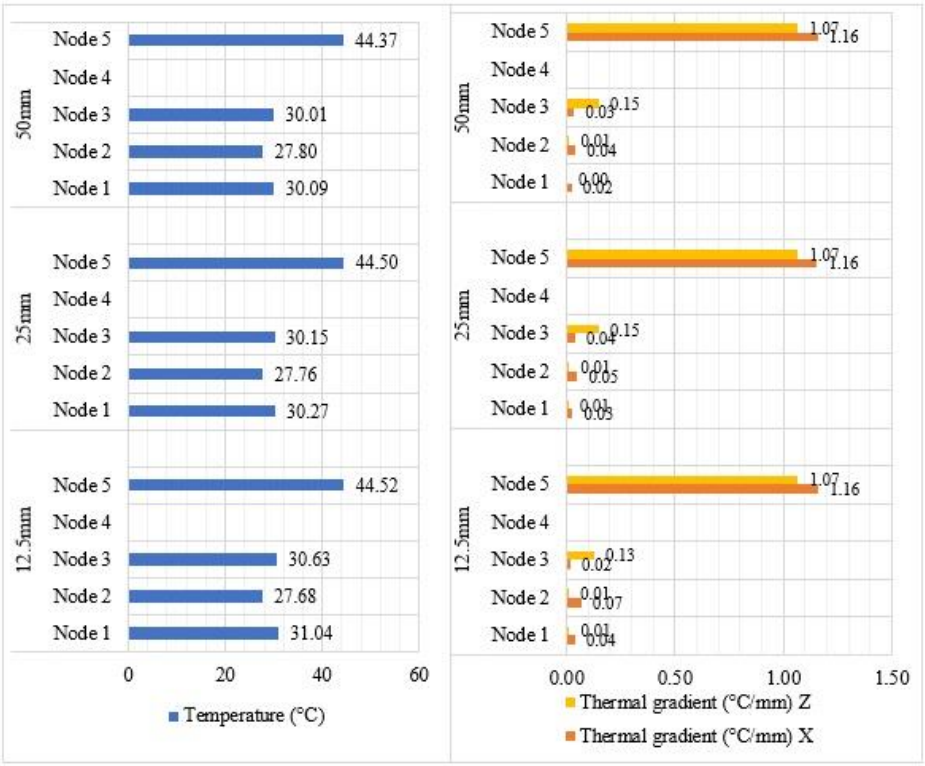

Figure 4.43. Temperature and thermal gradients from a 12.5 mm, 25 mm and 50 mm build plate on the nodes after 12426 s.

4.7. Recoater Blade Interference Results

The recoater clearance of 80% was generally upheld in all the layers of the simulations used in this study. This meant that at no stage of the build simulations processes did the upward deflection of a previously formed layer impinge on newly formed layer. On average the recoater clearance ranged between 90-100% (see Figure 4.44).

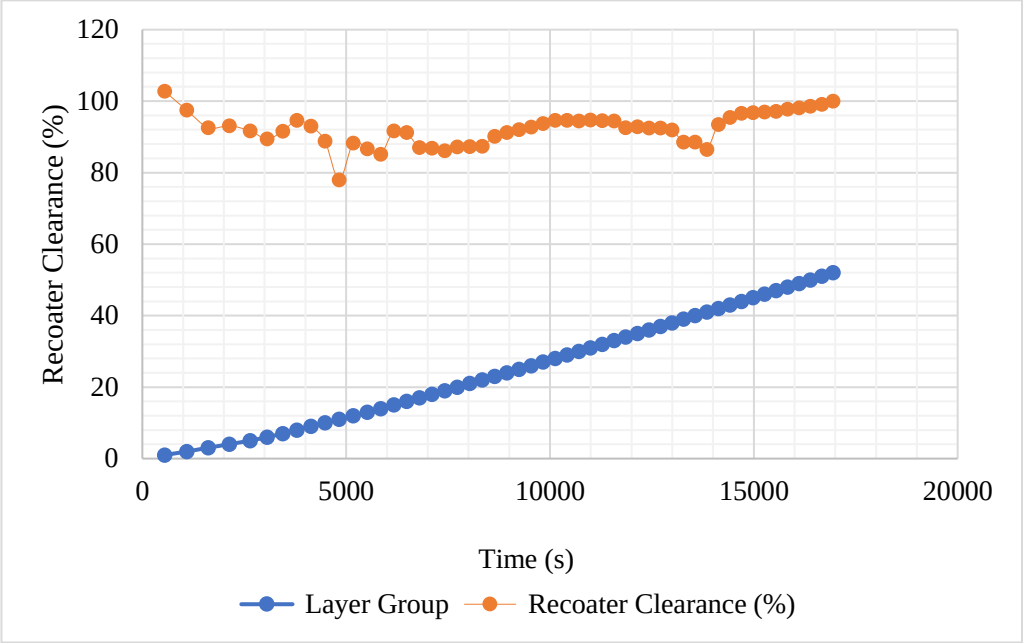

Figure 4.44. Recoater Clearance during the simulation process using a laser power of 150W and process parameters in Table 3.4.

5. CONCLUSION AND SUGGESTIONS

This study demonstrated the importance of using simulation tools before part printing to predict and analyse thermomechanical responses and defects that would otherwise occur or distort part geometry during laser powder bed fusion. Autodesk Netfabb Simulation Utility was used to simulate part build of a Ti6Al4V cabin bracket using varying process parameter magnitudes. The effect of increasing laser power, scan speed, layer thickness, preheating temperatures and build plate thickness were investigated to show the cause-and-effect relationship between them and the resultant thermal gradients, temperature distribution, displacements and residual stresses.

The main conclusions of this study as following:

The thermal gradients are highly influenced by the magnitude of the laser power (heat input). With an increase in laser power, a significant increase in both the thermal gradients and interlayer temperatures in the early simulation stages is observed. Higher thermal gradients in the z axis are observed as compared to the x axis. The difference in the displacement values was more likely to be influenced by the post processing operations rather than by the increase in laser power.

The highest temperature and thermal gradients values originated from the use of lowest scan speed during the initial build simulation stages. After heat treatment, the lower interlayer temperatures were experienced in the build having higher scan speeds. This phenomenon is attributed to the higher exposure times of moving laser using lower scan speeds.

Layer thickness sizes greatly influenced the complexity of the part's geometry mesh strategy and computational resources. The maximum thermal gradients for the entire part in the z direction decreased with increasing layer thickness and the higher interlayer temperatures were obtained using a 0.06 mm layer thickness as compared to that 0.03 mm. The von Mises and the principle stresses largely varied with increments of layer thickness and some to extent depending on the part geometry.

The thermal gradients in the z axis in the built plate preheated at 450°C were higher compared to those from a built plate preheated at 200°C. However, in the late build simulation stages, the difference in temperatures and thermal gradients decreased significantly possibly due to the increased distance from the build plate that allowed for more heat dissipation by conduction. To a considerable extent, decreasing the build plate thickness highly influenced the formation of higher thermal gradients especially during the early build simulation stages.

The maximum difference of 29.9% in the displacement magnitudes between the experimental (in situ) and simulation results was obtained. The magnitude for this error and the accuracy levels of this work, could be attributed to possibility that the simulation was done using a thermal boundary condition that used uniform heat loss as opposed to one that allowed conduction to loose powder. Due to the high number of simulations, it was experimentally feasible to validate all the maximum temperatures and thermal gradients. However, as evident in studies by Yılmaz & Kayacan, 2020, which incorporated a similar approach to that used in this work, a relatively high accuracy of 93% was observed.

The use of simulation tools such as Autodesk Netfabb is crucial as it enables prediction and mitigation of distortion, residual stress and lack of fusion defects associated with laser powder bed fusion. The advantages of reduced print part failures, time and cost savings can also be realized from the use of part build simulations in additive manufacturing processes.

REFERENCES

A Comprehensive List of all the Metal 3D Printer Manufacturers. (2018). https://www.3dnatives.com/en/. https://www.3dnatives.com/en/metal-3d-printer-manufacturers/

Abliz, D., Adamowski, J. C., Ahmad, A. H., Ahsan, M. M., Ahsan, Q., Akbar, S. A., Akhtar, S. S., Akter, T., Al-Ahmari, A., Al-Dweik, A. Y., Alam, M. M., Alaswad, A., Albano, L., Ali, N., Aliofkhazraei, M., Alves, M., Andrade, M. A. B., Antonini, J. M., Aqida, S. N., … Azouz, A. B. (2014). *Comprehensive Materials Processing* (H. Saleem, C. J. Van Tyne, G. F. Batalha, & B. Yilbas (Eds.); Issue 1st Edition). Elsevier Ltd. https://www.elsevier.com/books/comprehensive-materials processing/9780080965338

Aboulkhair, N. T., Everitt, N. M., Ashcroft, I., & Tuck, C. (2014). Reducing porosity in AlSi10Mg parts processed by selective laser melting. *Additive Manufacturing*. https://doi.org/10.1016/j.addma.2014.08.001

Aggarangsi, P., & Beuth, J. L. (2006). Localized preheating approaches for reducing residual stress in additive manufacturing. *Proc. SFF Symp., Austin*, 709–720. http://edge.rit.edu/content/P10551/public/SFF/SFF 2006 Proceedings/Manuscripts/61-Aggarangsi.pdf

Ali, H., Ghadbeigi, H., & Mumtaz, K. (2018). Residual stress development in selective laser-melted Ti6Al4V: a parametric thermal modelling approach. *International Journal of Advanced Manufacturing Technology*, *97*(5–8), 2621–2633. https://doi.org/10.1007/s00170-018-2104-9

Ali, H., Ma, L., Ghadbeigi, H., & Mumtaz, K. (2017). In-situ residual stress reduction, martensitic decomposition and mechanical properties enhancement through high temperature powder bed pre-heating of Selective Laser Melted Ti6Al4V. In *Materials Science and Engineering: A* (Vol. 695). https://doi.org/10.1016/j.msea.2017.04.033

REFERENCES (continued)

Antony, K., & Arivazhagan, N. (2015). Studies on energy penetration and marangoni effect during laser melting process. *Journal of Engineering Science and Technology*, *10*(4), 509–525.

Anwar, A., & Pham, Q. C. (2016). Selective laser melting of AlSi10Mg: Effects of scan direction, part placement and inert gas flow velocity on tensile strength. *Journal of Materials Processing Technology*, *240*. https://doi.org/10.1016/j.jmatprotec.2016.10.015

ASTM International. (2013). F2792-12a - Standard Terminology for Additive Manufacturing Technologies. In *Rapid Manufacturing Association*. https://doi.org/10.1520/F2792-12A.2

Attar, H., Calin, M., Zhang, L. C., Scudino, S., & Eckert, J. (2014). Manufacture by selective laser melting and mechanical behavior of commercially pure titanium. *Materials Science and Engineering A*, *593*, 170–177. https://doi.org/10.1016/j.msea.2013.11.038

Autodesk Help. (2020a). *Mesh Settings*. https://knowledge.autodesk.com/support/netfabb/learn-explore/caas/CloudHelp/cloudhelp/2019/ENU/NETF-Utility-Simulation/files/GUID-65A1C07C-4101-4D5E-812B-15B40CA48544-htm.html

Autodesk Help. (2020b). *Netfabb Simulation Theory*. https://knowledge.autodesk.com/support/netfabb/learn-explore/caas/CloudHelp/cloudhelp/2021/ENU/NETF-Utility-Simulation/files/GUID-6BAF550D-C179-4785-99AA-2355A3FCFC90-htm.html

REFERENCES (continued)

Autodesk Help. (2020c). *The Thermal Model*. https://knowledge.autodesk.com/support/netfabb/learnexplore/caas/CloudHelp/cloudhelp/2021/ENU/NETF-Utility-Simulation/files/GUID-39A3F054-8BB5-4A95-B0AD-6299F852840A-htm.html

Autodesk Help. (2020d). *The Weakly Coupled Model*. https://knowledge.autodesk.com/support/netfabb/learn-explore/caas/CloudHelp/cloudhelp/2021/ENU/NETF-Utility-Simulation/files/GUID-C40D11AE-4F88-4E6B-8205-C42569101FCA-htm.html

Autodesk Help. (2020e). *Tutorial 16: To Analyze Lack of Fusion and Hot Spots*. https://knowledge.autodesk.com/support/netfabb/learn-explore/caas/CloudHelp/cloudhelp/2020/ENU/NETF-Utility-Simulation/files/GUID-D3D423E3-BB0E-474B-AB8C-A871BC443E1D-htm.html

Azam, F. I., Abdul Rani, A. M., Altaf, K., Rao, T. V. V. L. N., & Zaharin, H. A. (2018). An In-Depth Review on Direct Additive Manufacturing of Metals. *IOP Conference Series: Materials Science and Engineering*, *328*(1). https://doi.org/10.1088/1757-899X/328/1/012005

Baauw, M., Hellemondt, G., van Hooff, M., & Spruit, M. (2015). The accuracy of positioning of a custom-made implant within a large acetabular defect at revision arthroplasty of the hip. *The Bone & Joint Journal*, *97-B*, 780–785. https://doi.org/10.1302/0301-620X.97B6.35129

Bauereiß, A., Scharowsky, T., & Körner, C. (2014). Defect generation and propagation mechanism during additive manufacturing by selective beam melting. *Journal of Materials Processing Tech.*, *214*(11), 2522–2528. https://doi.org/10.1016/j.jmatprotec.2014.05.002

REFERENCES (continued)

Bian, L., Shamsaei, N., & Usher, J. M. (2017). Laser-Based Additive Manufacturing of Metal Parts: Modeling, Optimization, and Control of Mechanical Properties. In L. Bian, N. Shamsaei, & J. M. Usher (Eds.), *Laser-Based Additive Manufacturing of Metal Parts: Modeling, Optimization, and Control of Mechanical Properties* (1st ed., Vol. 1, Issue 1). Boca Raton : CRC Press, Taylor & Francis. https://doi.org/10.1201/9781315151441

Borisov, E., Anatoliy, P., Sufiiarov, V., & Polozov, I. (2015). Microstructure and Mechanical Properties of Ti-6AL-4V Manufactured by SLM. *Key Engineering Materials*, *651–653*, 677–682. https://doi.org/10.4028/www.scientific.net/KEM.651-653.677

Boyer, R., & E.W, C. (1994). *Materials Properties Handbook: Titanium Alloys*. ASM International. https://www.asminternational.org/materials-resources/results/-/journal_content/56/10192/06005G/PUBLICATION#

Boyer, R. R. (2010). Titanium and Its Alloys: Metallurgy, Heat Treatment and Alloy Characteristics. In *Encyclopedia of Aerospace Engineering*. https://doi.org/10.1002/9780470686652.eae198

Brandt, M., Sun, S. J., Leary, M., Feih, S., Elambasseril, J., & Liu, Q. C. (2013). High-Value SLM Aerospace Components: From Design to Manufacture. *Advanced Materials Research*, *633*(January), 135–147. https://doi.org/10.4028/www.scientific.net/amr.633.135

Buchbinder, D., Meiners, W., Pirch, N., Wissenbach, K., & Schrage, J. (2014). Investigation on reducing distortion by preheating during manufacture of aluminum components using selective laser melting. *Journal of Laser Applications*, *26*(1), 012004. https://doi.org/10.2351/1.4828755

REFERENCES (continued)

Buls, S., Craeghs, T., Clijsters, S., Kempen, K., Swevers, J., & Kruth, J.-P. (2013). The influence of a dynamically optimized galvano based laser scanner on the total scan time of slm parts. *Solid Freeform Fabrication Symposium*, 260–266.

Cardarelli, F. (2001). Materials Handbook — a concise desktop reference. *Materials & Design*. https://doi.org/10.1016/s0261-3069(00)00075-3

Chen, Z., Xiang, Y., Wei, Z., Wei, P., Lu, B., Zhang, L., & Du, J. (2018). Thermal dynamic behavior during selective laser melting of K418 superalloy: numerical simulation and experimental verification. *Applied Physics A: Materials Science and Processing*, *124*(4), 1–16. https://doi.org/10.1007/s00339-018-1737-8

Chlebus, E., Kuźnicka, B., Kurzynowski, T., & Dybała, B. (2011). Microstructure and mechanical behaviour of Ti-6Al-7Nb alloy produced by selective laser melting. *Materials Characterization*. https://doi.org/10.1016/j.matchar.2011.03.006

Choo, H., Sham, K. L., Bohling, J., Ngo, A., Xiao, X., Ren, Y., Depond, P. J., Matthews, M. J., & Garlea, E. (2019). Effect of laser power on defect, texture, and microstructure of a laser powder bed fusion processed 316L stainless steel. *Materials and Design*. https://doi.org/10.1016/j.matdes.2018.12.006

Ciraud, P. A. (1972). Process and Device for the Manufacture of any Objects Desired from any Meltable Material. *FRG Disclosure Publication, 2263777*.

Costa, L., Vilar, R., Reti, T., & Deus, A. M. (2005). Rapid tooling by laser powder deposition: Process simulation using finite element analysis. *Acta Materialia*. https://doi.org/10.1016/j.actamat.2005.05.003

REFERENCES (continued)

Dai, D., & Gu, D. (2014). Thermal behavior and densification mechanism during selective laser melting of copper matrix composites : Simulation and experiments. *JOURNAL OF MATERIALS&DESIGN*, *55*, 482–491. https://doi.org/10.1016/j.matdes.2013.10.006

Deng, D. (2018). *Additively Manufactured Inconel 718 : Microstructures and Mechanical Properties*. https://doi.org/10.3384/lic.diva-144491

Denlinger, E. R., Gouge, M., Irwin, J., & Michaleris, P. (2017). Thermomechanical model development and in situ experimental validation of the Laser Powder-Bed Fusion process. *Additive Manufacturing*. https://doi.org/10.1016/j.addma.2017.05.001

Denlinger, E. R., Irwin, J., & Michaleris, P. (2014). Thermomechanical modeling of additive manufacturing large parts. *Journal of Manufacturing Science and Engineering, Transactions of the ASME*. https://doi.org/10.1115/1.4028669

Denlinger, E. R., Jagdale, V., Srinivasan, G. V., El-Wardany, T., & Michaleris, P. (2016). Thermal modeling of Inconel 718 processed with powder bed fusion and experimental validation using in situ measurements. *Additive Manufacturing*. https://doi.org/10.1016/j.addma.2016.03.003

Do, D. K., & Li, P. (2016). The effect of laser energy input on the microstructure, physical and mechanical properties of Ti-6Al-4V alloys by selective laser melting. *Virtual and Physical Prototyping*. https://doi.org/10.1080/17452759.2016.1142215

Donachie, M. J. (2000). Titanium: A Technical Guide. In *Titanium: A Technical Guide* (2nd ed.). ASM International. https://www.asminternational.org/search/-/journal_content/56/10192/06112G/PUBLICATION

REFERENCES (continued)

Dunbar, A. J. (2016). Analysis of the laser powder bed fusion additive manufacturing process through experimental measurement and finite element modeling. *Department of Mechanical Engineering*.

Elias, C. N., Fernandes, D. J., Galiza, J. A., dos Santos Monteiro, E., & de Almeida, A. C. C. (2018). Dental application. In *Nanocrystalline Titanium*. https://doi.org/10.1016/B978-0-12-814599-9.00012-2

EOS GmbH. (n.d.). *Titanium for industrial 3D printing | EOS GmbH*. https://www.eos.info/en/additive-manufacturing/3d-printing-metal/dmls-metal-materials/titanium-ti64-ticp

EOS Industrial 3D printing - Process, method and benefits. (n.d.). Retrieved May 11, 2019, from https://www.eos.info/additive_manufacturing/for_technology_interested

Flint, T., Yates, J., & Francis, J. (2013, August 18). Analytical solutions of the transient thermal field induced in finite bodies with insulating and convective boundary conditions subjected to a welding heat source. *International Association for Structural Mechanics in Reactor Technology (IASMIRT)*. https://doi.org/10.13140/2.1.2710.3680

Ford, S., & Despeisse, M. (2016). Additive manufacturing and sustainability: an exploratory study of the advantages and challenges. *Journal of Cleaner Production*, *137*, 1573–1587. https://doi.org/10.1016/j.jclepro.2016.04.150

Fu, C., & Guo, Y. B. (2014). *3-Dimensional Finite Element Modeling of Selective Laser Melting Ti-6Al-4V Alloy*.

REFERENCES (continued)

Goldak, J., Chakravarti, A., & Bibby, M. (1984). A new finite element model for welding heat sources. *Metallurgical Transactions B*. https://doi.org/10.1007/BF02667333

Gong, H., Rafi, H., Gu, H., Starr, T., & Stucker, B. (2014). Analysis of Defect Generation in Ti-6Al-4 V Parts Made using Powder Bed Fusion Additive Manufacturing Processes. In *Additive Manufacturing* (Vols. 1–4). https://doi.org/10.1016/j.addma.2014.08.002

Gorsse, S., Hutchinson, C., Gouné, M., & Banerjee, R. (2017). Additive manufacturing of metals: a brief review of the characteristic microstructures and properties of steels, Ti-6Al-4V and high-entropy alloys. *Science and Technology of Advanced Materials*, *18*(1), 584–610. https://doi.org/10.1080/14686996.2017.1361305

Gouge, M., & Michaleris, P. (2017). Thermo-mechanical modeling of additive manufacturing. In *Thermo-Mechanical Modeling of Additive Manufacturing* (First edit). Elsevier Inc. https://doi.org/10.1016/c2016-0-00317-0

Gu, D, Meiners, W., Wissenbach, K., & Poprawe, R. (2012). Laser additive manufacturing of metallic components: Materials, processes and mechanisms. *International Materials Reviews*, *57*, 133–164. https://doi.org/10.1179/1743280411Y.0000000014

Gu, Dongdong, Hagedorn, Y.-C., Meiners, W., Meng, G., Batista, R., Wissenbach, K., & Poprawe, R. (2012). Densification behavior, microstructure evolution, and wear performance of selective laser melting processed commercially pure titanium. *Acta Materialia*, *60*, 3849–3860. https://doi.org/10.1016/j.actamat.2012.04.006

Han, Q., Geng, Y., Setchi, R., Lacan, F., Gu, D., & Evans, S. L. (2017). Macro and nanoscale wear behaviour of Al-Al 2 O 3 nanocomposites fabricated by selective laser melting. *Composites Part B*, *127*, 26–35. https://doi.org/10.1016/j.compositesb.2017.06.026

REFERENCES (continued)

Hanzl, P., Zetkova, I., & Dana, M. (2017). *A Comparison of Lattice Structures in Metal Additive Manufacturing*. 0481–0485. https://doi.org/10.2507/28th.daaam.proceedings.067

Harris, I. D. (2011). Development and Implementation of Metals Additive Manufacturing Current Landscape in Additive Manufacturing. *DOT International, New Orleans*.

Herzog, D., Seyda, V., Wycisk, E., & Emmelmann, C. (2016). Additive manufacturing of metals. *Acta Materialia*, *117*, 371–392. https://doi.org/10.1016/j.actamat.2016.07.019

Huang, S. H., Liu, P., Mokasdar, A., & Hou, L. (2013). Additive manufacturing and its societal impact: A literature review. In *International Journal of Advanced Manufacturing Technology*. https://doi.org/10.1007/s00170-012-4558-5

Hussein, A., Hao, L., Yan, C., & Everson, R. (2013). Finite element simulation of the temperature and stress fields in single layers built without-support in selective laser melting. *Materials and Design*. https://doi.org/10.1016/j.matdes.2013.05.070

Inagaki, I., Takechi, T., Shirai, Y., & Ariyasu, N. (2014). Application and features of titanium for the aerospace industry. *Nippon Steel and Sumitomo Metal Technical*.

Jiang, W., Dalgarno, K. W., & Childs, T. H. C. (2002). Finite Element Analysis of Residual Stresses and Deformations in Direct Metal SLS Process. *SFF Symposium*.

Kasperovich, G., & Hausmann, J. (2015). Improvement of fatigue resistance and ductility of TiAl6V4 processed by selective laser melting. *Journal of Materials Processing Technology*, *220*, 202–214. https://doi.org/https://doi.org/10.1016/j.jmatprotec.2015.01.025

REFERENCES (continued)

Kempen, L., Thijs, L., Vrancken, B., Buls, S., Humbeeck, J. Van, & Kruth, J.-P. (2013). Producing crack-free, high density M2 HSS parts by Selective Laser Melting: Pre-heating the baseplate. *Proceedings of the 24th International Solid Freeform Fabrication Symposium*, 131–139.

Khairallah, S. A., Anderson, A. T., Rubenchik, A., & King, W. E. (2016). Laser powder-bed fusion additive manufacturing: Physics of complex melt flow and formation mechanisms of pores, spatter, and denudation zones. *Acta Materialia*. https://doi.org/10.1016/j.actamat.2016.02.014

King, W. E., Anderson, A. T., Ferencz, R. M., Hodge, N. E., Kamath, C., Khairallah, S. A., & Rubenchik, A. M. (2015). *Laser powder bed fusion additive manufacturing of metals ; physics , computational , and materials challenges*. *041304*. https://doi.org/10.1063/1.4937809

Kolossov, S. (2005). *Non-linear model and finite element simulation of the selective laser sintering process*. https://doi.org/10.5075/epfl-thesis-3178

Kozak, J., & Zakrzewski, T. (2018). *Accuracy Problems of Additive Manufacturing Using SLS / SLM Processes*. *020010*. https://doi.org/10.1063/1.5056273

Kruth, J. P., Mercelis, P., Van Vaerenbergh, J., Froyen, L., & Rombouts, M. (2005). Binding mechanisms in selective laser sintering and selective laser melting. In *Rapid Prototyping Journal*. https://doi.org/10.1108/13552540510573365

REFERENCES (continued)

Kruth, Jean Pierre, Deckers, J., Yasa, E., & Wauthlé, R. (2012). Assessing and comparing influencing factors of residual stresses in selective laser melting using a novel analysis method. *Proceedings of the Institution of Mechanical Engineers, Part B: Journal of Engineering Manufacture*, *226*(6), 980–991. https://doi.org/10.1177/0954405412437085

Kumar, S., Shanghai, M., & Tong, J. (2014). *Selective Laser Sintering / Melting* (Vol. 10, pp. 93–134). Elsevier Ltd. https://doi.org/10.1016/B978-0-08-096532-1.01003-7

Kuroda, S., Kawakita, J., Watanabe, M., Kim, K. H., Molak, R., & Katanoda, H. (2015). Current status and future prospects of warm spray technology. In *Future Development of Thermal Spray Coatings: Types, Designs, Manufacture and Applications*. https://doi.org/10.1016/B978-0-85709-769-9.00007-5

Kushan, M., Poyraz, Ö., Uzunonat, Y., & Orak, S. (2018). Review Article SYSTEMATICAL REVIEW ON THE NUMERICAL SIMULATIONS OF LASER POWDER BED ADDITIVE MANUFACTURING. *Sigma Journal of Engineering and Natural Sciences*. https://www.researchgate.net/publication/329802213_Review_Article_SYSTEMATICAL_REVIEW_ON_THE_NUMERICAL_SIMULATIONS_OF_LASER_POWDER_BED_ADDITIVE_MANUFACTURING

Lee, H., Lim, C. H. J., Low, M. J., Tham, N., Murukeshan, V. M., & Kim, Y. J. (2017). Lasers in additive manufacturing: A review. *International Journal of Precision Engineering and Manufacturing - Green Technology*, *4*(3), 307–322. https://doi.org/10.1007/s40684-017-0037-7

REFERENCES (continued)

Leitz, K. H., Grohs, C., Singer, P., Tabernig, B., Plankensteiner, A., Kestler, H., & Sigl, L. S. (2018). Fundamental analysis of the influence of powder characteristics in Selective Laser Melting of molybdenum based on a multi-physical simulation model. *International Journal of Refractory Metals and Hard Materials*. https://doi.org/10.1016/j.ijrmhm.2017.11.034

Leuders, S., Thöne, M., Riemer, A., Niendorf, T., Tröster, T., Richard, H. A., & Maier, H. J. (2013). On the mechanical behaviour of titanium alloy TiAl6V4 manufactured by selective laser melting: Fatigue resistance and crack growth performance. *International Journal of Fatigue*, *48*, 300–307. https://doi.org/https://doi.org/10.1016/j.ijfatigue.2012.11.011

Li, C., Liu, Z. Y., Fang, X. Y., & Guo, Y. B. (2018). Residual Stress in Metal Additive Manufacturing. *Procedia CIRP*, *71*, 348–353. https://doi.org/10.1016/j.procir.2018.05.039

Lindgren, L. E. (2001). Finite element modeling and simulation of welding part 1: Increased complexity. *Journal of Thermal Stresses*. https://doi.org/10.1080/01495730150500442

Liu, B., Wildman, R., Tuck, C., Ashcroft, I., & Hague, R. (2011). Investigation the effect of particle size distribution on processing parameters optimisation in selective laser melting process. *Proceedings of the Solid Freeform Fabrication Symposium*, *January*, 227–238. https://doi.org/10.1017/CBO9781107415324.004

Liu, S., & Shin, Y. C. (2019). Additive manufacturing of Ti6Al4V alloy: A review. *Materials and Design*, *164*, 107552. https://doi.org/10.1016/j.matdes.2018.107552

REFERENCES (continued)

Liu, Y., Yang, Y., & Wang, D. (2016). A study on the residual stress during selective laser melting (SLM) of metallic powder. *The International Journal of Advanced Manufacturing Technology*, *87*(1), 647–656. https://doi.org/10.1007/s00170-016-8466-y

Lu, Y., Wu, S., Gan, Y., Huang, T., Yang, C., Junjie, L., & Lin, J. (2015). Study on the microstructure, mechanical property and residual stress of SLM Inconel-718 alloy manufactured by differing island scanning strategy. *Optics and Laser Technology*, *75*(November), 197–206. https://doi.org/10.1016/j.optlastec.2015.07.009

Ma, L., & Bin, H. (2007). Temperature and stress analysis and simulation in fractal scanning-based laser sintering. *International Journal of Advanced Manufacturing Technology*. https://doi.org/10.1007/s00170-006-0665-5

Ma, M., Wang, Z., Gao, M., & Zeng, X. (2015). Layer thickness dependence of performance in high-power selective laser melting of 1Cr18Ni9Ti stainless steel. *Journal of Materials Processing Technology*, *215*(1), 142–150. https://doi.org/10.1016/j.jmatprotec.2014.07.034

MatWeb. (2020). *Titanium Ti-6Al-4V (Grade 5), Annealed*. http://www.matweb.com/search/DataSheet.aspx?MatGUID=a0655d261898456b958e5f825ae85390&ckck=1

Megahed, M., Mindt, H.-W., N'Dri, N., Duan, H., & Desmaison, O. (2016). Metal additive-manufacturing process and residual stress modeling. *Integrating Materials and Manufacturing Innovation*, *5*(1), 61–93. https://doi.org/10.1186/s40192-016-0047-2

REFERENCES (continued)

Mercelis, P., & Kruth, J. (2006). Residual stresses in selective laser sintering and selective laser melting. *Rapid Prototyping Journal*, *12*(5), 254–265. https://doi.org/10.1108/13552540610707013

Michaleris, P. (2014). Modeling metal deposition in heat transfer analyses of additive manufacturing processes. *Finite Elements in Analysis and Design*, *86*, 51–60. https://doi.org/10.1016/j.finel.2014.04.003

Mishra, A. K., Aggarwal, A., Kumar, A., & Sinha, N. (2018). Identification of a suitable volumetric heat source for modelling of selective laser melting of Ti6Al4V powder using numerical and experimental validation approach. *International Journal of Advanced Manufacturing Technology*. https://doi.org/10.1007/s00170-018-2631-4

Moges, T., Ameta, G., & Witherell, P. (2019). A Review of Model Inaccuracy and Parameter Uncertainty in Laser Powder Bed Fusion Models and Simulations. In *Journal of Manufacturing Science and Engineering, Transactions of the ASME*. https://doi.org/10.1115/1.4042789

Mumtaz, K., Vora, P., & Hopkinson, N. (2011). A Method To Eliminate Anchors/Supports From Directly Laser Melted Metal Powder Bed Processes. *Proc. Solid Freeform Fabrication Symposium., August 2011*, 55–64.

Munsch, M. (2017). Laser additive manufacturing of customized prosthetics and implants for biomedical applications. In *Laser Additive Manufacturing: Materials, Design, Technologies, and Applications*. https://doi.org/10.1016/B978-0-08-100433-3.00015-4

REFERENCES (continued)

Neugebauer, F., Keller, N., Xu, H., Kober, C., & Ploshikhin, V. (2014). Simulation of Selective Laser Melting Using Process Specific Layer Based Meshing. *Proceedings of the Fraunhofer Direct Digital Manufacturing Conference*.

Okamoto, H., Okabe, K., Yuri, Y., Möhl, D., & Sessler, A. M. (2004). Laser Additive Manufacturing: Materials, Design, Technologies, and Applications. In *Physical Review E - Statistical Physics, Plasmas, Fluids, and Related Interdisciplinary Topics* (Vol. 69, Issue 6). https://doi.org/10.1103/PhysRevE.69.066504

Pal, S., & Drstvensek, I. (2018). *Physical Behaviors of Materials in Selective Laser Melting Process*. *November*, 239–256. https://doi.org/10.2507/daaam.scibook.2018.21

Papadakis, L., Branner, G., Schober, A., Richter, K. H., & Uihlein, T. (2012). Numerical modeling of heat effects during thermal manufacturing of aero engine components. *Lecture Notes in Engineering and Computer Science*.

Parry, L. A. (2018). *Investigation of residual stress in selective laser melting*.

Parry, L., Ashcroft, I. A., & Wildman, R. D. (2016). Understanding the effect of laser scan strategy on residual stress in selective laser melting through thermo-mechanical simulation. *Additive Manufacturing*, *12*, 1–15. https://doi.org/10.1016/j.addma.2016.05.014

Paul, R., Anand, S., & Gerner, F. (2014). Effect of thermal deformation on part errors in metal powder based additive manufacturing processes. *Journal of Manufacturing Science and Engineering, Transactions of the ASME*. https://doi.org/10.1115/1.4026524

REFERENCES (continued)

Peter, N., Pitts, Z., Thompson, S., & Saharan, A. (2020). Benchmarking build simulation software for laser powder bed fusion of metals. *Additive Manufacturing*. https://doi.org/10.1016/j.addma.2020.101531

Poprawe, R., Hinke, C., Meiners, W., Schrage, J., Bremen, S., & Merkt, S. (2014). SLM Production Systems: Recent Developments in Process Development, Machine Concepts and Component Design. In *Advances in Production Technology* (Issue 3, pp. 49–65). https://doi.org/10.1007/978-3-319-12304-2

Prashanth, K. G., Scudino, S., Maity, T., Das, J., & Eckert, J. (2017). Is the energy density a reliable parameter for materials synthesis by selective laser melting? *Materials Research Letters*. https://doi.org/10.1080/21663831.2017.1299808

Qiu, C., Panwisawas, C., Ward, M., Basoalto, H. C., Brooks, J. W., & Attallah, M. M. (2015). On the role of melt flow into the surface structure and porosity development during selective laser melting. *Acta Materialia*, *96*, 72–79. https://doi.org/10.1016/j.actamat.2015.06.004

Rafi, H. K., Karthik, N. V., Gong, H., Starr, T. L., & Stucker, B. E. (2013). Microstructures and mechanical properties of Ti6Al4V parts fabricated by selective laser melting and electron beam melting. *Journal of Materials Engineering and Performance*, *22*(12), 3872–3883. https://doi.org/10.1007/s11665-013-0658-0

Sames, W. J., List, F. A., Pannala, S., Dehoff, R. R., & Babu, S. S. (2016). The metallurgy and processing science of metal additive manufacturing. *International Materials Reviews*, *61*(5), 315–360. https://doi.org/10.1080/09506608.2015.1116649

REFERENCES (continued)

Savalani, M. M., & Pizarro, J. M. (2016). Effect of preheat and layer thickness on selective laser melting (SLM) of magnesium. *Rapid Prototyping Journal*, *22*(1), 115–122. https://doi.org/10.1108/RPJ-07-2013-0076

Saxena, S., Kumar, A., Ali, H., Ghadbeigi, H., & Mumtaz, K. (2016). Residual stress development in selective laser-melted Ti6Al4V: a parametric thermal modelling approach. In *The International Journal of Advanced Manufacturing Technology* (Vol. 97, Issue 5). https://doi.org/10.1007/s00170-018-2104-9

Schoinochoritis, B., Chantzis, D., & Salonitis, K. (2015). Simulation of metallic powder bed additive manufacturing processes with the finite element method: A critical review. *Proceedings of the Institution of Mechanical Engineers, Part B: Journal of Engineering Manufacture*, *231*. https://doi.org/10.1177/0954405414567522

Seifi, M., Salem, A., Beuth, J., Harrysson, O., & Lewandowski, J. J. (2016). Overview of Materials Qualification Needs for Metal Additive Manufacturing. *JOM*, *68*(3), 747–764. https://doi.org/10.1007/s11837-015-1810-0

Shah, A., Ismail, S. N. F., Hasan, M. A., & Daud, R. (2018). Surface Modification on Titanium Alloy for Biomedical Application ☆. In *Reference Module in Materials Science and Materials Engineering*. https://doi.org/10.1016/b978-0-12-803581-8.10484-9

Shi, X., Ma, S., Liu, C., Chen, C., Wu, Q., Chen, X., & Lu, J. (2016). Performance of high layer thickness in selective laser melting of Ti6Al4V. *Materials*, *9*(12), 1–15. https://doi.org/10.3390/ma9120975

REFERENCES (continued)

Shipley, H., McDonnell, D., Culleton, M., Coull, R., Lupoi, R., O'Donnell, G., & Trimble, D. (2018). Optimisation of process parameters to address fundamental challenges during selective laser melting of Ti-6Al-4V: A review. *International Journal of Machine Tools and Manufacture*, *128*(January), 1–20. https://doi.org/10.1016/j.ijmachtools.2018.01.003

Simonelli, M., Tse, Y. Y., & Tuck, C. (2012). Microstructure of Ti-6Al-4V produced by selective laser melting. *Journal of Physics: Conference Series*, *371*, 12084. https://doi.org/10.1088/1742-6596/371/1/012084

Sing, S. L., An, J., Yeong, W. Y., & Wiria, F. E. (2016). Laser and electron-beam powder-bed additive manufacturing of metallic implants: A review on processes, materials and designs. *Journal of Orthopaedic Research*, *34*(3), 369–385. https://doi.org/10.1002/jor.23075

SLM Solutions Group AG. (2020). *SLM®800 Powder Bed Fusion Metal AM System for Large Builds*. https://www.slm-solutions.com/en/products/machines/slmr800/

Song, X., Xie, M., Hofmann, F., Illston, T., Connolley, T., Reinhard, C., Atwood, R. C., Connor, L., Drakopoulos, M., Frampton, L., & Korsunsky, A. M. (2015). Residual stresses and microstructure in Powder Bed Direct Laser Deposition (PB DLD) samples. *International Journal of Material Forming*. https://doi.org/10.1007/s12289-014-1163-1

Stevenson, K. (2018). *SLM Solutions Making Things Easier*. https://www.fabbaloo.com/blog/2018/7/27/slm-solutions-making-things-easier

REFERENCES (continued)

Sufiiarov, V. S., Popovich, A. A., Borisov, E. V., Polozov, I. A., Masaylo, D. V., & Orlov, A. V. (2017). The Effect of Layer Thickness at Selective Laser Melting. *Procedia Engineering*, *174*, 126–134. https://doi.org/10.1016/j.proeng.2017.01.179

Sutton, A. T., Kriewall, C. S., Leu, M. C., & Newkirk, J. W. (2016). Powders for Additive Manufacturing Processes: Characterization Techniques and Effects on Part Properties. *Solid Freeform Fabrication 2016: Proceedings of the 26th Annual International Solid Freeform Fabrication Symposium*, 1004–1030.

Tan, X. P., Tan, Y. J., Chow, C. S. L., Tor, S. B., & Yeong, W. Y. (2017). Metallic powder-bed based 3D printing of cellular scaffolds for orthopaedic implants: A state-of-the-art review on manufacturing, topological design, mechanical properties and biocompatibility. *Materials Science and Engineering: C*, *76*, 1328–1343. https://doi.org/https://doi.org/10.1016/j.msec.2017.02.094

Thijs, L., Verhaeghe, F., Craeghs, T., Humbeeck, J. Van, & Kruth, J. P. (2010). A study of the microstructural evolution during selective laser melting of Ti-6Al-4V. *Acta Materialia*, *58*(9), 3303–3312. https://doi.org/10.1016/j.actamat.2010.02.004

Trevisan, F., Calignano, F., Lorusso, M., Pakkanen, J., Aversa, A., Ambrosio, E. P., Lombardi, M., Fino, P., & Manfredi, D. (2017). On the selective laser melting (SLM) of the AlSi10Mg alloy: Process, microstructure, and mechanical properties. *Materials*, *10*(1). https://doi.org/10.3390/ma10010076

Van Belle, L., Vansteenkiste, G., & Boyer, J. C. (2012). Comparisons of numerical modelling of the Selective Laser Melting. *Key Engineering Materials*. https://doi.org/10.4028/www.scientific.net/KEM.504-506.1067

REFERENCES (continued)

Vastola, G., Zhang, G., Pei, Q. X., & Zhang, Y.-W. (2016). Controlling of residual stress in additive manufacturing of Ti6Al4V by finite element modeling. *Additive Manufacturing*, *12*, 231–239. https://doi.org/https://doi.org/10.1016/j.addma.2016.05.010

Vilaro, T., Colin, C., & Bartout, J. D. (2011). As-fabricated and heat-treated microstructures of the Ti-6Al-4V alloy processed by selective laser melting. *Metallurgical and Materials Transactions A: Physical Metallurgy and Materials Science*, *42*(10), 3190–3199. https://doi.org/10.1007/s11661-011-0731-y

Vrancken, B. (2016). Study of Residual Stresses in Selective Laser Melting. *PhD Thesis; KU Leuven Arenberg Doctoral School Faculty of Engineering Science*, *June*, 1–253. https://lirias.kuleuven.be/bitstream/123456789/542751/1/thesis+Bey+Vrancken+v01-06-2016+FINAL_compressed.pdf

Vrancken, B., Buls, S., Kruth, J.-P., & Van Humbeeck, J. (2015). Influence of preheating and oxygen content on Selective Laser Melting of Ti6Al4V. In *Proceedings of the 16th RAPDASA Conference*.

Vrancken, B., Thijs, L., Kruth, J. P., & Van Humbeeck, J. (2012). Heat treatment of Ti6Al4V produced by Selective Laser Melting: Microstructure and mechanical properties. *Journal of Alloys and Compounds*, *541*, 177–185. https://doi.org/10.1016/j.jallcom.2012.07.022

Wang, D., Dou, W., & Yang, Y. (2018). Research on Selective Laser Melting of Ti6Al4V: Surface Morphologies, Optimized Processing Zone, and Ductility Improvement Mechanism. *Metals*, *8*(7), 471. https://doi.org/10.3390/met8070471

REFERENCES (continued)

Wang, D., Wu, S., Fu, F., Mai, S., Yang, Y., Liu, Y., & Song, C. (2016). Mechanisms and characteristics of spatter generation in SLM processing and its effect on the properties. *Materials & Design*, *117*. https://doi.org/10.1016/j.matdes.2016.12.060

Wehmöller, M., Warnke, P. H., Zilian, C., & Eufinger, H. (2005). Implant design and production-a new approach by selective laser melting. *International Congress Series*, *1281*, 690–695. https://doi.org/10.1016/j.ics.2005.03.155

Xia, M., Gu, D., Yu, G., Dai, D., Chen, H., & Shi, Q. (2017). Porosity evolution and its thermodynamic mechanism of randomly packed powder-bed during selective laser melting of Inconel 718 alloy. *International Journal of Machine Tools and Manufacture*, *116*(January), 96–106. https://doi.org/10.1016/j.ijmachtools.2017.01.005

Yang, L., Hsu, K., Baughman, B., Godfrey, D., Medina, F., Menon, M., & Wiener, S. (2017). Additive Manufacturing of Metals: The Technology, Materials, Design and Production. In *Springer Series in Advanced Manufacturing*. https://doi.org/10.1007/978-3-319-55128-9

Yap, C. Y., Chua, C. K., Dong, Z. L., Liu, Z. H., Zhang, D. Q., Loh, L. E., & Sing, S. L. (2015). Review of selective laser melting: Materials and applications. *Applied Physics Reviews*, *2*(4). https://doi.org/10.1063/1.4935926

Yasa, E. (2018). Understanding Adopting Selective Laser Melting of Metallic Materials. *Solid Freeform Fabrication 2018: Proceedings of the 29th Annual International Solid Freeform Fabrication Symposium*. http://utw10945.utweb.utexas.edu/sites/default/files/2018/100 UnderstandingAdoptingSelectiveLaserMeltingof.pdf

REFERENCES (continued)

Yasa, E., Deckers, J., Craeghs, T., Badrossamay, M., & Kruth, J.-P. (2009). Investigation on occurrence of elevated edges in selective laser melting. In *20th Annual International Solid Freeform Fabrication Symposium, SFF 2009*.

Yılmaz, N., & Kayacan, M. Y. (2020). Effect of single and multiple parts manufacturing on temperature-induced residual stress problems in SLM. *International Journal of Material Forming*. https://doi.org/10.1007/s12289-020-01560-1

Zaeh, M. F., & Branner, G. (2010). Investigations on residual stresses and deformations in selective laser melting. *Production Engineering*, *4*(1), 35–45. https://doi.org/10.1007/s11740-009-0192-y

Zhang, B., Li, Y., & Bai, Q. (2017). Defect Formation Mechanisms in Selective Laser Melting: A Review. *Chinese Journal of Mechanical Engineering (English Edition)*, *30*(3), 515–527. https://doi.org/10.1007/s10033-017-0121-5

Zhang, H., & LeBlanc, S. (2018). Processing Parameters for Selective Laser Sintering or Melting of Oxide Ceramics. In I. Shishkovsky (Ed.), *Additive Manufacturing of High-performance Metals and Alloys: Modeling and Optimization* (pp. 89–125). Intech Open. https://doi.org/10.5772/intechopen.75832

Zhao, X., Li, S., Zhang, M., Liu, Y., Sercombe, T. B., Wang, S., Hao, Y., Yang, R., & Murr, L. E. (2016). Comparison of the microstructures and mechanical properties of Ti–6Al–4V fabricated by selective laser melting and electron beam melting. *Materials & Design*, *95*, 21–31. https://doi.org/https://doi.org/10.1016/j.matdes.2015.12.135

Zhou, X., Liu, X., Zhang, D., Shen, Z., & Liu, W. (2015). Balling phenomena in selective laser melted tungsten. *Journal of Materials Processing Technology*, *222*. https://doi.org/10.1016/j.jmatprotec.2015.02.032